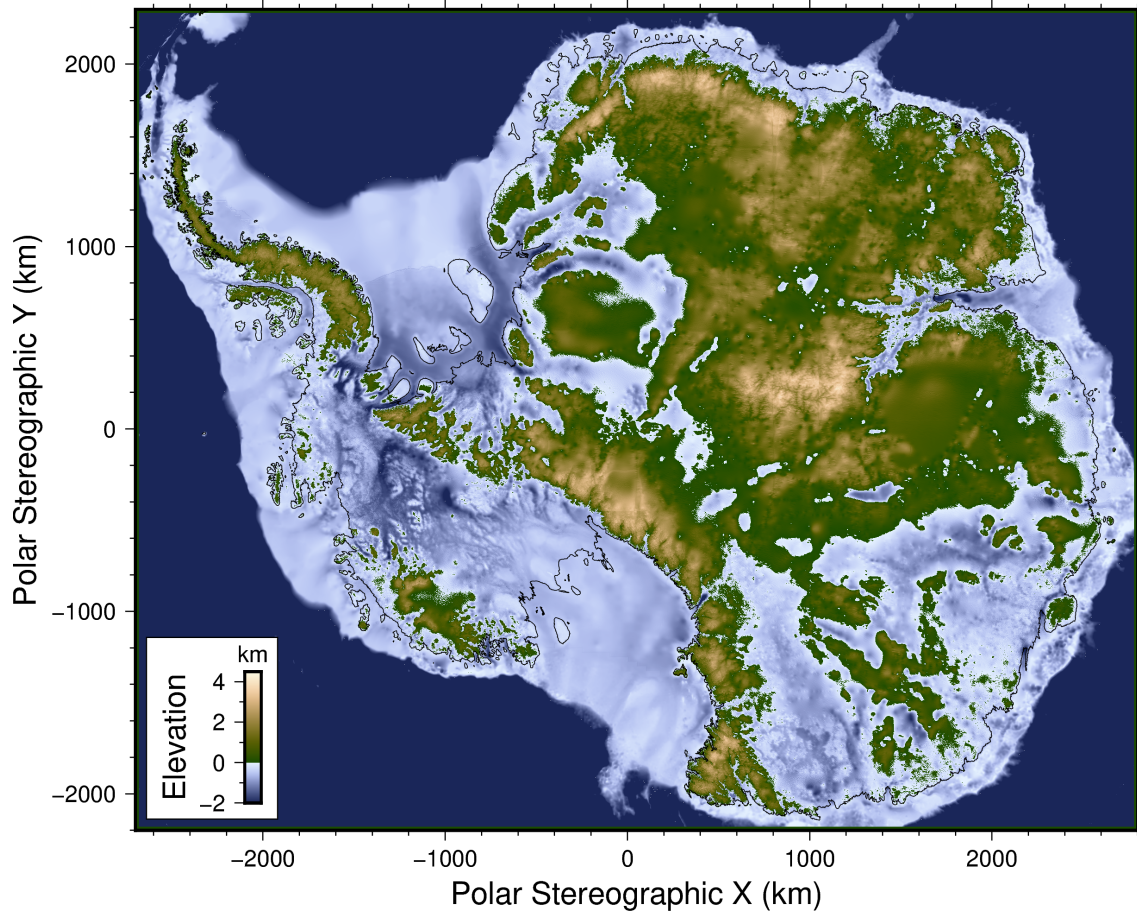
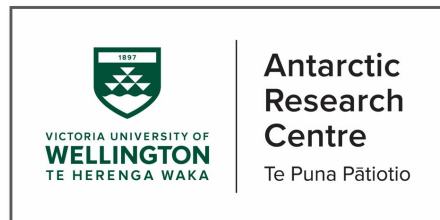


The subglacial landscape and hydrology of Antarctica mapped from space



A thesis presented for the degree of
Doctor of Philosophy in Physical Geography

Wei Ji Leong



Antarctic Research Centre
Victoria University of Wellington
New Zealand
12 July 2021

Abstract

To narrow uncertainties in the Antarctic ice sheet's contribution to sea level rise, we present a collection of novel machine learning and automated satellite remote sensing methods which use ice surface observations to infer the subglacial nature of Antarctica. A super-resolution deep neural network called DeepBedMap was designed and trained to produce a high-resolution (250 m) bed elevation model of Antarctica called DeepBedMap_DEM that preserves bed roughness details useful for catchment- to continent-scale ice sheet modelling. This DeepBedMap_DEM is compared with a smoother, medium-resolution (500 m) BedMachine topography in a basal inversion experiment over Pine Island Glacier, with results motivating more research into the interacting roles of subglacial hydrology which influences skin drag and high resolution bed topographies which influences form drag. Active subglacial lakes in Antarctica were mapped using an unsupervised density-based classification method on ICESat-2 point cloud data from 2018–2020, yielding 194 active subglacial lakes, including 36 new lakes in the 86–88°S area not detected by the previous ICESat (2003–2009) mission. This thesis showcases both the rich diversity in subglacial landscapes and the dynamic nature of subglacial hydrology in Antarctica, forming a foundation enabling the accurate modelling of overland ice flow in critical regions of the vulnerable West Antarctic Ice Sheet.

Plain language summary

Antarctica has a lot of ice, but we're unsure how fast ice can slide into the sea and cause water to go up in beaches around the world. So we teach computers to solve hard math problems that tell us how fast sea water might go up. These computers are fed with lots of pictures taken from cameras up in the sky and space. Ice sits on top of rock in Antarctica, and with practice, the computers get pretty good at telling us how high and bumpy the rock is. The rock under the ice appears quite bumpy, and ice probably doesn't like sliding over bumpy rocks since it's rough. Sometimes though, ice may not mind sliding over rough bits of rock if the rock moves along with it, or if water gets in between the rock and ice to makes things slippery, but we ask our smart computers to be sure. There are also lasers from space shooting down at earth and bouncing back to tell us how ice in Antarctica is going up or down. Once in a while, they tell us that ice in parts of Antarctica moved up or down a bit too fast. Smart people think these are lakes hiding under the ice, filling up with water or draining, and we found many of these lakes over Antarctica, especially in an area called Whillans Ice Stream on the Siple Coast. We hope that the computers can keep learning faster because there's a lot of pictures showing ice moving pretty fast, and it doesn't look like there's much time before a big chunk of ice might break away in Antarctica and flood beaches around the world.

Dedication

To Penny, who led me, so profoundly, to be

Acknowledgements

每一个成功男人的背后，都有一个伟大的女人。 Every step along this journey has not been without the support of a great community behind me. My Chinese name is 梁伟吉，each character signifying a part of who I am, my duty in this world, and the enormous privilege that has allowed me to make it to this day.

Family 梁(Leong) comes first. My dearest partner Penny Qiu Yue 邱乐, you have went above and beyond what a normal long distance relationship entails, keeping me company daily through good times and bad, being patient, trusting and more than I could ever express in my supposedly native yet broken Malaysian/Bruneian Chinese. Above all, thank you for sharing the most precious asset there is - 时间- time - which for that, I am forever grateful. To my younger sister Wei Qian 伟倩and brother Wei Tong 伟桐, growing up with you two in Brunei has taught me the importance of sharing and looking after each other, so thank you for your understanding, for all the catch up calls, and simply for being. For Dad and Mum, 梁耀明and 陈碹丝, it takes a million to raise one child, let alone three, and I have lost count of the number of side jobs you've had over the years, especially the struggles in recent times, both of you deserve a special thank you and a long holiday.

To my local family in Wellington, Jaclyn and David Chai, for the nourishment you have provided over the years in the form of yummy Malaysian style vegetarian food. It is unbelievable how fast time flies, seeing your two kids ZH and Yi Ling grow tall and mature, you are all my second family and will always be remembered.

Greatness 伟(Wei) of teachers is next. To my great supervisor Huw Horgan (and his amazing partner Ruschle), I sometimes wonder how a person from the tropics without a trace of snow got into studying Antarctic ice, and obviously it was because of you, from that time in 2014 studying proglacial lakes at Mount Cook national park, to my 2015 Honours project on mapping potential subglacial estuaries in Antarctica, to this very PhD thesis 2017-2021. A very big thank you for allowing me to do my work remotely using satellites, sending me randomly on exchanges to Alaska and Austria to realize how big the world truly is, for giving me the space to develop independently, while providing top notch Yoda-like advice that takes me weeks and months to figure out.

Thank you to all my Geography teachers and mentors over the years. In particular, to my secondary school teacher Veronica Chan at Chung Hwa Middle School, for your great style of Geography teaching with funny stories and sketches, it was weird that you didn't recommend me taking Geography in high school, but here I am now. To my university lecturer Mairéad de Róiste, for putting me on this journey into Geographic Information Systems (GIS), setting good examples on how to tutor the next generation of students, and also for drilling in Cartographic best practices. To Karl Baker at e-Spatial, for passing on your guru level of stacking and mosaicking aerial imagery, arranging map layers to perfection, and for being a role model on how to be a respectable GIS professional.

Luck 吉(Ji) is the last but not least. I feel really fortunate to be able to stand on the shoulders of giants, and would like to acknowledge at least some of the many people I've met along this journey.

Open source

To Leonardo Uieda, DongDong Tian 田冬冬, Liam Toney and the rest of the PyGMT team, and also to Paul Wessel for his enduring work on the Generic Mapping Tools (GMT) package over many decades, it is a pleasure to have such a great tool for producing beautiful maps. To all the folks maintaining the Python and Pangeo ecosystem of geospatial packages, from Xarray to RAPIDS AI and every imaginable library in between, thank you for all the new features and bug fixes, keep up the good work!

Europe

To Poonam Vishwas, KaiKai Xue 薛凯, Yawen Tan 谭雅文, and all the friends I met in the 2019 Erasmus+ exchange at ZGIS, University of Salzburg, Austria, it was an awesome experience having so many like-minded people researching GIS together in Europe, an experience I will always treasure. To Dr. Hermann Klug, thank you for warmly inviting me to Salzburg and sorting out all manners of logistics in German, and to Dr. Dirk Tiede for introducing me to Object Based Image Analysis and providing a conceptual framework for understanding the place of Convolutional Neural Networks in the wider field of supervised classification in GIS.

United States

To Anushilan Acharya, Indraneel Kasmalkar, Whyjay Zheng, and all my friends in the 2018 McCarthy International Summer School in Glaciology, it was a great pleasure meeting you all, and I look forward to seeing some of you again at some point! To Dr. Regine Hock, thank you for inviting me to Alaska and giving me a once in a lifetime experience of stepping on a big glacier, and to Dr. Kelly Brunt for some great lessons on the ICESat-2 laser altimetry satellite! To the International Glaciological Society (IGS), thank you for the generous early career travel grant and the chance to present a talk at the 2019 IGS Five Decades of Radioglaciology Symposium at Stanford University.

New Zealand

To Arran Whiteford, Alanna Alevropoulos-Borrill, Francesca Baldacchino, my CO522 office mates at the Antarctic Research Centre, for all the yarns about ice and other topics, I couldn't have asked for a nicer group of friendly folks to do my PhD with! To Dao Polsiri and Michelle Dow, thank you for sorting out all sorts of paperwork from flight ticket changes to funding for trivial things, and also to Aleksandr Beliaev, for troubleshooting issues with the UNIX servers and putting up with my overuse of storage, RAM, GPU resources and all.

Finally to anyone that I left out, you are not unnoticed, this sentence is for you, and I hope you enjoy reading this thesis just as much as I do.

Contents

Acronyms	15
1 Introduction	17
1.1 Motivation	17
1.2 Thesis context	18
1.2.1 Research Questions	18
1.2.2 Outline	19
1.3 Background	19
2 DeepBedMap: a deep neural network for resolving the bed topography of Antarctica	25
2.1 Introduction	25
2.2 Related Work	27
2.2.1 Super-Resolution	27
2.2.2 Network Conditioning	28
2.3 Data and Methods	29
2.3.1 Data Preparation	29
2.3.2 Model Design	31
2.4 Results	34
2.4.1 DeepBedMap_DEM Topography	34
2.4.2 Surface Roughness	37
2.5 Discussion	40
2.5.1 Bed Features	40
2.5.2 Roughness	40
2.5.3 Limitations	41
2.5.4 Future directions	42
2.6 Conclusions	43
2.7 Code and data availability	44
2.8 Acknowledgements	44
3 The role of subglacial topography on Antarctic ice flow	47
3.1 Introduction	47
3.1.1 Bed Topography	48
3.1.2 Basal drag	49
3.1.3 Previous work	52
3.2 Methods	53
3.2.1 Ice Sheet model set-up	53
3.2.2 Inverting for basal drag τ_b	55
3.3 Results	56
3.4 Discussion and Conclusion	64

4 Automated classification of active subglacial lakes in Antarctica from ICESat-2/ATLAS laser altimetry (2018–2020)	67
4.1 Introduction	67
4.1.1 Subglacial lakes in Antarctica	68
4.1.2 Antarctic subglacial water system interactions	71
4.2 Methods	74
4.2.1 Components of ice surface elevation change over time	74
4.2.2 Active subglacial lake detection from remote sensing	77
4.2.3 Measuring rapid height change signals	78
4.2.4 Clustering active lakes: Using DBSCAN	79
4.2.5 Crossover track analysis and ice volume displacement	80
4.3 Results	82
4.3.1 ICESat-2 active subglacial lake inventory	82
4.3.2 Active subglacial lakes at Whillans Ice Stream central basin .	83
4.4 Discussion	92
4.4.1 Comparison to previous active subglacial lake studies	92
4.4.2 Multi-lobe active subglacial lakes	92
4.4.3 Cascading drain fill activity of Whillans subglacial lakes . .	93
4.4.4 Limitations	96
4.5 Conclusions	96
5 Conclusion	99
5.1 Research Questions	99
5.2 Future work	100
5.2.1 Towards BEDMAP3 - More data to super-resolve the bed topography of Antarctica	101
5.2.2 Coupling ice flow models with evolving subglacial hydrological models	101
5.2.3 Continuous active subglacial lake time-series data	101
5.3 Concluding remark	102
A Details of loss function components	103
A.1 Content Loss	103
A.2 Adversarial Loss	103
A.3 Topographic Loss	104
A.4 Structural Loss	104
A.5 Total Loss Function	105
B Neural Network Training Details	107
C Hydropotential	109

List of Figures

1.1	Cryospheric contribution to sea level change by 2100	17
1.2	Comparison of bed elevation products along ground-truth transects . .	21
1.3	Universal glacier slip law	22
1.4	Map of radio-echo sounding and satellite-detected subglacial lakes in Antarctica	23
2.1	DeepBedMap generator model architecture	31
2.2	DeepBedMap_DEM overview map over the entire Antarctic continent	33
2.3	2-D comparison of interpolated bed elevation grid products over Pine Island Glacier	35
2.4	2-D Close-up views of DeepBedMap_DEM over Antarctica	36
2.5	Spatial 2-D view of bed elevation and roughness grids over Thwaites Glacier	38
2.6	Transect plots of bed elevation and surface roughness of interpolated grid products	39
3.1	Comparison of Weertman, Budd, Schoof and Tsai sliding laws	51
3.2	Topographies and Speed over Pine Island Glacier	54
3.3	Comparison of basal velocity over Pine Island Glacier for DeepBedMap and BedMachine	57
3.4	Comparison of effective pressure over Pine Island Glacier for DeepBedMap and BedMachine	58
3.5	Comparison of slipperiness over Pine Island Glacier for DeepBedMap and BedMachine	60
3.6	Comparison of basal drag over Pine Island Glacier for DeepBedMap and BedMachine	61
3.7	Transect plot along Pine Island Glacier trunk	62
3.8	Transect plot cutting across Pine Island Glacier trunk	63
4.1	Distribution of ICESat-2 active subglacial lakes from 2018-2020 . . .	68
4.2	Channelized vs distributed flow in a subglacial water system	72
4.3	Seasonal cycle of ice surface elevation change over Antarctica	75
4.4	Schematic of ICESat-2 altimetry repeat-track and crossover-track analysis	81
4.5	Siple Coast active subglacial lakes detected by ICESat-2 laser altimetry	82
4.6	Elevation anomaly of crossover points within Whillans 7	84
4.7	Digital Surface elevation Model and elevation trend map at Whillans 7	85
4.8	Along track view of ice surface elevation over Whillans 7	85
4.9	Elevation anomaly of crossover points within Whillans IX	86

4.10 Digital Surface elevation Model and elevation trend map at Whillans IX	87
4.11 Along track view of ice surface elevation over Whillans IX	87
4.12 Elevation anomaly of crossover points within Subglacial Lake Whillans	88
4.13 Digital Surface elevation Model and elevation trend map at Subglacial Lake Whillans	89
4.14 Along track view of ice surface elevation over Subglacial Lake Whillans	89
4.15 Elevation anomaly of crossover points within Lake 12	90
4.16 Digital Surface elevation Model and elevation trend map at Lake 12	91
4.17 Along track view of ice surface elevation over Lake 12	91
4.18 Ice Volume displacement over Whillans Ice Stream Central Catchment lakes	93
4.19 Modelled subglacial water flux (2003-2009) over Kamb, Whillans and Mercer Ice Stream	95

List of Tables

2.1	High-resolution ground-truth datasets for training DeepBedMap . . .	29
2.2	Remote sensing dataset inputs into the DeepBedMap neural network model.	30
B.1	Optimized hyperparameter settings.	107

Acronyms

ConvNets

Convolutional Neural Networks

DBSCAN

Density-based Spatial Clustering of Applications with Noise

DEM

Digital Elevation Model

ESRGAN

Enhanced Super-Resolution Generative Adversarial Network

ICESat-2

Ice, Cloud, and land Elevation Satellite 2. A near polar-orbit laser altimeter satellite that measures ice surface elevation.

IPCC

Intergovernmental Panel on Climate Change

ISSM

Ice-sheet and Sea-level System Model

LeakyReLU

Leaky Rectified Linear Unit

REMA

Reference Elevation Model of Antarctica. A high resolution, time-stamped Digital Surface Elevation Model of Antarctica created from stereophotogrammetry.

RES

Radio-echo sounding

SD

Standard deviation

SLE

Sea level equivalent

Chapter 1

Introduction

1.1 Motivation

What is the rate at which sea level will rise and affect coastal communities around the globe? Besides greenhouse gas emissions, a large uncertainty in the answer to that question lies in the Antarctic ice sheet's behaviour. By 2100, Antarctica is projected to contribute as little as 0.03 m to as much as 0.28 m sea level equivalent (SLE) of water under a high emissions scenario (RCP 8.5, Fig. 1.1f, IPCC, 2019). To narrow the range of this projection, one of the regions we need to understand is Antarctica's bed, the part hidden under the ice. This thesis synthesizes a collection of satellite remote sensing methods, using what we can see at the surface of the Antarctic continent, to deduce what is happening in the subglacial world below.

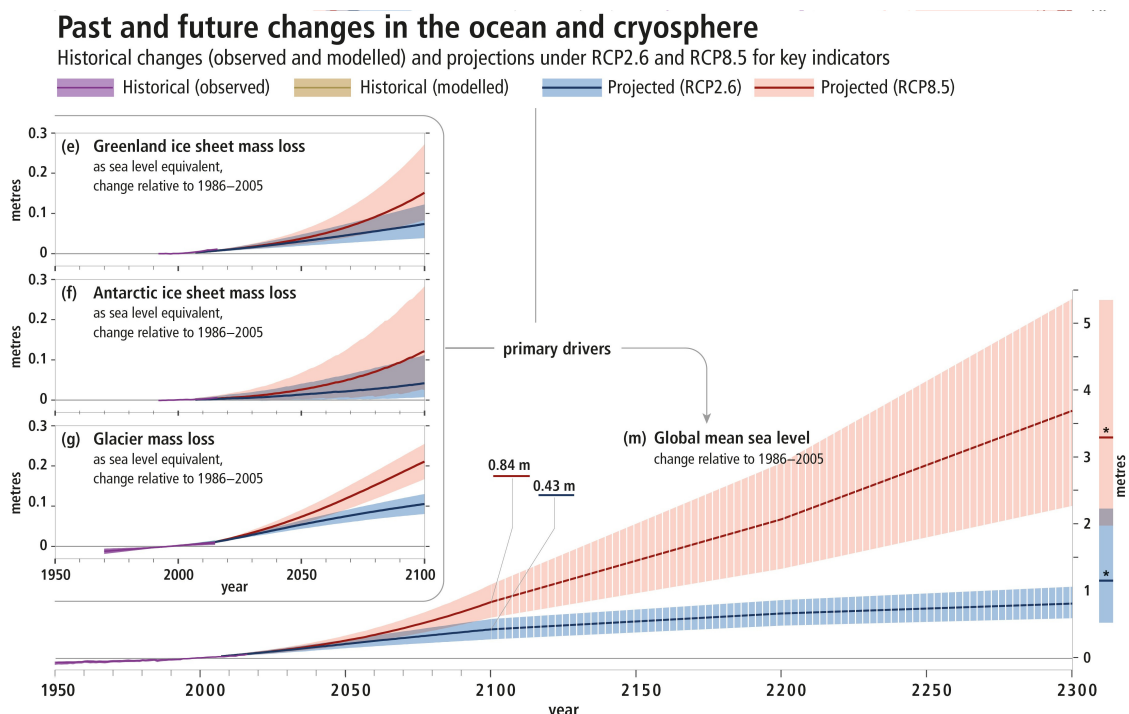


Figure 1.1: Contribution of the cryosphere to sea level change. Modelled and observed historical changes in the cryosphere since 1950, and the projected future changes under low (RCP2.6) and high (RCP8.5) greenhouse gas emissions scenarios. Figure adapted from SPM.1 in the Summary for Policy Makers, IPCC Special Report on the Ocean and Cryosphere in a Changing Climate (IPCC, 2019).

1.2 Thesis context

Antarctica is a large continent, $53\times$ the size of New Zealand or $1.8\times$ the size of Australia, and satellite measurements are one of the best ways to cover the whole icescape. While the first satellite images of Antarctica were taken in 1964 by the Nimbus I satellite (Meier et al., 2013), continuous modern-day observations only started in 1979. Forty years later, and there is now a wealth of openly available optical images of much of the continent, currently captured by NASA's Landsat 8 (Roy et al., 2014) and the European Space Agency (ESA)'s Sentinel 2 (Drusch et al., 2012). Changes to Antarctica's mass can be measured at kilometre-scale using the Gravity Recovery and Climate Experiment Follow-On (GRACE-FO, 2018-) satellites (Landerer et al., 2020), and at metre-scales using the Ice, Cloud and land Elevation Satellite-2 (ICESat-2, 2018-; Markus et al., 2017). Also with radar instruments like Sentinel 1 (Attema et al., 2009) and Cryosat 2 (Wingham et al., 2006), cloud-free monitoring of the Antarctic surface has never been easier. Sadly, most of these satellites can only observe the surface of the Antarctic continent. There are physical constraints on designing an Earth orbiting satellite which can penetrate through both the atmosphere and kilometres of ice (Culberg & Schroeder, 2020; Gogineni et al., 2018). Arguably more is known about the subglacial landscape of Mars's polar caps (Arnold et al., 2019; Lauro et al., 2020; Orosei et al., 2018) than that of our own planet Earth. Still, it is possible to infer about Antarctica's bed properties by combining satellite observations captured over large surface areas with what little is known about the bed at discrete sites targeted by oversnow observations, and this is the approach this thesis will take.

1.2.1 Research Questions

To better understand the drivers of Antarctic ice flow, we present high spatial resolution ($\leq 250\text{ m}$) views of Antarctica's subglacial geography, as inferred from satellite detected ice surface changes. Novel machine learning and automated remote sensing techniques are applied to infer both the subglacial landscape and subglacial hydrological network of Antarctica. The 3 main research questions are as follows:

1. How can we integrate existing high spatial resolution remote sensing products to boost the resolution of existing bed elevation maps of Antarctica?
2. What effect does a rough surface, high-resolution (250 m) bed topography have on the friction parameters of an ice sheet model?
3. Where does water drain and accumulate underneath the Antarctic Ice Sheet, how much volume is mobilized, and at what timescales do these processes occur?

The products of this thesis will be a revised continent-wide map of Antarctica's bed topography and subglacial hydrology, including a revised inventory of active subglacial lakes. Building on top of this, are regional-scale derived products of basal friction and a time-series of ice volume displacement analyzed at select drainage basins. Taken together, these datasets form a foundation enabling accurate modelling of overland ice flow.

1.2.2 Outline

This thesis is comprised of five chapters.

Chapter 1 establishes the context behind this research, the three research questions, and also the outline you are reading now. It also contains an introduction to the influence of subglacial topography and subglacial hydrology on ice flow.

Chapter 2 is adapted from a journal paper submitted to *The Cryosphere* (Leong & Horgan, 2020b), reformatted to fit in this thesis. It starts with an introduction to the field of deep learning in the context of geospatial science. The chapter then provides a detailed look into the construction of a convolutional neural network architecture to generate a super-resolution (250 m) bed elevation map of Antarctica from a low resolution (1000 m) BEDMAP2 input and other remote sensing observations of the ice surface.

Chapter 3 uses the neural network generated super-resolution Antarctic bed elevation map to perform an ice sheet model basal inversion over Pine Island Glacier. In this chapter, we examine the inverted properties of basal drag, effective pressure and friction coefficient using two bed elevation models of different spatial resolutions. The output of this exercise is to analyze the effects of using a rougher bed on ice flow modelling.

Chapter 4 looks into the active subglacial hydrology system of Antarctica using ICESat-2 laser altimetry. A revised and automated method for building an active subglacial lake inventory is described, with details on the timing of subglacial lake drainage and filling events, and the estimated volume of water exchanged. The increased spatiotemporal resolution of these subglacial hydrological maps, combined with an improved subglacial topography, is used to examine the drivers of Antarctic ice flow.

Chapter 5 provides a discussion of the 3 research questions, and implications for future work. It also presents the main conclusions of this thesis.

1.3 Background

Glaciers and ice sheets move in three main ways: 1) internal deformation of the ice due to gravity 2) sliding of the ice over the basal substrate 3) deformation of the basal substrate.

The latter two processes can be collectively termed as basal slip (Cuffey & Patterson, 2010). While the bed topography of Antarctica can change significantly over geological time (e.g. Hochmuth et al., 2020), the amount of water available to slide a glacier is more dynamic and can act on sub-annual to annual timescales (e.g. Siegfried et al., 2016). Much focus has been placed on the importance of subglacial water on ice dynamics, such as the draining and filling of subglacial lakes (e.g. Siegfried & Fricker, 2018; B. E. Smith et al., 2009) and glacial surges due to rainfall events (e.g. Iken et al., 1983). Another contributor is the structure of the basal topography that exerts a drag on the ice-rock contact surface (e.g. Kyrke-Smith et al., 2018). The base of the ice sheet is difficult to observe, as they require oversnow seismic or radar surveys (e.g. Holschuh et al., 2020) or direct drilling access (e.g. Tulaczyk et al., 2014). In contrast, the surface of the ice sheet can be more readily examined using satellites and other remote sensing instruments (e.g. Howat et al., 2019; Mouginot et al., 2019a). The study of basal slip at local to regional scales, from sliding due to water and bed deformation, varies with specific conditions at the

bed, and can be posed as a geographical question: 1) Where in Antarctica does bed topography not have an important control on ice flow (i.e. water is more important). 2) Where in Antarctica does bed topography have an important control on ice flow (i.e. a better bed is needed).

To answer this question, we first require an accurate geographic model of the bed, a Digital Elevation Model with sufficient fine-scale structures (Chp. 2, Leong & Horgan, 2020b). Current generations of Antarctic bed elevation models such as BEDMAP2 (Fretwell et al., 2013) are overly smooth by necessity. BEDMAP2 is derived from Radio-echo sounding (RES) observations, the data was interpolated to a 5 km grid, and then to a 1 km grid. BedMachine Antarctica (Morlighem, 2020) is generated by mass conservation and is also smoothed in such a way that fails to capture the inherent sub-kilometre scale roughness of an ice sheet's topography as seen in paleo-ice sheets uncovered in the modern day.

The smoothness of existing interpolated bed topography products at the sub-kilometre scale is evident when looking along a transect profile. In Fig. 1.2, we show how fine scale roughness exists in ground-truth radio-echo sounding (RES) bed picks. Continent-wide bed elevation products like BEDMAP2 and BedMachine Antarctica fail to capture this roughness. Newer regional products over the Weddell Sea sector (Jeofry et al., 2018) and Princess Elizabeth Land (Cui et al., 2020) provide more accurate interpolated bed elevations but are still unable to resolve short-wavelength bed roughness. Thus, we require a method applicable to the entire continent that retains fine-scale (sub-kilometre) roughness critical for modelling ice flow (see e.g. Bingham et al., 2017; Falcini et al., 2018; Hubbard et al., 2000; Siegert et al., 2004)

One way to improve on smooth bed topographies is by using deep learning (see Goodfellow et al., 2016, for a review). Specifically, training a neural network on areas with high resolution datasets, and using it to predict what a high resolution topography would look like in areas with little to no direct observations (Chp. 2, Leong & Horgan, 2020b). Our deep learning method has similarities with inverse methods (Gudmundsson, 2011), whereby knowing ice surface elevation, velocity, surface accumulation, and other surface observations in detail allows us to infer what the bed topography might be like. In contrast to inverse methods, we introduced a specific adversarial loss function (Goodfellow et al., 2014) that penalizes overtly smooth topography, pushing bed predictions towards that of realistic groundtruth surfaces.

With the DeepBedMap dataset, we then experiment how ice flow over a rough surface differs from ice flow over smooth topography (Chp. 3). Two beds are compared using a Full Stokes ice flow model - a full physical treatment of how an ice stream flows, including the three-dimensional driving forces and stresses that govern the behaviour of an ice body (Larour et al., 2012). One outcome of this exercise is to measure the basal traction of an ice stream, separable into form drag and skin drag (Fig. 1.3, Bingham et al., 2017; Kyrke-Smith et al., 2018; Minchew & Jougin, 2020; Schoof, 2002). Form drag is basal drag due to topography (c.f. Weertman, 1957), a component which typically increases with higher resolution topography. Skin drag is the frictional force occurring at the ice-rock interface, determined by bed material properties, and significantly influenced by water that acts to decrease friction (Iverson & Zoet, 2015). Skin drag may be overestimated in comparison to form drag on glaciers such as Pine Island Glacier (Bingham et al., 2017; Kyrke-Smith et al., 2018), and this detail is of particular relevance when modelling vulnerable glaciers in the Amundsen sea sector (Kyrke-Smith et al., 2018).

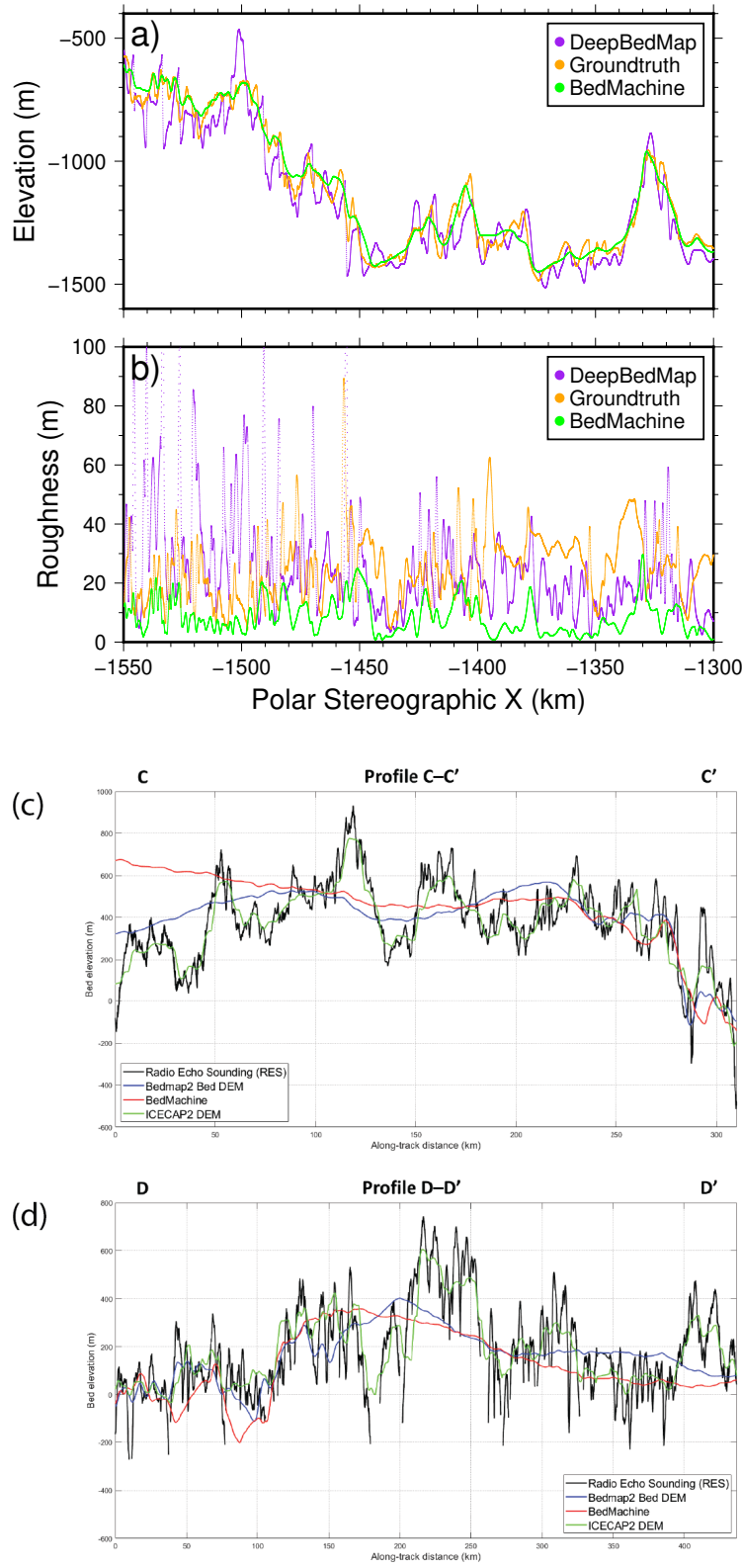


Figure 1.2: Comparing RES bed elevation measurements against different bed products along transect lines in Antarctica. Top panel is over Thwaites Glacier, showing super resolution DeepBedMap_DEM (purple; Leong & Horgan, 2020b), Ground-truth Operation IceBridge RES points (orange; Shi et al., 2010) and BedMachine Antarctica (green; Morlighem et al., 2019). Bottom panel is over Princess Elizabeth Land, showing ICECAP2 RES transects (black), BEDMAP2 (blue), BedMachine (red), and ICECAP2 DEM (green) (Fig. 6 from Cui et al., 2020, licensed under CC-BY-4.0).

Universal glacier slip law

New evidence suggests that a single glacier slip law can describe slip over the full spectrum of glacier bed types, from rough, rigid beds to deformable, sediment-covered beds. Such a universal slip law should improve projections of glacier and ice sheet mass loss.

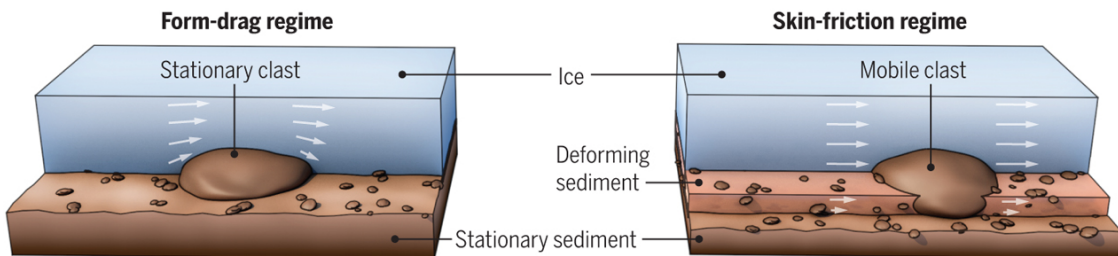
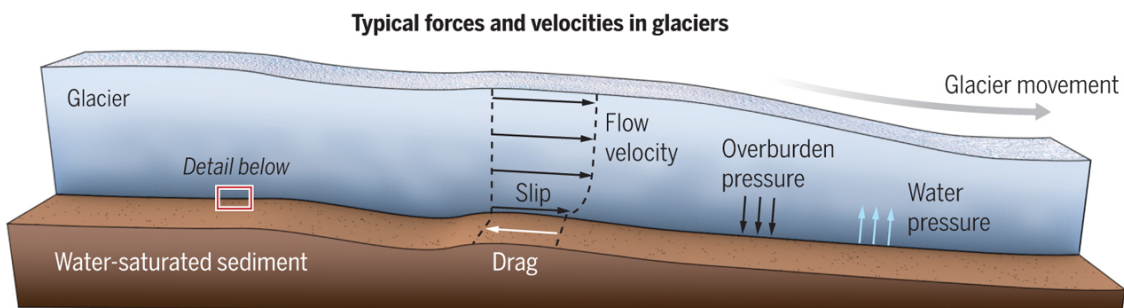
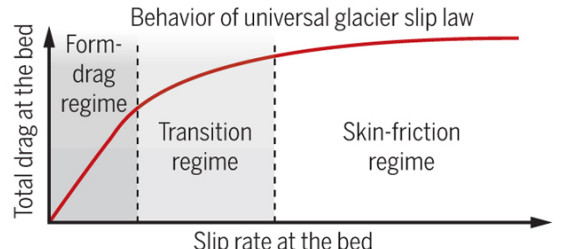


Figure 1.3: A universal glacier slip law spanning the spectrum of form drag and skin drag regimes. Figure is from Minchew and Joughin (2020). Reprinted with permission from AAAS.

Regardless of the nature of subglacial topography, water remains important in determining ice flow. Water beneath an ice sheet is dynamic, and has been shown to affect the speed of mountain glaciers (e.g. Iken et al., 1983), and that of outlet glaciers in Greenland where surface water has the ability to access the bed via moulin (Zwally, 2002). While no active moulin are known to be present in the interior regions of West and East Antarctica (Dirkscherl et al., 2020; Stokes et al., 2019), there is still a considerable volume of water trapped in subglacial lakes (Wright & Siegert, 2012). Many of these subglacial lakes are active and have drained and filled over the satellite era (Fig. 1.4, Siegfried & Fricker, 2018; B. E. Smith et al., 2009), including some that were associated with a temporary speed-ups of ice flow (e.g. Bell et al., 2007; Scambos et al., 2011; Stearns et al., 2008; Wright et al., 2014).

The subglacial hydrological system of Antarctica is very dynamic, and effort is needed to model and account for how subglacial water weakens subglacial till and induce faster sliding. The Subglacial Hydrology Model Intercomparison Project (SHMIP; De Fleurian et al., 2018) subjected a land terminating ice sheet to different subglacial hydrological schemes and forcing cycles (steady state, diurnal and seasonal), looking at how effective pressure (ice overburden pressure minus subglacial water pressure) and discharge volumes were affected. SHMIP found that complex 2-D models which include the physics of drainage systems were needed to model dynamic short term (e.g. diurnal) cycles, while simpler 0-D or 1-D models may suffice for less dynamic scenarios like those in steady state or happening on annual

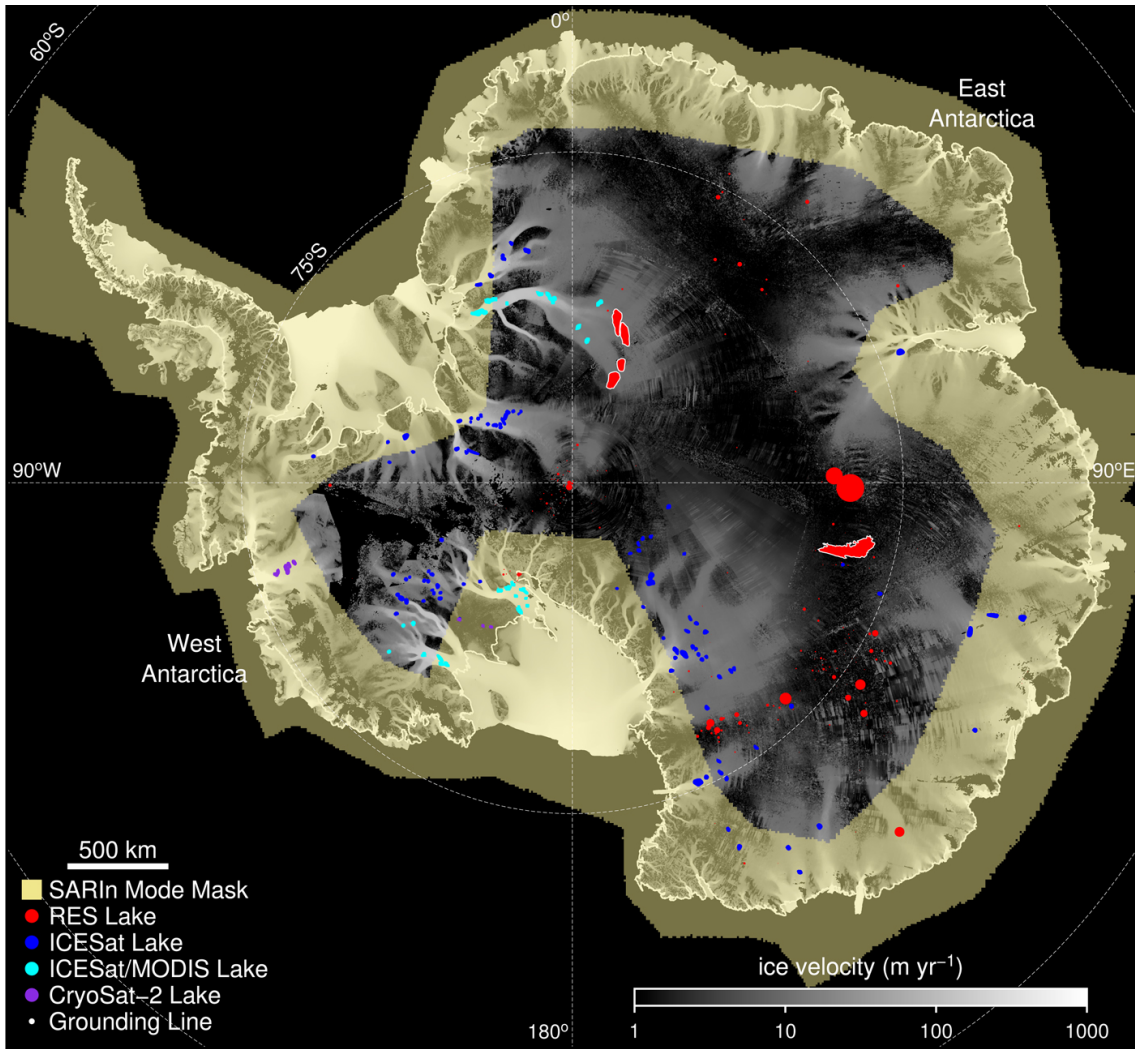


Figure 1.4: Subglacial lakes over Antarctica as detected by satellite and airborne sensors. Active subglacial lakes as detected by different satellite sensors are represented by different coloured blobs (blue, light blue and purple). Radio-echo sounding (RES) detected subglacial lakes are shown as red blobs. Figure is from Siegfried and Fricker (2018).

timescales. In Chapter 4, our findings of rapid, sub-annual transmission of subglacial water across a connected subglacial lake system suggests that 2-D models are therefore needed. Our understanding of subglacial hydrology is still inadequate as mentioned in recent model intercomparisons (ISMIP6; Seroussi et al., 2020), and research will need to focus on coupling subglacial hydrology models with ice sheet models (e.g. Smith-Johnsen et al., 2020; Sommers et al., 2018) to examine the influence of distributed vs channelized flow on ice dynamics.

One takeaway from this thesis is the need to efficiently integrate data and methods from various fields working on Antarctic glaciology. In order to inform our understanding of future ice sheet behaviour for sea level rise projections, it is crucial to make full and efficient use of the growing volume of remote sensing and field collected data in our ice sheet models. The novel machine learning and automated remote sensing methods we introduce present an exciting path forward over existing classical methods, by enabling for the efficient ingestion and merging of diverse

datasets. The bed of Antarctica may remain out of reach for the most part, but one can hope that the increasing synergy between data collectors and modellers will continue to improve our understanding of the Antarctic bed.

Chapter 2

DeepBedMap: a deep neural network for resolving the bed topography of Antarctica

Abstract

To resolve the bed elevation of Antarctica, we present DeepBedMap – a novel machine learning method that can produce Antarctic bed topography with adequate surface roughness from multiple remote sensing data inputs. The super-resolution deep convolutional neural network model is trained on scattered regions in Antarctica where high-resolution (250 m) ground-truth bed elevation grids are available. This model is then used to generate high-resolution bed topography in less surveyed areas. DeepBedMap improves on previous interpolation methods by not restricting itself to a low-spatial-resolution (1000 m) BEDMAP2 raster image as its prior image. It takes in additional high-spatial-resolution datasets, such as ice surface elevation, velocity and snow accumulation, to better inform the bed topography even in the absence of ice thickness data from direct ice-penetrating-radar surveys. The DeepBedMap model is based on an adapted architecture of the Enhanced Super-Resolution Generative Adversarial Network, chosen to minimize per-pixel elevation errors while producing realistic topography. The final product is a four-times-upsampled (250 m) bed elevation model of Antarctica that can be used by glaciologists interested in the subglacial terrain and by ice sheet modellers wanting to run catchment- or continent-scale ice sheet model simulations. We show that DeepBedMap offers a rougher topographic profile compared to the standard bicubically interpolated BEDMAP2 and BedMachine Antarctica and envision it being used where a high-resolution bed elevation model is required.

2.1 Introduction

The bed of the Antarctic ice sheet is one of the most challenging surfaces on Earth to map due to the thick layer of ice cover. Knowledge of bed elevation is however essential for estimating the volume of ice currently stored in the ice sheets and for input to the numerical models that are used to estimate the contribution ice sheets are likely to make to sea level in the coming century. The Antarctic ice sheet is estimated to hold a sea level equivalent (SLE) of 57.9 ± 0.9 m (Morlighem

et al., 2019). Between 2012 and 2017, the Antarctic ice sheet was losing mass at an average rate of $219 \pm 43 \text{ Gt yr}^{-1}$ ($0.61 \pm 0.12 \text{ mm yr}^{-1}$ SLE), with most of the ice loss attributed to the acceleration, retreat and rapid thinning of major West Antarctic Ice Sheet outlet glaciers (IMBIE, 2018). Bed elevation exerts additional controls on ice flow by routing subglacial water and providing frictional resistance to flow (Siegert et al., 2004). Bed roughness, especially at short wavelengths, exerts a frictional force against the flow of ice, making it an important influence on ice velocity (Bingham et al., 2017; Falcini et al., 2018). The importance of bed elevation has led to major efforts to compile bed elevation models of Antarctica, notably with the BEDMAP1 (Lythe & Vaughan, 2001) and BEDMAP2 (Fretwell et al., 2013) products. A need for a higher-spatial-resolution digital elevation model (DEM) is also apparent, as ice sheet models move to using sub-kilometre grids in order to quantify glacier ice flow dynamics more accurately (Graham et al., 2017; Le Brocq et al., 2010). Finer grids are especially important at the ice sheet's grounding zone on which adaptive mesh refinement schemes have focused (e.g. Cornford et al., 2016), and attention to the bed roughness component is imperative for proper modelling of fast-flowing outlet glaciers (Durand et al., 2011; Nias et al., 2016). Here we address the challenge of producing a high-resolution DEM while preserving a realistic representation of the bed terrain's roughness.

Estimating bed elevation directly from geophysical observations primarily uses ice-penetrating-radar methods (e.g. Robin et al., 1970). Airborne radar methods enable reliable along-track estimates with low uncertainty (around the 1% level) introduced by imperfect knowledge of the firn and ice velocity structure, with some potential uncertainty introduced by picking the bed return. Radar-derived bed estimates remain limited in their geographic coverage (Fretwell et al., 2013) and are typically anisotropic in their coverage, with higher spatial sampling in the along-track direction than between tracks.

To overcome these limitations, indirect methods of estimating bed elevation have been developed, and these include inverse methods and spatial statistical methods. Inverse methods use surface observations combined with glaciological-process knowledge to determine ice thickness (e.g. van Pelt et al., 2013). A non-linear relationship exists between the thickness of glaciers, ice streams and ice sheets and how they flow (Raymond & Gudmundsson, 2005), meaning one can theoretically use a well-resolved surface to infer bed properties (e.g. Farinotti et al., 2009). Using surface observation inputs, such as the glacier outline, surface digital elevation models, surface mass balance, surface rate of elevation change, and surface ice flow velocity, various models have been tested in the Ice Thickness Models Intercomparison eXperiment (ITMIX; Farinotti et al., 2017) to determine ice thickness (surface elevation minus bed elevation). While significant inter-model uncertainties do exist, they can be mitigated by combining several models in an ensemble to provide a better consensus estimate (Farinotti et al., 2019). On a larger scale, the inverse technique has also been applied to the Greenland (Morlighem et al., 2017) and Antarctic (Morlighem et al., 2019) ice sheets, specifically using the mass conservation approach (Morlighem et al., 2011). Spatial statistical methods seek to derive a higher-spatial-resolution bed by applying the topographical likeness of bed features known to great detail in one area to other regions. For example, the conditional simulation method applied by Goff et al. (2014) is able to resolve both fine-scale roughness and channelized morphology over the complex topography of Thwaites Glacier and make use of the fact that roughness statistics are different between highland and lowland areas. Graham

et al. (2017) uses a two-step approach to generate their synthetic high-resolution grid, with the high-frequency roughness component coming from the ICECAP and BEDMAP1 compilation radar point data and the low-frequency component coming from BEDMAP2. Neither method is perfect, and we see all of the above methods as complementary.

We present a deep-neural-network method that is trained on direct ice-penetrating-radar observations over Antarctica and one which has features from both the indirect inverse modelling and spatial statistical methodologies. An artificial neural network, loosely based on biological neural networks, is a system made up of neurons. Each neuron comprises a simple mathematical function that takes an input to produce an output value, and neural networks work by combining many of these neurons together. The term deep neural network is used when there is not a direct function mapping between the input data and final output but two or more layers that are connected to one another (see LeCun et al., 2015, for a review). They are trained using backpropagation, a procedure whereby the weights or parameters of the neurons’ connections are adjusted so as to minimize the error between the ground truth and output of the neural network (Rumelhart et al., 1986). Similar work has been done before using artificial neural networks for estimating bed topography (e.g. Clarke et al., 2009; Monnier & Zhu, 2018), but to our knowledge, no-one so far in the glaciological community has attempted to use convolutional neural networks that work in a more spatially aware, 2-dimensional setting. Convolutional neural networks differ from standard artificial neural networks in that they use kernels or filters in place of regular neurons (again, see LeCun et al., 2015, for a review). The techniques we employ are prevalent in the computer vision community, having existed since the 1980s (Fukushima & Miyake, 1982; LeCun et al., 1989) and are commonly used in visual pattern recognition tasks (e.g. Krizhevsky et al., 2012; Lecun et al., 1998). Our main contributions are twofold: we (1) present a high-resolution (250 m) bed elevation map of Antarctica that goes beyond the 1 km resolution of BEDMAP2 (Fretwell et al., 2013) and (2) design a deep convolutional neural network to integrate as many remote sensing datasets as possible which are relevant to estimating Antarctica’s bed topography. We name the neural network “DeepBedMap”, and the resulting digital elevation model (DEM) product “DeepBedMap_DEM”.

2.2 Related Work

2.2.1 Super-Resolution

Super resolution involves the processing of a low-resolution raster image into a higher-resolution one (R. Tsai & Huang, 1984). The idea is similar to the work on enhancing regular photographs to look crisper. The problem is especially ill-posed because a specific low-resolution input can correspond to many possible high-resolution outputs, resulting in the development of several different algorithms aimed at solving this challenge (see Nasrollahi & Moeslund, 2014, for a review). One promising approach is to use deep neural networks (LeCun et al., 2015) to learn an end-to-end mapping between the low- and high-resolution images, a method coined the Super-Resolution Convolutional Neural Network (SRCNN; Dong et al., 2014). Since the development of SRCNN, multiple advances have been made to improve the perceptual quality of super-resolution neural networks (see W. Yang et al., 2019, for a review). One way is to use a better loss function, also known as a cost function. A

loss function is a mathematical function that represents the error between the output of the neural network and the ground truth (see also Appendix A). By having an adversarial component in its loss function, the Super-Resolution Generative Adversarial Network (SRGAN; Ledig et al., 2017) manages to produce super-resolution images with finer perceptual details. A generative adversarial network (Goodfellow et al., 2014) consists of two neural networks, a generator and a discriminator. A common analogy used is to treat the generator as an artist that produces imitation paintings and the discriminator as an art critic that determines the authenticity of the paintings. The artist wants to fool the critic into believing its paintings are real, while the critic tries to identify problems with the painting. Over time, the artist or generator model learns to improve itself based on the critic’s judgement, producing authentic-looking paintings with high perceptual quality. Perceptual quality is the extent to which an image looks like a valid natural image, usually as judged by a human. In this case, perceptual quality is quantified mathematically by the discriminator or critic taking into account high-level features of an image like contrast, texture, etc. Another way to improve performance is by reconfiguring the neural network’s architecture, wherein the layout or building blocks of the neural network are changed. By removing unnecessary model components and adding residual connections (He et al., 2015), an enhanced deep super-resolution network (EDSR; Lim et al., 2017) features a deeper neural network model that has better performance than older models. For the DeepBedMap model, we choose to adapt the Enhanced Super-Resolution Generative Adversarial Network (ESRGAN; X. Wang et al., 2019) which brings together the ideas mentioned above. This approach produces state-of-the-art perceptual quality and won the 2018 Perceptual Image Restoration and Manipulation Challenge on Super Resolution (Third Region; Blau et al., 2018).

2.2.2 Network Conditioning

Network conditioning means having a neural network process one source of information in the context of other sources (Dumoulin et al., 2018). In a geographic context, conditioning is akin to using not just one layer but also other relevant layers with meaningful links to provide additional information for the task at hand. Many ways exist to insert extra conditional information into a neural network, such as concatenation-based conditioning, conditional biasing, conditional scaling and conditional affine transformations (Dumoulin et al., 2018). We choose to use the concatenation-based conditioning approach, whereby all of the individual raster images are concatenated together channel-wise, much like the individual bands of a multispectral satellite image. This was deemed the most appropriate conditioning method as all the contextual remote sensing datasets are raster grid images and also because this approach aligns with related work in the remote sensing field.

An example similar to this DEM super-resolution problem is the classic problem of pan-sharpening, whereby a blurry low-resolution multispectral image conditioned with a high-resolution panchromatic image can be turned into a high-resolution multispectral image. There is ongoing research into the use of deep convolutional neural networks for pan-sharpening (Masi et al., 2016; Scarpa et al., 2018), sometimes with the incorporation of specific domain knowledge (J. Yang et al., 2017), all of which show promising improvements over classical image processing methods. More recently, generative adversarial networks (Goodfellow et al., 2014) have been used in the conditional sense for general image-to-image translation tasks (e.g. Isola

et al., 2016; Park et al., 2019), and also for producing more realistic pan-sharpened satellite images (Liu et al., 2018). Our DeepBedMap model builds upon these ideas and other related DEM super-resolution work (Chen et al., 2016; Xu et al., 2015), while incorporating extra conditional information specific to the cryospheric domain for resolving the bed elevation of Antarctica.

2.3 Data and Methods

2.3.1 Data Preparation

Our convolutional neural network model works on 2-D images, so we ensure all the datasets are in a suitable raster grid format. Ground-truth bed elevation points picked from radar surveys (see Table 2.1) are first compiled together onto a common Antarctic stereographic projection (EPSG:3031) using the WGS84 datum, reprojecting where necessary. These points are then gridded onto a 250 m spatial resolution (pixel-node-registered) grid. We preprocess the points first using Generic Mapping Tools v6.0 (GMT6; Wessel et al., 2019), computing the median elevation for each pixel block in a regular grid. The preprocessed points are then run through an adjustable-tension continuous-curvature spline function with a tension factor set to 0.35 to produce a digital elevation model grid. This grid is further post-processed to mask out pixels that are more than 3 pixels (750 m) from the nearest ground-truth point.

Table 2.1: High-resolution ground-truth datasets from ice-penetrating-radar surveys (collectively labelled as y) used to train the DeepBedMap model. Training site locations can be seen in Fig. 2.2.

Location	Citation
Pine Island Glacier	Bingham et al. (2017)
Wilkes Subglacial Basin	Jordan et al. (2010)
Carlson Inlet	King (2011)
Rutford Ice Stream	King et al. (2016)
Various locations in Antarctica	Shi et al. (2010)

To create the training dataset, we use a sliding window to obtain square tiles cropped from the high-resolution (250 m) ground-truth bed elevation grids, with each tile required to be completely filled with data (i.e. no Not a Number – NaN – values). Besides these ground-truth bed elevation tiles, we also obtain other tiled inputs (see Table 2.2) corresponding to the same spatial bounding box area. To reduce border edge artefacts in the prediction, the neural network model’s input convolutional layers (see Fig. 2.1) use no padding (also known as “valid” padding) when performing the initial convolution operation. This means that the model input grids (x, w^1, w^2, w^3) have to cover a larger spatial area than the ground-truth grids (y). More specifically, the model inputs cover an area of $11\text{ km} \times 11\text{ km}$ (e.g. $11\text{ pixels} \times 11\text{ pixels}$ for BEDMAP2), while the ground-truth grids cover an area of $9\text{ km} \times 9\text{ km}$ ($36\text{ pixels} \times 36\text{ pixels}$). As the pixels of the ground-truth grids may not align perfectly with those of the model’s input grids, we use bilinear interpolation to ensure that all the input grids cover the same spatial bounds as those of the reference ground-truth tiles. The general locations of these training tiles are shown in orange in Fig. 2.2.

Table 2.2: Remote sensing dataset inputs into the DeepBedMap neural network model.

Symbol	Name	Variable	Spatial resolution	Citation
x	BEDMAP2	bed elevation (m)	1000 m	Fretwell et al. (2013)
w^1	REMA	surface elevation (m)	100 m ^b	Howat et al. (2018)
w^2	MEaSUREs Ice Velocity	VX, VY (m yr ⁻¹) ^a	500 m ^c	Mouginot et al. (2019a)
w^3	Antarctic snow accumulation	snow accumulation rate (kg m ⁻² yr ⁻¹)	1000 m	Arthern et al. (2006)

^a Note that the x and y components of velocity are used here instead of the norm.

^b Gaps in 100 m mosaic filled in with bilinear resampled 200 m resolution REMA image.

^c Originally 450 m; bilinear resampled to 500 m.

2.3.2 Model Design

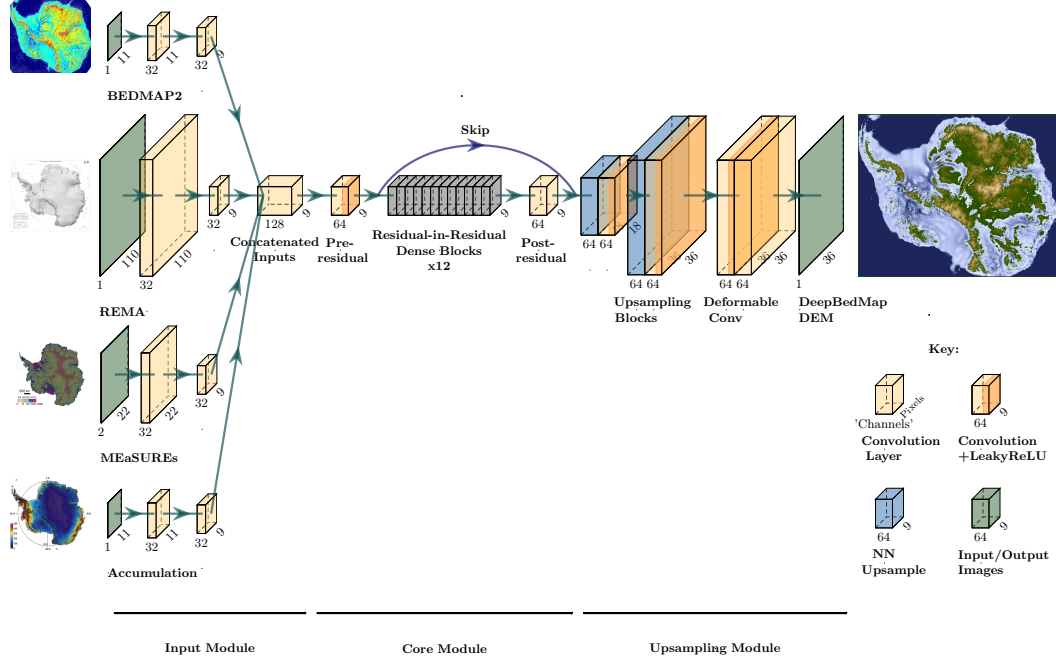


Figure 2.1: DeepBedMap generator model architecture composed of three modules. The input module processes each of the four inputs (BEDMAP2, Fretwell et al., 2013; REMA, Howat et al., 2019; MEaSUREs Ice Velocity, Mouginot et al., 2019b; snow accumulation, Arthern et al., 2006; see also Table 2.2) into a consistent tensor. The core module processes the rich information contained within the concatenated inputs. The upsampling module scales the tensor up by 4 times and does some extra processing to produce the output DeepBedMap_DEM.

Our DeepBedMap model is a generative adversarial network (Goodfellow et al., 2014) composed of two convolutional neural network models, a generator G_θ that produces the bed elevation prediction and a discriminator D_η critic that will judge the quality of this output. The two models are trained to compete against each other, with the generator trying to produce images that are misclassified as real by the discriminator and the discriminator learning to spot problems with the generator's prediction in relation to the ground truth. Following this is a mathematical definition of the neural network models and their architecture.

The objective of the main super-resolution generator model G_θ is to produce a high-resolution (250 m) grid of Antarctica's bed elevation \hat{y} given a low-resolution (1000 m) BEDMAP2 (Fretwell et al., 2013) image x . However, the information contained in BEDMAP2 is insufficient for this regular super-resolution task, so we provide the neural network with more context through network conditioning (see Sect. 2.2.2). Specifically, the model is conditioned at the input block stage with three raster grids (see Table 2.2): (1) ice surface elevation w^1 , (2) ice surface velocity w^2 and (3) snow accumulation w^3 . This can be formulated as follows:

$$\hat{y} = G_\theta(x, w^1, w^2, w^3), \quad (2.1)$$

where G_θ is the generator (see Fig. 2.1) that produces high-resolution image candidates \hat{y} . For brevity in the following equations, we simplify Eq. (2.1) to hide

conditional inputs w^1, w^2 and w^3 , so that all input images are represented using x . To train the generative adversarial network, we update the parameters of the generator θ and discriminator η as follows:

$$\hat{\theta} = \arg \min_{\theta} \frac{1}{N} \sum_{n=1}^N L_G(\hat{y}_n, y_n), \quad (2.2)$$

$$\hat{\eta} = \arg \min_{\eta} \frac{1}{N} \sum_{n=1}^N L_D(\hat{y}_n, y_n), \quad (2.3)$$

where new estimates of the neural network parameters $\hat{\theta}$ and $\hat{\eta}$ are produced by minimizing the total loss functions L_G and L_D , respectively, for the generator G and discriminator D and \hat{y}_n and y_n are the set of predicted and ground-truth high-resolution images over N training samples. The generator network's loss L_G is a custom perceptual loss function with four weighted components – content, adversarial, topographic and structural loss. The discriminator network's loss L_D is designed to maximize the likelihood that predicted images are classified as fake (0) and ground-truth images are classified as real (1). Details of these loss functions are described in Appendix A.

Noting that the objective of the Generator G is opposite to that of the Discriminator D , we formulate the adversarial min-max problem following Goodfellow et al. (2014) as so:

$$\begin{aligned} \min_G \max_D V(G, D) = & \mathbb{E}_{y \sim P_{\text{data}}(y)} [\ln D(y)] \\ & + \mathbb{E}_{x \sim P_{G(x)}} [\ln(1 - D(G(x)))] \end{aligned} \quad (2.4)$$

where for the discriminator D , we maximize the expectation \mathbb{E} or the likelihood that the probability distribution of the discriminator's output fits $D(y) = 1$ when $y \sim P_{\text{data}}(y)$; i.e. we want the discriminator to classify the high-resolution image as real (1) when the image y is in the distribution of the ground-truth images $P_{\text{data}}(y)$. For the generator G , we minimize the likelihood that the discriminator classifies the generator output $D(G(x)) = 0$ when $x \sim P_{G(x)}$; i.e. we do not want the discriminator to classify the super-resolution image as fake (0) when the inputs x are in the distribution of generated images $P_{G(x)}$. The overall goal of the entire network is to make the distribution of generated images $G(x)$ as similar as possible to the ground truth y through optimizing the value function V .

DeepBedMap's model architecture is adapted from the Enhanced Super-Resolution Generative Adversarial Network (ESRGAN; X. Wang et al., 2019). The generator model G (see Fig. 2.1) consists of an input, core and upsampling module. The input module is made up of four sub-networks, each one composed of a convolutional neural network that processes the input image into a consistent 9×9 shaped tensor. Note that the MEaSURES Ice Velocity (Mouginot et al., 2019b) input has two channels, one each for the x and y velocity components. All the processed inputs are then concatenated together channel-wise before being fed into the core module. The core module is based on the ESRGAN architecture with 12 residual-in-residual dense blocks (see X. Wang et al., 2019, for details), saddled in between a pre-residual and post-residual convolutional layer. A skip connection runs from the pre-residual

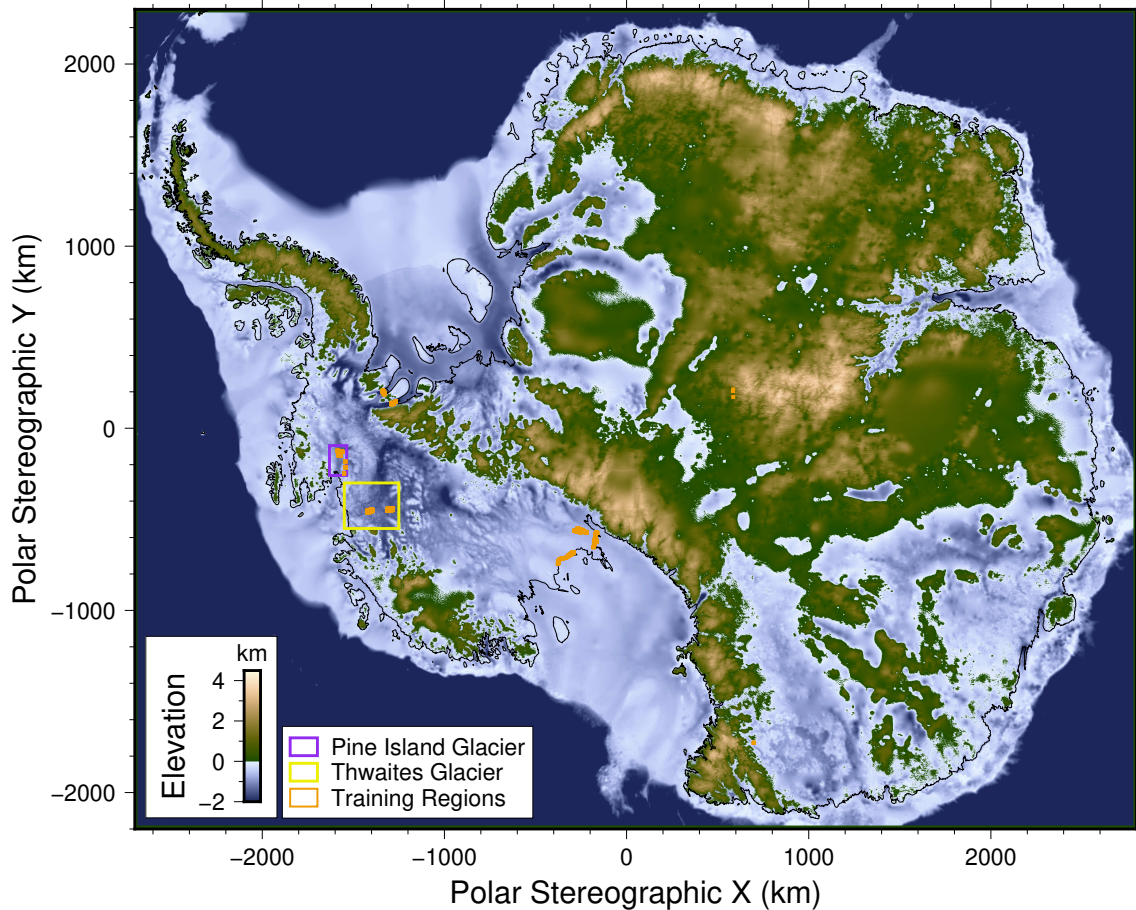


Figure 2.2: DeepBedMap_DEM over the entire Antarctic continent. Plotted on an Antarctic stereographic projection (EPSG:3031) with elevation referenced to the WGS84 datum. Grounding line is plotted as thin black line. Purple box shows Pine Island Glacier extent used in Fig. 2.3. Yellow box shows Thwaites Glacier extent used in Fig. 2.5. Orange areas show locations of training tiles (see Table 2.1).

layer's output to the post-residual layer's output before being fed into the upsampling module. This skip connection (He et al., 2016) helps with the neural network training process by allowing the model to also consider minimally processed information from the input module, instead of solely relying on derived information from the residual-block layers when performing the upsampling. The upsampling module is composed of two upsampling blocks, specifically a nearest-neighbour upsampling followed by a convolutional layer and leaky rectified linear unit (LeakyReLU; Maas et al., 2013) activation, which progressively scales the tensors by 2 times each time. Following this are two deformable convolutional layers (Dai et al., 2017) which produce the final-output super-resolution DeepBedMap_DEM. This generator model is trained to gradually improve its prediction by comparing the predicted output with ground-truth images in the training regions (see Fig. 2.2), using the total loss function defined in Eq. (A.9).

The main differences between the DeepBedMap generator model and ESRGAN are the custom input block at the beginning and the deformable convolutional layers at the end. The custom input block is designed to handle the prior low-resolution BEDMAP2 image and conditional inputs (see Table 2.2). Deformable convolution was chosen in place of the standard convolution so as to enhance the model's pre-

dictive capability by having it learn dense spatial transformations.

Besides the generator model, there is a separate adversarial discriminator model D (not shown in the paper). Again, we follow ESRGAN’s (X. Wang et al., 2019) lead by implementing the adversarial discriminator network in the style of the Visual Geometry Group convolutional neural network model (VGG; Simonyan & Zisserman, 2014). The discriminator model consists of 10 blocks made up of a convolutional, batch normalization (Ioffe & Szegedy, 2015) and LeakyReLU (Maas et al., 2013) layer, followed by two fully connected layers comprised of 100 neurons and 1 neuron, respectively. For numerical stability, we omit the final fully connected layer’s sigmoid activation function from the discriminator model’s construction, integrating it instead into the binary cross-entropy loss functions at Eqs. (A.2) and (A.3) using the log-sum-exp function. The output of this discriminator model is a value ranging from 0 (fake) to 1 (real) that scores the generator model’s output image. This score is used by both the discriminator and generator in the training process and helps to push the predictions towards more realistic bed elevations. More details of the neural network training setup can be found in Appendix B.

2.4 Results

2.4.1 DeepBedMap_DEM Topography

Here we present the output digital elevation model (DEM) of the super-resolution DeepBedMap neural network model and compare it with bed topography produced by other methods. The resulting DEM has a 250 m spatial resolution and therefore a four-times upsampled bed elevation grid product of BEDMAP2 (Fretwell et al., 2013). In Fig. 2.2, we show that the full Antarctic-wide DeepBedMap_DEM manages to capture general topographical features across the whole continent. The model is only valid for grounded-ice regions, but we have produced predictions extending outside of the grounding-zone area (including ice shelf cavities) using the same bed elevation, surface elevation, ice velocity and snow accumulation inputs where such data are available up to the ice shelf front. We emphasize that the bed elevation under the ice shelves has not been super resolved properly and is not intended for ice sheet modelling use. Users are encouraged to cut the DeepBedMap_DEM using their preferred grounding line (e.g. Bindschadler et al., 2011; Mouginot et al., 2017; Rignot et al., 2011) and replace the under-ice-shelf areas with another bathymetry grid product (e.g. GEBCO Bathymetric Compilation Group 2020, 2020). The transition from the DeepBedMap_DEM to the bathymetry product across the grounding zone can then be smoothed using inverse distance weighting or an alternative interpolation method.

We now highlight some qualitative observations of DeepBedMap_DEM’s bed topography beneath Pine Island Glacier (Figure 2.3) and other parts of Antarctica (Figure 2.4). DeepBedMap_DEM shows a terrain with realistic topographical features, having fine-scale bumps and troughs that makes it rougher than that of BEDMAP2 (Fretwell et al., 2013) and BedMachine Antarctica (Morlighem, 2019) while still preserving the general topography of the area (Figure 2.3). Over steep topographical areas such as the Transantarctic Mountains (Figure 2.4a, 2.4h), DeepBedMap produced speckle (**S**) texture patterns. Along fast flowing ice streams and glaciers (Figure 2.4b, 2.4c, 2.4d, 2.4e, 2.4f, 2.4g, 2.4h), we can see ridges (**R**) aligned parallel to the sides of the valley, i.e. along flow. In some cases, the ridges

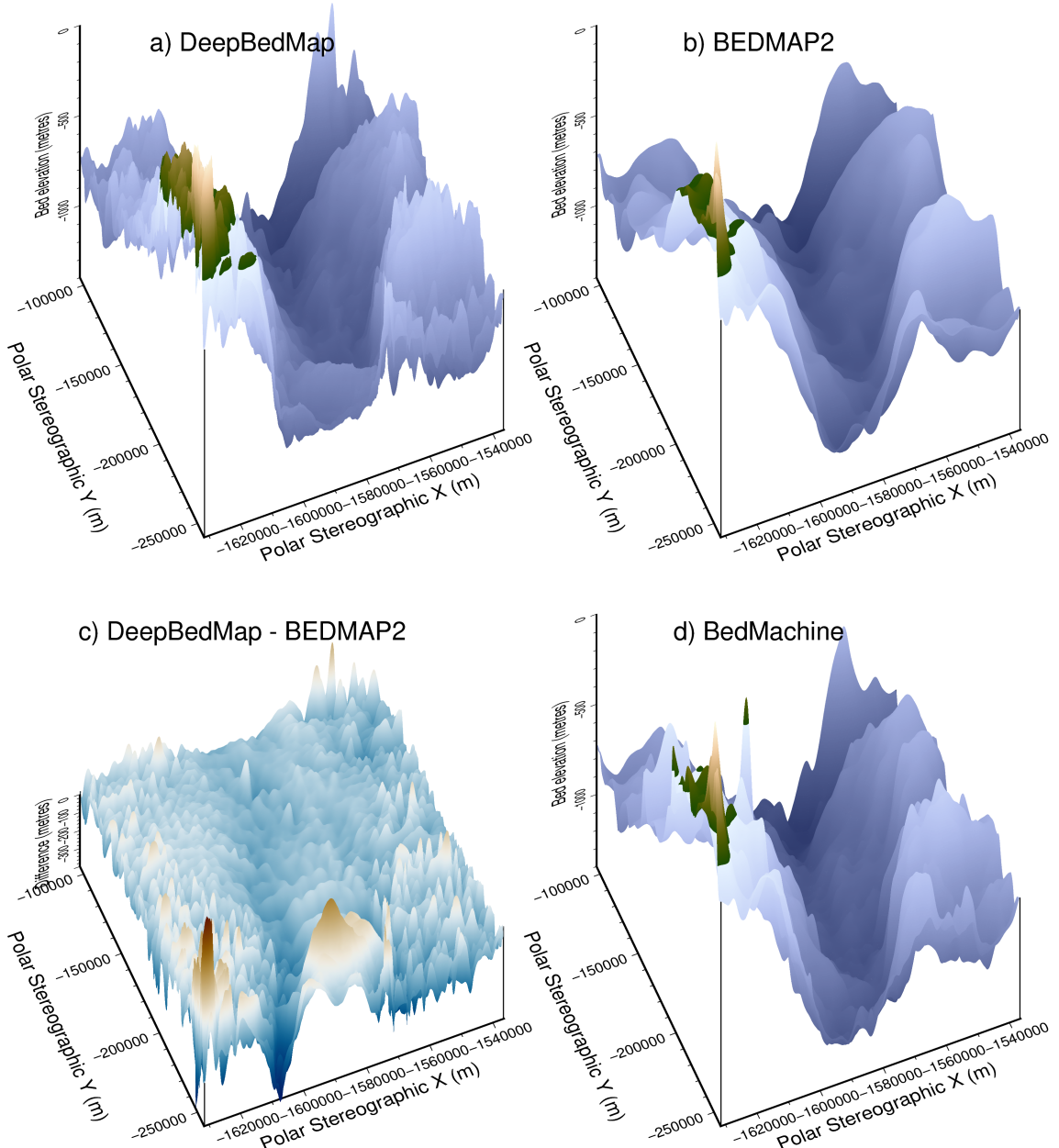


Figure 2.3: Comparison of interpolated bed elevation grid products over Pine Island Glacier (see extent in Figure 2.2). **a** DeepBedMap (ours) at 250 m resolution. **b** BEDMAP2 (Fretwell et al., 2013), originally 1000 m, bicubic interpolated to 250 m. **c** Elevation Difference between DeepBedMap and BEDMAP2. **d** BedMachine Antarctica (Morlighem, 2019), originally 500 m, bicubic interpolated to 250 m.

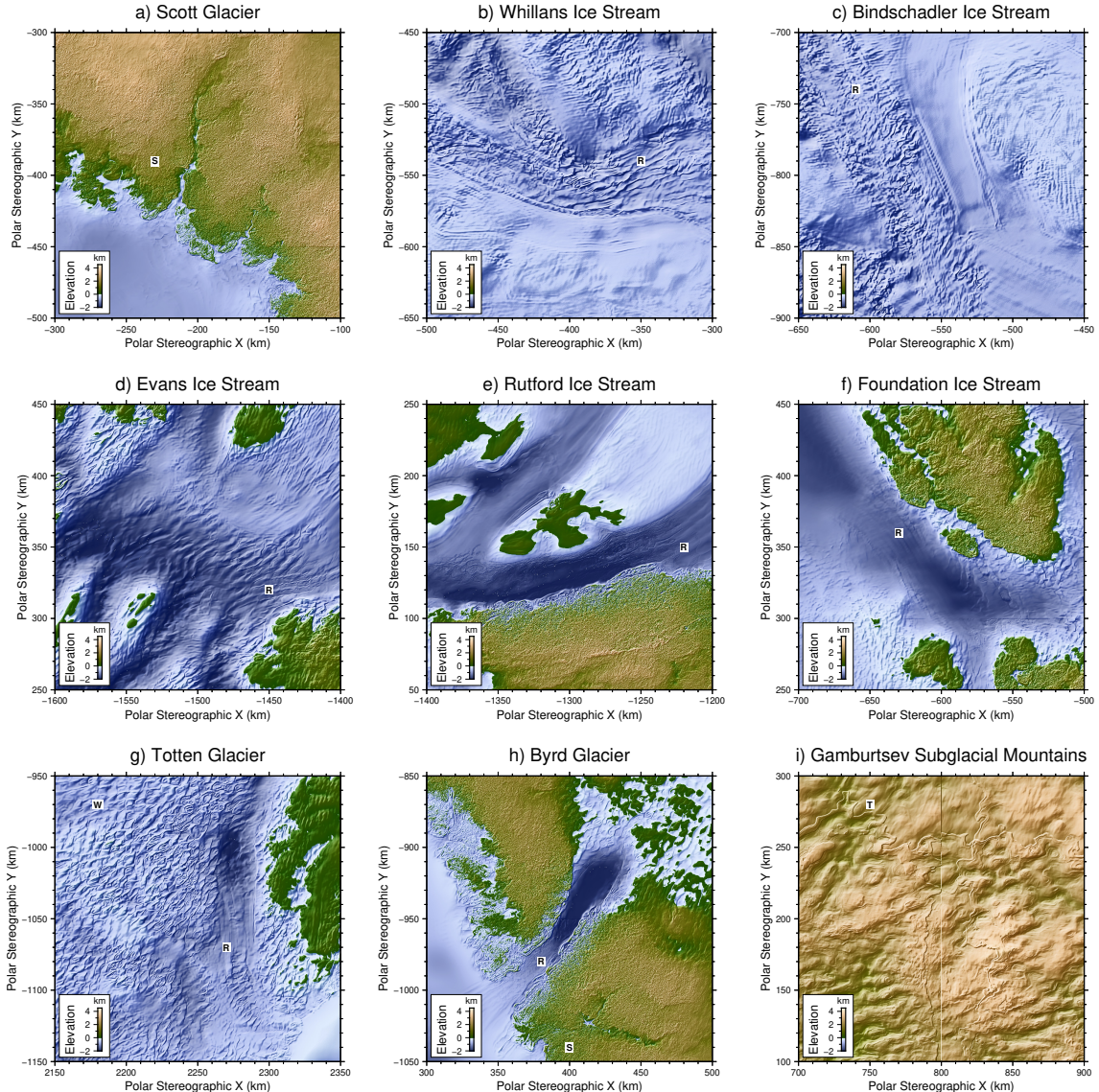


Figure 2.4: Close-up views of DeepBedMap_DEM around Antarctica. Panels (a–c) show Siple Coast locations. Panels (d–f) show Weddell Sea region locations. Panels (g–i) show East Antarctica locations. Features of interest are annotated in black text against a white background: ridges R, speckle patterns S, terraces T, wave patterns W.

are also oriented perpendicular to the flow direction such at Whillans Ice Stream (Figure 2.4b), Bindschadler Ice Stream (Figure 2.4c) and Totten Glacier (Figure 2.4g), resulting in intersecting ridges that creates a box-like, honeycomb structure. Over relatively flat regions in both West and East Antarctica (e.g. Figure 2.4g), there are some hummocky, wave-like (**W**) patterns occasionally represented in the terrain. Terrace (**T**) features can occasionally be found winding along the side of hills such as at the Gamburtsev Subglacial Mountains (Figure 2.4i).

2.4.2 Surface Roughness

We compare the roughness of DeepBedMap_DEM vs. BedMachine Antarctica with ground-truth grids from processed Operation IceBridge data (Shi et al., 2010) using standard deviation SD as a simple measure of roughness (Rippin et al., 2014). We calculate the surface roughness for a single 250 m pixel from the SD of elevation values over a square 1250 m \times 1250 m area (i.e. 5 pixels \times 5 pixels) surrounding the central pixel. Focusing on Thwaites Glacier, the spatial 2-D view of the DeepBedMap_DEM (Fig. 2.5a) shows a range of typical topographic features such as hills and canyons. The calculated 2-D roughnesses for both DeepBedMap_DEM (Fig. 2.5b) and the Ground truth (Fig. 2.5c) lie in a similar range from 0 to 400 m, whereas the roughness of BedMachine Antarctica (Fig. 2.5d) is mostly in the 0-to-200 m range (hence the different colour scale). Also, the roughness pattern for both DeepBedMap_DEM and the ground truth has a more distributed cluster pattern made up of little pockets (especially towards the coastal region on the left; see Fig. 2.5b and c), whereas the BedMachine Antarctica roughness pattern shows larger cluster pockets in isolated regions (see Fig. 2.5d).

Taking a 1-D transect over the 250 m resolution DeepBedMap_DEM, BedMachine Antarctica and ground-truth grids, we illustrate the differences in bed topography and roughness from the coast towards the inland area of Thwaites Glacier with a flight trace from Operation IceBridge (see Fig. 2.6). For better comparison, we have calculated the Operation IceBridge ground-truth bed elevation and roughness values from a resampled 250 m grid instead of using its native along-track resolution. All three elevation profiles are shown to follow the same general trend from the relatively rough coastal region (Fig. 2.6a from -1550 to -1500 km on the x scale), along the retrograde slope (Fig. 2.6a from -1500 to -1450 km on the x scale) and into the interior region. DeepBedMap_DEM features a relatively noisy elevation profile with multiple fine-scale (< 10 km) bumps and troughs similar to the ground truth, while BedMachine Antarctica shows a smoother profile that is almost a moving average of the ground-truth elevation (Fig. 2.6a). Looking at the roughness statistic (Fig. 2.6b), both the DeepBedMap_DEM and Operation IceBridge ground-truth grids have a mean SD of about 40 m, whereas BedMachine Antarctica has a mean of about 10 m and rarely exceeds a SD value of 20 m along the transect.

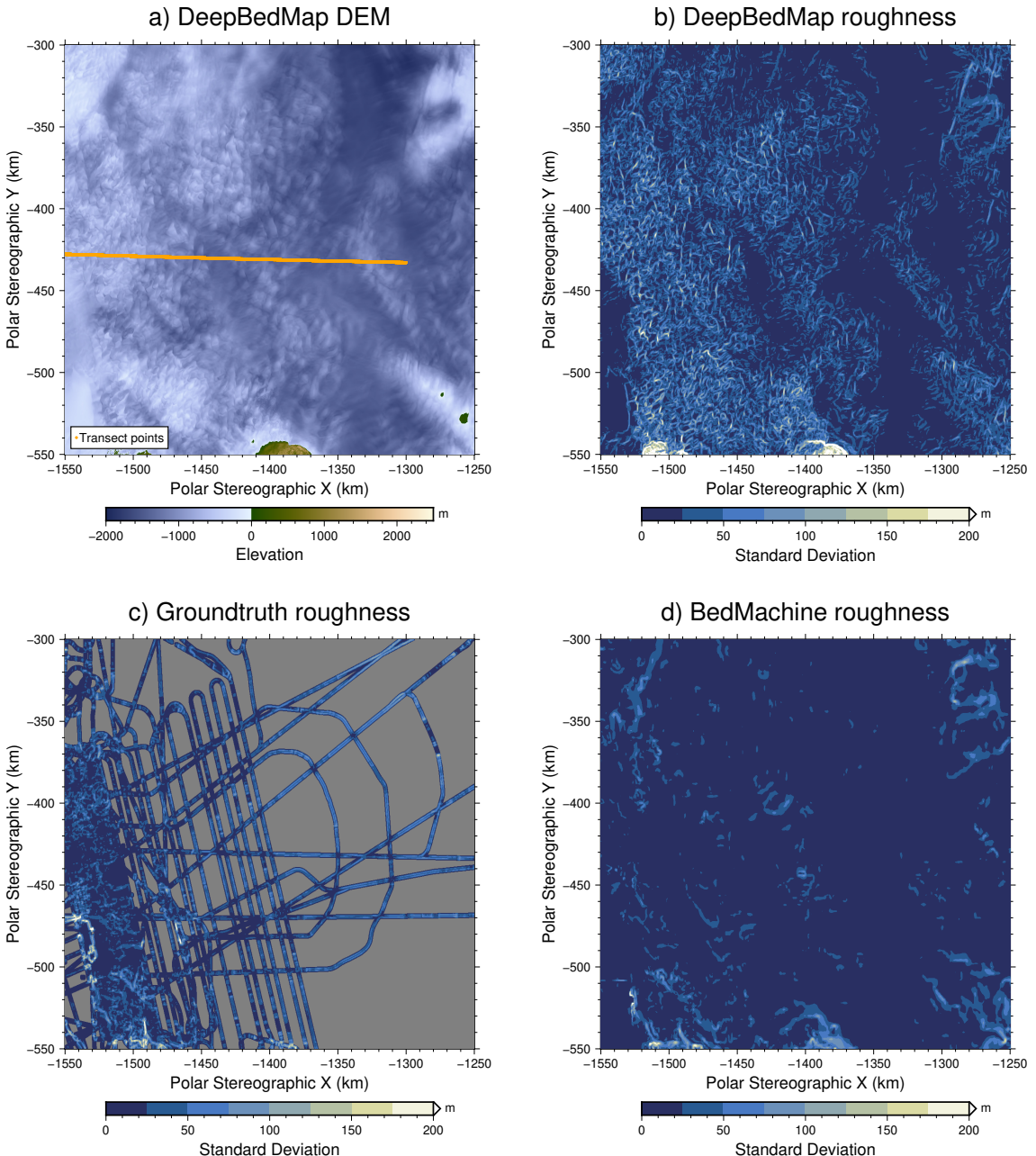


Figure 2.5: Spatial 2-D view of grids over Thwaites Glacier, West Antarctica. Plotted on an Antarctic stereographic projection (EPSG:3031) with elevation and SD values referenced to the WGS84 datum. **(a)** DeepBedMap digital elevation model. **(b)** 2-D roughness from the DeepBedMap_DEM grid. **(c)** 2-D roughness from interpolated Operation IceBridge grid. **(d)** 2-D roughness from bicubically interpolated BedMachine Antarctica grid. Orange points in **(a)** correspond to transect sampling locations used in Fig. 2.6.

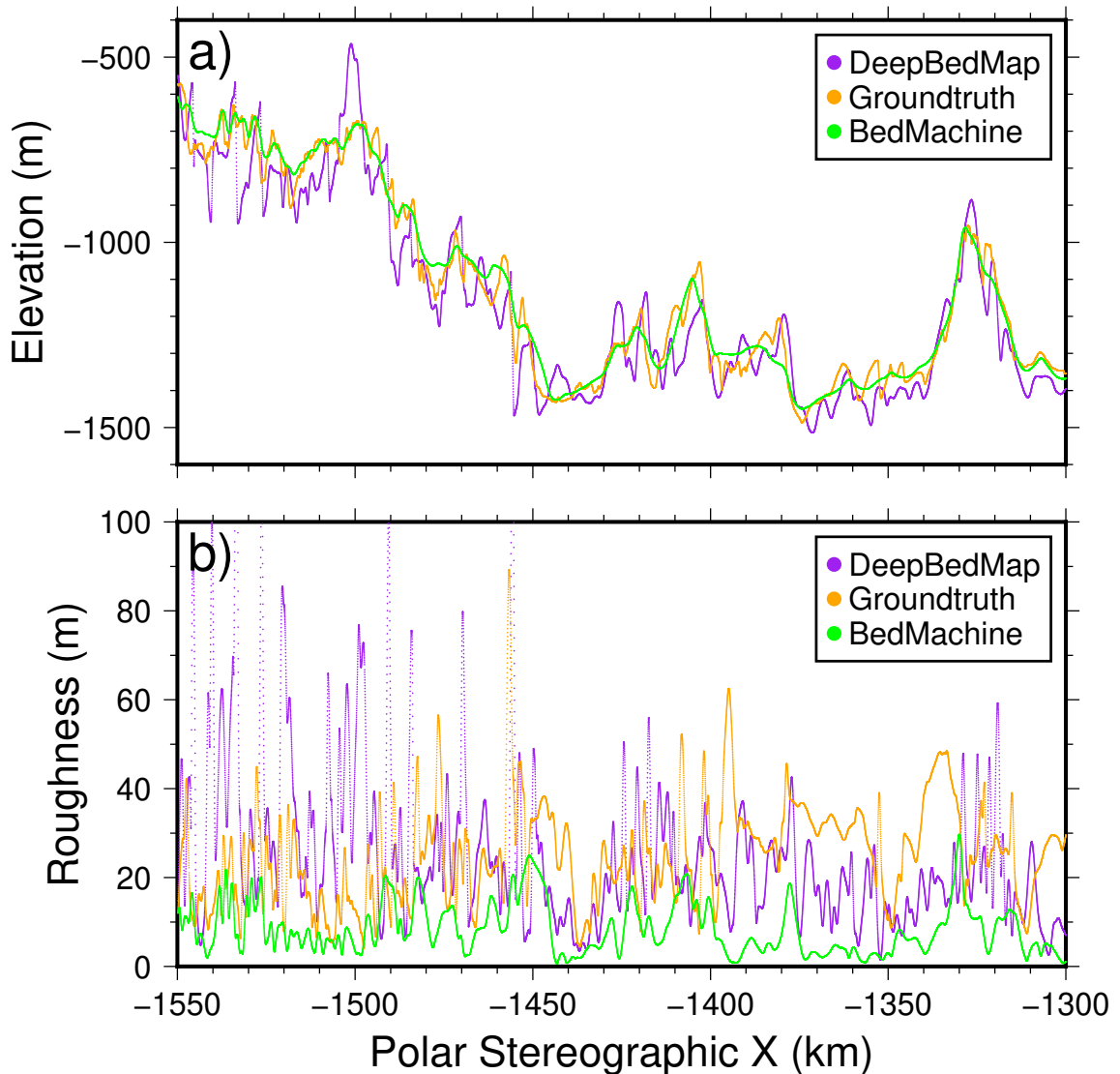


Figure 2.6: Comparing bed elevation (**a**) and surface roughness (**b**) (SD of elevation values) of each interpolated grid product (250 m resolution) over a transect (see Fig. 2.5 for location of transect line). Purple values are from the super-resolution DeepBedMap_DEM; orange values are from tension-spline-interpolated Operation IceBridge ground-truth points; green values are from bicubically interpolated BedMachine Antarctica.

2.5 Discussion

2.5.1 Bed Features

In Sect. 2.4.1, we show that the DeepBedMap model has produced a high-resolution (250 m) result (see Fig. 2.3) that can capture a detailed picture of the underlying bed topography. The fine-scale bumps and troughs are the result of the DeepBedMap generator model learning to produce features that are similar to those found in the high-resolution ground-truth datasets it was trained on. However, there are also artefacts produced by the model. For example, the winding terrace (T, Fig. 2.4) features are hard to explain, and though they resemble eskers (Drews et al., 2017), their placement along the sides of hills does not support this view. Similarly, we are not sure why speckle (S, Fig. 2.4) texture patterns are found over steep mountains, but the lack of high-resolution training datasets likely leads the model to perform worse over these high-gradient areas.

Another issue is that DeepBedMap will often pick up details from the high-resolution ice surface elevation model (Howat et al., 2019) input dataset, which may not be representative of the true bed topography. For example, the ridges (R, Fig. 2.4) found along fast-flowing ice streams and glaciers are likely to be the imprints of crevasses or flow stripes (Glasser & Gudmundsson, 2012) observable from the surface. An alternative explanation is that the ridges, especially the honeycomb-shaped ones, are rhombohedral moraine deposits formed by soft sediment squeezed up into basal crevasses that are sometimes found at stagnant surging glaciers (Dowdeswell, Canals, et al., 2016; Dowdeswell, Solheim, et al., 2016; Solheim & Pfirman, 1985). We favour the first interpretation as the positions of these bed features coincide with the surface features and also because these ridges are more likely to be eroded away in these fast-flowing ice stream areas.

The hummocky wave-like (W) patterns we observe over the relatively flat and slower-flowing areas are likely to result from surface megadune structures (Scambos, 2014). Alternatively, they may be ribbed or Rogen moraine features that are formed in an orientation transverse to the ice flow direction (Hättestrand, 1997; Hättestrand & Kleman, 1999). While any one of these two explanations may be valid in different regions of Antarctica, we lean towards the conservative interpretation that these features are the result of the DeepBedMap model overfitting to the ice surface elevation data.

2.5.2 Roughness

In Sect. 2.4.2, we quantitatively show that a well-trained DeepBedMap neural network model can produce high roughness values more comparable to the ground truth than those of BedMachine Antarctica. While the mass conservation technique used by BedMachine Antarctica (Morlighem et al., 2019) improves upon ordinary interpolation techniques such as bicubic interpolation and kriging, its results are still inherently smooth by nature. The ground-truth grids show that rough areas do exist on a fine scale, and so the high-resolution models we produce should reflect that.

DeepBedMap_DEM manages to capture much of the rough topography found in the Operation IceBridge ground-truth data, especially near the coast (see Fig. 2.6a, from -1550 to -1500 km on the x scale) where the terrain tends to be rougher.

Along the retrograde slope (see Fig. 2.6a, from -1500 to -1450 km on the x scale), several of the fine-scale (< 10 km) bumps and troughs in DeepBedMap_DEM can be seen to correlate well in position with the ground truth. In contrast, the cubically interpolated BedMachine Antarctica product lacks such fine-scale (< 10 km) bumps and troughs, appearing as a relatively smooth terrain over much of the transect. Previous studies that estimated basal shear stress over Thwaites Glacier have found a band of strong bed extending about 80–100 km from the grounding line, with pockets of weak bed interspersed between bands of strong bed further upstream (Joughin et al., 2009; Sergienko & Hindmarsh, 2013), a pattern that is broadly consistent with the DeepBedMap_DEM roughness results (see Fig. 2.5b).

In general, DeepBedMap_DEM produces a topography that is rougher, with SD values more in line with those observed in the ground truth (see Fig. 2.6b). The roughness values for BedMachine Antarctica are consistently lower throughout the transect, a consequence of the mass conservation technique using regularization parameters that yield smooth results. We note that the DeepBedMap_DEM does appear rougher than the ground truth in certain areas. It is possible to tweak the training regime to incorporate roughness (or any statistical measure) into the loss function (see Appendix A) to yield the desired surface, and this will be explored in future work (see Sect. 2.5.4). Recent studies have stressed the importance of form drag (basal drag due to bed topography) over skin drag (or basal friction) on the basal traction of Pine Island Glacier (Bingham et al., 2017; Kyrke-Smith et al., 2018), and the DeepBedMap super-resolution work here shows strong potential in meeting that demand as a high-resolution bed topography dataset for ice sheet modelling studies.

In terms of bed roughness anisotropy, DeepBedMap is able to capture aspects of it from the ground-truth grids by combining (1) ice flow direction via the ice velocity grid's x and y components (Mouginot et al., 2019b), (2) ice surface aspect via the ice surface elevation grid (Howat et al., 2019), and (3) the low-resolution bed elevation input (Fretwell et al., 2013). There are therefore inherent assumptions that the topography of the current bed is associated with the current ice flow direction, surface aspect and existing low-resolution BEDMAP2 anisotropy. Provided that the direction of this surface velocity and aspect is the same as bed roughness anisotropy, as demonstrated in Holschuh et al. (2020), the neural network will be able to recognize it and perform accordingly. However, if the ice flow direction and surface aspect is not associated with bed anisotropy, then this assumption will be violated and the model will not perform well.

2.5.3 Limitations

The DeepBedMap model is trained only on a small fraction of the area of Antarctica, at less than 0.1% of the grounded-ice regions (excluding ice shelves and islands). This is because the pixel-based convolutional neural network cannot be trained on sparse survey point measurements, nor is it able to constrain itself with track-based radar data. As the along-track resolution of radar bed picks are much smaller than 250 m pixels, it is also not easy to preserve roughness from radar unless smaller pixels are used. The topography generated by the model is sensitive to the accuracy of its data inputs (see Tables 2.1 and 2.2), and though this is a problem faced by other inverse methods, neural network models like the one presented can be particularly biased towards the training dataset. Specifically, the DeepBedMap

model focuses on resolving short-wavelength features important for sub-kilometre roughness, compared to BedMachine Antarctica (Morlighem et al., 2019) which recovers large-scale features like ridges and valleys well.

An inherent assumption in this methodology is that the training datasets have sampled the variable bed lithology of Antarctica (Cox et al., 2018) sufficiently. This is unlikely to be true, introducing uncertainty into the result as different lithologies may cause the same macroscale bed landscapes to result in a range of surface features. In particular, the experimental model’s topography is likely skewed towards the distribution of the training regions that tend to reside in coastal regions, especially over ice streams in West Antarctica (see Fig. 2.2). While bed lithology could be used as an input to inform the DeepBedMap model’s prediction, it is challenging to find a suitable geological map (or geopotential proxy; see e.g. Aitken et al., 2014; Cox et al., 2018) for the entire Antarctic continent that has a sufficiently high spatial resolution. Ideally, the lithological map (categorical or qualitative) would first be converted to a hardness map with an appropriate erosion law and history incorporated (quantitative). This is because it is easier to train generative adversarial networks on quantitative data (e.g. hardness as a scale from 0 to 10) than on categorical data variables (e.g. sedimentary, igneous or metamorphic rocks); the latter would require a more elaborate model architecture and loss function design.

2.5.4 Future directions

The way forward for DeepBedMap is to combine quality datasets gathered by radioglaciology and remote sensing specialists, with new advancements made by the ice sheet modelling and machine learning community. While care has been taken to source the best possible datasets (see Tables 2.1 and 2.2), we note that there are still areas where more data are needed. Radio-echo sounding is the best tool available to fill in the data gap, as it provides not only the high-resolution datasets needed for training but also the background coarse-resolution BEDMAP dataset. Besides targeting radio-echo-sounding acquisitions over a diverse range of bed and flow types, swath reprocessing of old datasets that have that capability (Holschuh et al., 2020) may be another useful addition to the training set. The super-resolution DeepBedMap technique can also be applied on bed elevation inputs newer than BEDMAP2 (Fretwell et al., 2013), such as the 1000 m resolution DEM over the Weddell Sea (Jeofry et al., 2017), the 500 m resolution BedMachine Antarctica dataset (Morlighem, 2019) or the upcoming BEDMAP3.

A way to increase the number of high-resolution ground-truth training data further is to look at formerly glaciated beds. There are a wealth of data around the margins of Antarctica in the form of swath bathymetry data and also on land in areas like the former Laurentide ice sheet. The current model architecture does not support using solely “elevation” as an input, because it also requires ice elevation, ice surface velocity and snow accumulation data. In order to support using these paleobeds as training data, one could do one of the following:

1. Have a paleo-ice-sheet model that provides these ice surface observation parameters. However, continent-scale ice sheet models quite often produce only kilometre-scale outputs, and there are inherent uncertainties with past ice sheet reconstructions that may bias the resulting trained neural network model.
2. Modularize the neural network model to support different sets of training data.

One main branch would be trained like a single-image super-resolution problem (W. Yang et al., 2019), where we try to map a low-resolution BEDMAP2 tile to a high-resolution ground-truth image (be it from a contemporary bed, a paleobed or offshore bathymetry). The optional conditional branches would then act to support and improve on the result of this naive super-resolution method. This design is more complicated to set up and train, but it can increase the available training data by at least an order of magnitude and lead to better results.

From a satellite remote sensing perspective, it is important to continue the work on increasing spatial coverage and measurement precision. Some of the conditional datasets used such as REMA (Howat et al., 2019) and MEaSUREs Ice Velocity (Mouginot et al., 2019b) contain data gaps which introduce artefacts in the DeepBedMap_DEM, and those holes need to be patched up for proper continent-wide prediction. A surface mass balance dataset with sub-kilometre spatial resolution will also prove useful in replacing the snow accumulation dataset (Arthern et al., 2006) used in this work. As the DeepBedMap model relies on data from multiple sources collected over different epochs, it has no proper sense of time. Ice elevation change captured using satellite altimeters such as from CryoSat-2 (Helm et al., 2014), ICESat-2 (Markus et al., 2017) or the upcoming CRISTAL (Kern et al., 2020) could be added as an additional input to better account for temporal factors.

The DeepBedMap model’s modular design (see Sect. 2.3.2) means the different modules (see Fig. 2.1) can be improved on and adapted for future-use cases. The generator model architecture’s input module can be modified to handle new datasets such as the ones suggested above or redesigned to extract a greater amount of information for better performance. Similarly, the core and upsampling modules which are based on ESRGAN (X. Wang et al., 2019) can be replaced with newer, better architectures as the need arises. The discriminator model which is currently one designed for standard computer vision tasks can also be modified to incorporate glaciology-specific criteria. For example, the generated bed elevation image could be scrutinized by the discriminator model for valid properties such as topographic features that are aligned with the ice flow direction. The redesigned neural network model can be retrained from scratch or fine-tuned using the trained weights from DeepBedMap to further improve the predictive performance. Taken together, these advances will lead to an even more accurate and higher-resolution bed elevation model.

2.6 Conclusions

The DeepBedMap convolutional neural network method presents a data-driven approach to resolve the bed topography of Antarctica using existing data. It is an improvement beyond simple interpolation techniques, generating high-spatial-resolution (250 m) topography that preserves detail in bed roughness and is adaptable for catchment- to continent-scale studies on ice sheets. Unlike other inverse methods that rely on some explicit parameterization of ice flow physics, the model uses deep learning to find suitable neural network parameters via an iterative error minimization approach. This makes the resulting model particularly sensitive to the training dataset, emphasizing the value of densely spaced bed elevation datasets and the need for such sampling over a more diverse range of Antarctic substrate types.

The use of graphical processing units (GPUs) for training and inference allows the neural network method to scale easily, and the addition of more training datasets will allow it to perform better.

The work here is intended not to discourage the usage of other inverse modelling or spatial statistical techniques but to introduce an alternative methodology, with an outlook towards combining each methodology's strengths. Once properly trained, the DeepBedMap model runs quickly (about 3 min for the whole Antarctic continent) and produces realistic rough topography. Combining the DeepBedMap model with more physically based mass conservation inverse approaches (e.g. Morlighem et al., 2019) will likely result in more efficient ways of generating accurate bed elevation maps of Antarctica. One side product resulting from this work is a test-driven development framework that can be used to measure and compare the performance of upcoming bed terrain models. The radioglaciology community has already begun to compile a new comprehensive bed elevation and ice thickness dataset for Antarctica, and there have been discussions on combining various terrain interpolation techniques in an ensemble to collaboratively create the new BEDMAP3.

2.7 Code and data availability

Python code for data preparation, neural network model training and visualization of model outputs is freely available at <https://github.com/weiji14/deepbedmap> (last access: 9 August 2020) and at <https://doi.org/10.5281/zenodo.3752613> (Leong & Horgan, 2020a). Neural network model training experiment runs are also recorded at <https://www.comet.ml/weiji14/deepbedmap> (last access: 9 August 2020).

The DeepBedMap_DEM is available from Zenodo at <https://doi.org/10.5281/zenodo.3752613> (Leong & Horgan, 2020a). The Pine Island Glacier dataset (Bingham et al., 2017) is available on request from Robert Bingham. The Carlson Inlet dataset (King, 2011) is available on request from Edward King. Bed elevation datasets from Wilkes Subglacial Basin (Ferraccioli et al., 2018) and Rutford Ice Stream (King et al., 2016) are available from the British Antarctic Survey's Polar Data Centre (<https://ramadda.data.bas.ac.uk>, last access: 14 January 2020). Other Antarctic bed elevation datasets are available from the Center for Remote Sensing of Ice Sheets (<https://data.cresis.ku.edu/data/rds>, last access: 15 August 2019) or from the National Snow and Ice Data Center (<https://nsidc.org/data/IRMCR2/> versions/1, last access: 15 August 2019). BEDMAP2 (Fretwell et al., 2013) and REMA (Howat et al., 2018) are available from the Polar Geospatial Center (<http://data.pgc.umn.edu>, last access: 30 August 2019). MEaSUREs Ice Velocity data (Mouginot et al., 2019b) are available from NSIDC (<https://nsidc.org/data/nsidc-0754/> versions/1, last access: 31 August 2019). Antarctic snow accumulation data (Arthern et al., 2006) are available from the British Antarctic Survey (https://secure.antarctica.ac.uk/data/bedmap2/resources/Arthern_accumulation, last access: 17 June 2019).

2.8 Acknowledgements

We are grateful to Robert Bingham and Edward King for the Pine Island Glacier and Carlson Inlet data and to all the other researchers in the British Antarctic Survey and Operation IceBridge team for providing free access to the high-resolution bed elevation datasets around Antarctica. A special thanks to Ruzica Dadic for her help

in reviewing draft versions of this paper. This research was funded by the Royal Society of New Zealand’s Rutherford Discovery Fellowship (contract RDF-VUW1602), with additional support from the Erasmus+ programme and International Glaciological Society early-career travel award for presenting earlier versions of this work at the 2019 EGU General Assembly and IGS Symposium on Five Decades of Radioglaciology.

Chapter 2, in full, is a reprint of material as it appears in *The Cryosphere*: Leong, W. J., & Horgan, H. J. (2020). DeepBedMap: A deep neural network for resolving the bed topography of Antarctica. *The Cryosphere*, 14(11), 3687–3705. <https://doi.org/10.5194/tc-14-3687-2020>. The paper was edited by Olivier Gagliardini and reviewed by Martin Siegert and one anonymous referee.

Chapter 3

The role of subglacial topography on Antarctic ice flow

Abstract

To examine the influence of bed topography on ice motion, we conduct an inversion experiment using two beds with different spatial resolutions - the 250 m resolution DeepBedMap_DEM and the 500 m resolution BedMachine Antarctica. At the bed of a glacier, form drag and skin drag resists the driving stress of the overriding ice. We examine how an increase in form drag due to higher resolution topography affects the remaining skin drag component which is controlled by subglacial hydrology and bed material properties. An iterative least-squares control method basal inversion is performed using the Ice-sheet and Sea-level System Model (ISSM) with L1L2 stress balance equations and a Schoof-type Coulomb-limited sliding law. Comparison of inverted fields between DeepBedMap_DEM and BedMachine Antarctica do not appear to be significantly different. Basal drag and slipperiness fields are slightly higher, while effective pressure is generally lower when using the higher-resolution DeepBedMap_DEM, due to a higher bed elevation model and thinner ice inducing less overburden pressure. Previous inversion studies using a Weertman-style sliding relation over Pine Island Glacier indicated that high resolution bed topography (i.e. more form drag) reduced basal drag (i.e. less skin drag), a conclusion that is not supported in this work as no noticeable decrease in basal drag (i.e. skin drag) was observed when higher resolution topography (i.e. more form drag) was used. These findings warrant more investigation into the dependence of ice sheet modelling on higher spatial resolution bed topographies (≤ 100 m) which increases form drag, and time-dependent subglacial hydrology which influences skin drag, over more diverse subglacial settings in West Antarctica.

3.1 Introduction

The bed topography of Antarctica is a critical parameter in ice sheet modelling studies as it affects basal slip - the combined motion of ice from sliding and bed deformation (Cuffey & Paterson, 2010, p.223). Understanding the slip relation remains one of the biggest uncertainties in our determination of the Antarctic ice sheet's contribution to sea level rise (e.g. Bulthuis et al., 2019; Ritz et al., 2015). The basal conditions of an ice sheet vary spatially, and are often determined via

inverse methods. Inverse methods allow us to use ice surface observations coupled with ice physics to solve for critical basal parameters needed for ice sheet modelling (e.g. Joughin et al., 2009; MacAyeal, 1992; Morlighem et al., 2013), and also to resolve bed topography (e.g. Leong & Horgan, 2020b; Morlighem et al., 2019). These indirect empirical methods are used because sampling subglacial sediments under the Antarctic ice sheet is logistically challenging (e.g. Siegert, Makinson, et al., 2014; Tulaczyk et al., 2014), though having direct access to sediments would allow us to use physically based methods of quantifying basal slip (e.g. Zoet & Iverson, 2020).

This chapter explores the interplay between two components of frictional drag at the ice-bed interface - form drag and skin drag (Bingham et al., 2017; Kyrke-Smith et al., 2018; Minchew & Joughin, 2020; Schoof, 2002). Form drag occurs from long-wavelength bed topography opposing ice motion (Schoof, 2002; Weertman, 1957), while skin drag arises in relation to lubricating water and bed material properties (Iverson & Zoet, 2015). To study this, we look at how a high resolution (250 m) rougher bed (Leong & Horgan, 2020a) compares with a medium resolution (500 m) smoother bed (Morlighem, 2020). The spatially varying basal drag of the bed can be worked out by using bed topography to calculate form drag (Schoof, 2002), and then taking the remainder balance as skin drag which is determined by bed material properties and subglacial hydrology (Kyrke-Smith et al., 2018). In the following, we review two key parameters which ice sheet models are sensitive to - multi-scale bed topography features and sliding law relations.

3.1.1 Bed Topography

Durand et al. (2011) performed a sensitivity analysis on different spatial resolution beds using a 2-D flowline model and suggested that a spatial resolution of at least 1 km was needed to accurately model coastal outlet glaciers. This was followed by the creation of BEDMAP2 (Fretwell et al., 2013) - a 1 km resolution Antarctic bed elevation model resampled from a 5 km grid, which became the de facto standard for ice sheet models (see e.g. Seroussi et al., 2019). However, there have been issues reported in relation to BEDMAP2's ice thickness at the former grounding line of Pine Island Glacier that did not respect mass conservation (Rignot et al., 2014). High resolution bed elevations are especially needed close to grounding zones (e.g. Cornford et al., 2016; Schoof, 2007), and there is a need for high resolution (≤ 500 m) bed elevation models that preserve topographic details, so that form drag - resistance to ice flow due to bed topography - is correctly accounted for (Bingham et al., 2017; Kyrke-Smith et al., 2018). The limitations of BEDMAP2 motivated the creation of higher resolution (≤ 500 m) bed DEMs with two important attributes - large-scale topography that is consistent with mass conservation requirements (e.g. Morlighem et al., 2011), and preservation of fine-scale roughness details (e.g. Goff et al., 2014; Graham et al., 2017), both of which are needed to fully capture ice-sheet dynamics.

Long-wavelength details captured by mass conservation

Ice sheet models include the physical laws of mass conservation, and this can be used to invert ice surface observations into bed elevation (e.g. Morlighem et al., 2011). Using an ensemble of 2-D shelfy stream approximation (SSA; MacAyeal, 1989) models, Schlegel et al. (2018) performed a comparison of bedrock topography over the Antarctic ice sheet, and their informed bound (using regionally based boundary

conditions) experiments showed that using an improved BEDMAP2 mass conserving grid (cf. Rignot et al., 2014) produced 0.3292 ± 0.1019 m SLE, while the older BEDMAP (Lythe & Vaughan, 2001) grid produced a 0.1845 ± 0.08834 m SLE over a 100 yr period. This represents a mean increase of 0.14 m SLE from the improved resolution BEDMAP2 mass conserving grid, but also an 18% increase in the SLE uncertainty which suggests a wider range of grounding line retreat scenarios with implications for ice sheet stability. On a catchment scale, Nias et al. (2018) produced a mass-conserving bed topography over Pine Island Glacier and found that modelled sea level contributions over a 50 yr period was consistently higher using the mass-conserving bed ($0.08\text{--}0.10 \text{ mm yr}^{-1}$ SLE) than with BEDMAP2 ($0.04\text{--}0.07 \text{ mm yr}^{-1}$ SLE) irrespective of the sliding law used. Since then, this mass conservation technique has been applied to other key outlet glaciers and ice streams in BedMachine Antarctica (Morlighem, 2020), identifying new areas vulnerable to Marine Ice Sheet Instability such as at Ninnis Glacier in George V Land and Denman Glacier in East Antarctica which both rest on retrograde slopes (Morlighem et al., 2019). This medium resolution (500 m) mass conserving BedMachine Antarctica grid (version 2, Morlighem, 2020) will be used in our basal inversion experiment.

Short-wavelength details from spatial statistics

Using an ensemble of L1L2 (Hindmarsh, 2004; Schoof & Hindmarsh, 2010) ice sheet models, Sun et al. (2014) showed that the phase of low-frequency noise (> 10 km) was more important than the phase of high-frequency noise (< 1 km) of the same amplitude in their model projection runs. Still, the ice sheet model was sensitive to the amplitude of the short-wavelength/high-frequency noise even if the phase of that noise was not so important. Spatial statistical methods have since been used to retrieve this topographical noise along radio-echo sounding (RES) transects and apply it spatially to a larger regional extent. Over Thwaites Glacier, Goff et al. (2014) captured the different roughness statistics between highland and lowland parts, and applied these to the whole catchment using a conditional simulation method which allowed fine-scale roughness and channelized morphologies to be resolved better than ordinary kriging. Graham et al. (2017) generated a synthetic high-resolution (100 m) grid using a two-step approach, with the low-frequency component derived from BEDMAP2, and a high-frequency component derived from radar point data from the Investigating the Cryospheric Evolution of the Central Antarctic Plate (ICECAP) and BEDMAP compilation. Leong and Horgan (2019) used 2-D gridded RES ground-truth data with ice surface observations of elevation, velocity and snow accumulation to train a super-resolution deep neural network model, using it to produce a 250 m resolution grid of the Antarctic ice sheet. This super-resolution (250 m) DeepBedMap_DEM grid (version 1.1, Leong & Horgan, 2020a) will be used in our basal inversion experiment.

3.1.2 Basal drag

Form drag arises due to large-scale bed topography which opposes the motion of ice as it flows and deforms around obstacles on a rigid bed (Schoof, 2002; Weertman, 1957). Skin drag occurs in relation to bed material properties and in the presence of water that acts to lubricate the ice-bed interface and allow subglacial till to deform more easily (Iverson & Zoet, 2015). The physical mechanisms of these two processes

may differ, but the mathematical formulation and parameterizations for both are similar (Fig. 1.3, Minchew & Joughin, 2020).

3.1.2.1 Physical basis of basal slip

A basal slip law that relates basal drag or basal shear stress τ_b with effective normal stress (pressure) N and basal slip velocity u_b is given by Zoet and Iverson (2020, eq.1):

$$\tau_b = \min[N \tan(\phi), (Cu_b)^{1/m}] \quad (3.1)$$

where ϕ is the friction angle of the basal till, such that $\tan(\phi)$ is the friction coefficient, m is a slip law exponent, and C is a constant dependent on a transitional velocity u_t and bed roughness, formulated as $C = \frac{(N \tan(\phi))^m}{u_t}$. The approximate continuous form of Equation (3.1) (Zoet & Iverson, 2020, eq.3) is as follows:

$$\tau_b = N \tan(\phi) \left(\frac{u_b}{u_b + u_t} \right)^{1/p} \quad (3.2)$$

where p is a slip exponent, experimentally determined to be ~ 5 (Zoet & Iverson, 2020).

At low basal slip speeds ($u_b \rightarrow 0$) typically found over rigid, dry beds, viscous Weertman-style behaviour ($(Cu_b)^{1/m}$ in Eq. 3.1, Weertman, 1957) dominates total drag τ_b . At high basal slip speeds ($u_b \rightarrow \infty$) found over water-saturated deforming beds, Coulomb-plastic behaviour ($N \tan(\phi)$ in Eq. 3.1, e.g. Joughin et al., 2019; Schoof, 2005) is more influential. The upper bound of τ_b is based on the shear strength of the till, as determined from ring-shear laboratory experiments (Zoet & Iverson, 2020). Past the transition speed u_t , basal drag τ_b becomes independent of basal slip velocity u_b (c.f. Stearns & van der Veen, 2018). The physical formulation of Equation (3.1) is similar to that of other Coulomb-based parametrizations (e.g. Joughin et al., 2019; V. C. Tsai et al., 2015), but while previous implementations fixed C to estimate u_t via inversion (*a posteriori*), Equation (3.1) is formulated on a physical basis with u_t derived independently (using clast size and till placement, see eq.2 in Zoet & Iverson, 2020) and then used to directly determine C (*a priori*).

3.1.2.2 Sliding laws - linear viscous to Coulomb-limited

It is not feasible to access subglacial till across a glaciated area to physically determine u_t using Equation (3.1), so parameterized basal slip relations are used in practice. Sensitivity analyses conducted in multiple ice sheet model comparison studies (e.g. Seroussi et al., 2019; Sun et al., 2020; Zhang et al., 2017) have explored the use of different basal slip relations or sliding laws (see Fig. 3.1), and the different tunable parameters that come with them. Gillet-Chaulet et al. (2016) used surface velocity observations from 1996 to 2010 over Pine Island Glacier and suggested that a non-linear Weertman stress exponent of $m \geq 5$ best matched observed flow accelerations, with the assumption that the basal slipperiness coefficient C remained constant over the period. In the Antarctic Buttressing Model Intercomparison Project (ABUMIP; Sun et al., 2020), the ice-shelf removal or ‘float-kick’ experiment (ABUK) noted how ice sheet models implementing linear Weertman/Coulomb friction laws tend to show lower ice loss (3.07 m SLE) than models which implemented pseudo-plastic (4.41 m SLE) or plastic (10.20 m SLE) sliding

laws. Ice sheet models implementing such non-linear/plastic sliding laws generally lead to faster grounding line retreat than those using viscous linear sliding laws over the Amundsen Sea Embayment area (e.g. Brondex et al., 2017; Bulthuis et al., 2019; Joughin et al., 2009; Ritz et al., 2015).

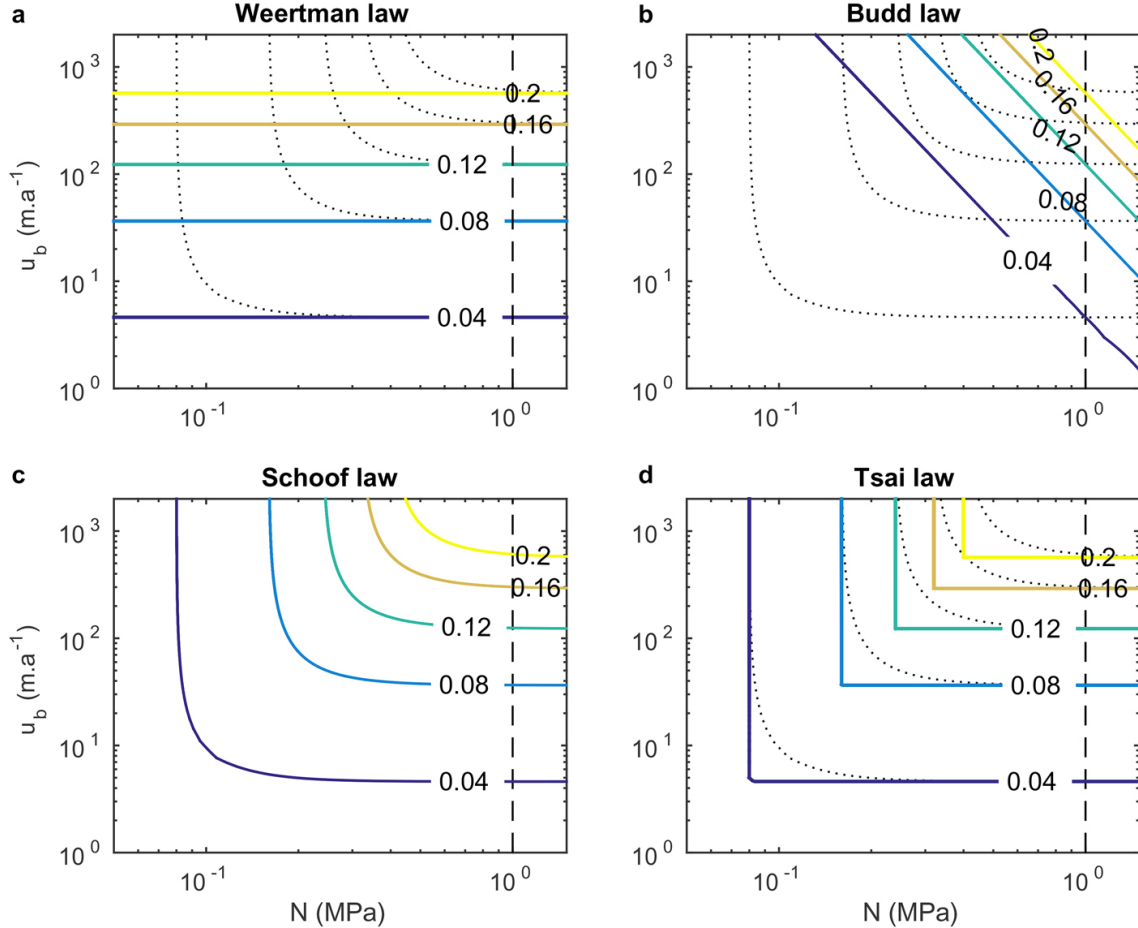


Figure 3.1: Comparison of linear (Weertman, Budd) and non-linear, Coulomb limited (Schoof and Tsai) sliding laws. Basal velocity u_b is plotted on the vertical y-axis and effective pressure N is plotted on the horizontal x-axis. Coloured iso-lines represent basal drag (τ_b) values ranging from 0.04 MPa to 0.2 MPa. Figure is from Brondex et al. (2017).

Other intercomparisons have judged the ability of different sliding laws to properly model grounding line dynamics, with overarching support for effective pressure (N) dependent sliding laws such as Budd-type (Budd et al., 1979), Tsai-type (V. C. Tsai et al., 2015) or Schoof-type (Schoof, 2005) formulations instead of a classical Weertman-type (Weertman, 1957) relation (see Fig. 3.1, Brondex et al., 2017; Brondex et al., 2019). In particular, Joughin et al. (2019) noted how the effects of cavitation on sliding (see Schoof, 2005) appear important at Pine Island Glacier, recommending a regularized Coulomb sliding law with $m = 3$ and velocity threshold $u_o = 300 \text{ m yr}^{-1}$ to reliably reproduce glacier behaviour in a manner applicable to both weak till and hard bedrock areas. Coulomb-limited sliding relations are generally favoured, such as a Schoof-type law for its ability to transition continuously between Weertman and Coulomb sliding regimes in different settings (Brondex et al., 2017; Brondex et al., 2019; Cornford et al., 2020; Minchew & Joughin, 2020; Zoet & Iverson, 2020). Thus, we choose to use the Schoof sliding law (adapted from

Schoof, 2005, eq. 6.2), presented below in a form similar to that of Equation (3.2):

$$\tau_b = NC \left(\frac{\Lambda}{\Lambda + \Lambda_0} \right)^{1/m}, \Lambda = \frac{u_b}{N^m} \quad (3.3)$$

where τ_b is basal drag, N is effective pressure, C is the Schoof friction coefficient less than the maximum bed slope (c.f. $\tan(\phi)$ in Eq. (3.2)), u_b is basal velocity, Λ_0 is a maximum threshold that satisfies Iken's bound (c.f. u_t in Eq. (3.2)), and m is a power law exponent. Equation (3.3) will be reformulated as Equation (3.5) in the Methods section to follow the ISSM (Larour et al., 2012) Schoof sliding law implementation.

3.1.3 Previous work

Kyrke-Smith et al. (2018) ran a Full Stokes ice sheet model inversion experiment with a Weertman-style sliding law on two different beds - a high-resolution (50 m) bed topography from DELORES data (Bingham et al., 2017) and on a low-resolution (1000 m) BEDMAP2 (Fretwell et al., 2013) - to compare the balance of slipperiness (C) and basal drag (τ_b) estimates. They reported that spatial patterns of both slipperiness C and basal drag τ_b were similar across both high- and low-resolution experiments. However, the magnitude of the spatially averaged basal drag τ_b (i.e. skin drag) was consistently lower when using the high-resolution DELORES DEM than with the low-resolution BEDMAP2 owing to more form drag being accounted for. Over the iSTARt1 area for example, the high-resolution DELORES DEM had $\bar{\tau}_b = 6.8$ kPa, low-resolution BEDMAP2 had $\bar{\tau}_b = 9.6$ kPa, while the flat bed control experiment had $\bar{\tau}_b = 11.9$ kPa. The lower mean basal drag $\bar{\tau}_b$ was attributed to an increase in form drag introduced by the high-resolution DELORES DEM that induces more resistive stresses on ice. The skin drag component must therefore decrease, corresponding to a lower slipperiness C , in order for the modelled velocity to match the observed velocity in the inversion process. The implications of this are that both basal drag τ_b and slipperiness C may be overestimated for ice sheet models using parameterizations based on low-resolution bed topography models like BEDMAP2 (Kyrke-Smith et al., 2018). Here, we expand on the work of Kyrke-Smith et al. (2018) by running an L1L2 ice sheet model (ISSM; Larour et al., 2012) using a Coulomb-limited Schoof-type sliding law (Joughin et al., 2019; Schoof, 2005) over the larger spatial area of the main trunk of Pine Island Glacier (see Fig. 3.2).

3.2 Methods

3.2.1 Ice Sheet model set-up

3.2.1.1 Stress balance model

We use an L1L2 model (Hindmarsh, 2004; Schoof & Hindmarsh, 2010) implemented in the Ice-sheet and Sea-level System Model (ISSM, v4.18; Larour et al., 2012). ISSM is a thermomechanical finite-element ice flow model that follows physical laws for the conservation of mass, momentum and energy, coupled with constitutive material laws and boundary conditions (Larour et al., 2012). Ice is treated as an viscous incompressible material (Cuffey & Paterson, 2010) with a non-linear ice effective viscosity μ following a Norton-Hoff rheology law (Glen's flow law, Glen, 1955):

$$\mu = \frac{B}{2\dot{\epsilon}_e^{(n-1)/n}} \quad (3.4)$$

where B is the temperature dependent ice hardness (rigidity), $\dot{\epsilon}_e$ is the effective strain rate tensor, n is Glen's flow law exponent.

3.2.1.2 Sliding law

Within ISSM, we applied a Schoof-type basal sliding law (Schoof, 2005):

$$\tau_b = -\frac{C|u_b|^{m-1}u_b}{\left(1 + \left(\frac{C}{C_{\max}N}\right)^{1/m} + |u_b|\right)^m} \quad (3.5)$$

where τ_b is basal drag, C is the Schoof friction coefficient (slipperiness), C_{\max} is a Coulomb friction upper bound parameter, u_b is basal ice velocity, N is effective pressure, and m is a positive power law exponent (note that m here is the reciprocal of m in other studies (e.g. V. C. Tsai et al., 2015), i.e. $m = 1/m_{\text{Tsai}} = 1/3$).

The friction factor C_{\max} imposes an upper limit on τ_b which must satisfy Iken's bound (Gagliardini et al., 2007; Iken, 1981):

$$\tau_b \leq N \tan \beta \quad (3.6)$$

where β is the maximum local up-slope angle between the bed and mean flow direction. Based on lab experiments (Iverson et al., 1998), C_{\max} is set to between $\tan 10^\circ = 0.17$ and $\tan 40^\circ = 0.84$, with lower values corresponding to clay-rich tills (Cuffey & Paterson, 2010, pp.266-267). The spatial distribution of C_{\max} varies across a glacier but no method yet exists to constrain it, so a uniform value of 0.4 is used instead (0.4 and 0.6 was used in Brondex et al., 2019). The magnitude of τ_b has an asymptotic behaviour, such that $\tau_b \sim Cu_b^m$ as N trends towards infinity corresponding to a Weertman-type sliding regime, and $\tau_b \sim C_{\max}N$ as N trends towards zero corresponding to a Coulomb-type sliding regime (Brondex et al., 2017).

The effective pressure (N) can be approximated using ice overburden pressure minus water pressure:

$$N = \rho_i g H - P_w \quad (3.7)$$

where ρ_i is ice density, g is gravitational acceleration, H is ice thickness and P_w is water pressure.

3.2.1.3 Boundary conditions

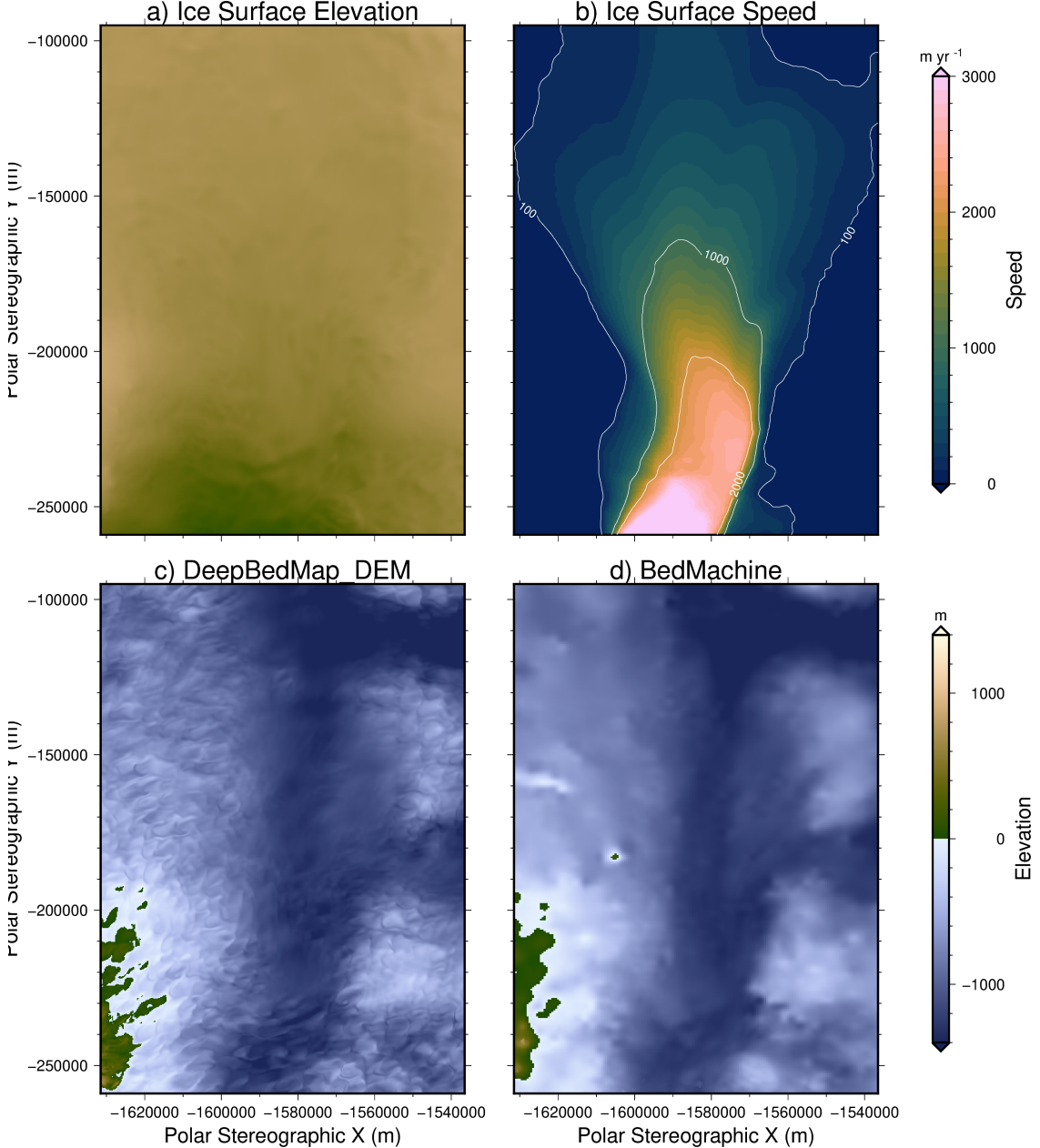


Figure 3.2: Topographies and speed over Pine Island Glacier study area. a) Ice surface elevation from Howat et al. (2019). b) Ice surface speed (contours in white) from Mouginot et al. (2019b). c) DeepBedMap_DEM bed elevation. d) BedMachine bed elevation. Plotted on an Antarctic Stereographic Projection with a standard latitude of 71°S (EPSG:3031).

The boundary conditions are kept equal across all experiments, aside from modifications to the bed topography (see Fig. 3.2). The model’s spatial domain is a triangulated static anisotropic adaptive mesh grid with 10 vertical layers, and a spatial resolution of 250–20 000 m (higher resolution over areas of high ice velocity), located over the main trunk of Pine Island Glacier. The same mesh is used for both experiments. A minimum ice thickness of 1 m is set to avoid numerical instabilities. A stress-free surface is applied at the ice-atmosphere interface $\boldsymbol{\sigma} \cdot \mathbf{n} = 0$ where $\boldsymbol{\sigma}$ is the Cauchy stress tensor and \mathbf{n} is the unit outward-pointing normal vector (Larour

et al., 2012, eq. 18). Surface mass balance, ice temperature and geothermal heat flux are from ALBMAPv1 (Le Brocq et al., 2010).

3.2.2 Inverting for basal drag τ_b

To determine the spatial distribution of basal drag (τ_b), we run an inversion using remotely sensed values of surface velocity u_s (Fig. 3.2b). This is accomplished using a least-squares approach involving a control method (MacAyeal, 1992, eq. 6) which avoids the errors in τ_b caused by using a direct algebraic inversion approach (e.g. MacAyeal, 1992, eq. 4, 5) which is more sensitive to un-physical interpolations of u_s . Following Morlighem et al. (2013, eq. 9), the objective function or cost function J used to minimize the difference in modelled and observed surface velocities is formulated as follows:

$$J(\mathbf{v}, \alpha) = J_{mis} + \gamma_1 J_1 + \gamma_t J_2 \quad (3.8)$$

where \mathbf{v} is ice surface velocity, α is the parameter being inverted (i.e. the friction coefficient $\ln(C)$), and γ_1, γ_t are non-dimensional weighting constants. The initial friction coefficient was set as $\alpha_0 = 10 \text{ (Pa yr/m)}^{1/2}$ for the model domain. We set $\gamma_1 = 100$ and $\gamma_t = 10^{-7}$ following Morlighem et al. (2013).

The first term J_{mis} is an L^2 misfit calculated as:

$$J_{mis} = \frac{1}{2} \int_{\Gamma_s} (v_x - v_x^{obs})^2 + (v_y - v_y^{obs})^2 d\Gamma_s \quad (3.9)$$

where v_x and v_y are modelled ice surface velocities (in the x and y directions), v_x^{obs} and v_y^{obs} are observed ice surface velocities from Mouginot et al. (2019a), and Γ_s is the ice surface domain.

The second term J_1 takes the squared natural logarithmic difference between u and u_{obs} :

$$J_1 = \frac{1}{2} \int_{\Gamma_s} \ln \left(\frac{\sqrt{u^2 + v^2} + \epsilon}{\sqrt{u_{obs}^2 + v_{obs}^2} + \epsilon} \right)^2 d\Gamma_s \quad (3.10)$$

where ϵ is a minimal velocity used to avoid division by zero. This J_1 term accounts for the order of magnitude difference in ice flow speed that ranges from $> 1000 \text{ m yr}^{-1}$ at ice streams to $< 1 \text{ m yr}^{-1}$ in the slow moving interior (Mouginot et al., 2019a).

The third term J_2 is a Tikhonov regularization term which applies a degree of smoothness to the inversion:

$$J_2 = \frac{1}{2} \int_{\Gamma_b} \nabla \alpha \cdot \nabla \alpha d\Gamma_b \quad (3.11)$$

where Γ_b is the ice bed domain, and recall that α is the parameter being inverted.

The inversion is computed by iteratively minimizing the total cost function J until a convergence stopping criterion is reached. The stopping criterion is set empirically as when the cost function output value reduces by < 0.1 between successive iterations. Further details of the inversion process can be found in Morlighem et al. (2013).

3.3 Results

We now present our results over Pine Island Glacier, comparing the medium spatial resolution (500 m) smooth bed (BedMachine v2; Morlighem, 2020) with a high spatial resolution (250 m) rough bed (DeepBedMap_DEM v1.1; Leong & Horgan, 2020a). In the following, we present the inverted spatial distributions of each bed's modelled velocity (u_b , Fig. 3.3) along with effective pressure (N , Fig. 3.4), slipperiness (C , Fig. 3.5), and basal drag (τ_b , Fig. 3.6) fields. For all the fields above, we also present a transect plot taken along the main trunk of Pine Island Glacier (Fig. 3.7) and across flow (Fig. 3.8).

Basal velocity (u_b)

In Fig. 3.3, velocity u_b is shown to increase from the upstream part of the glacier (A) to the downstream part of the glacier (B) near the grounding zone for both DeepBedMap and BedMachine. The mean velocity (\bar{u}_b) for DeepBedMap_DEM (614 m yr^{-1}) is slightly higher than that of BedMachine (552 m yr^{-1}), a difference of 62 m yr^{-1} . Spatially, the difference in velocity between the two beds appears to be greatest near the grounding zone around point B (see also Fig. 3.8b).

Effective Pressure (N)

In Fig. 3.4, effective pressure N is shown to decrease from the upstream part of the glacier (A) to the downstream part of the glacier (B) near the grounding zone for both DeepBedMap and BedMachine. The mean effective pressure (\bar{N}) for DeepBedMap_DEM ($1.3389 \times 10^7 \text{ Pa}$) is lower than that of BedMachine ($1.3807 \times 10^7 \text{ Pa}$), a difference of $4.1762 \times 10^5 \text{ Pa}$. The along-flow transect plot (see Fig. 3.7c) shows that DeepBedMap_DEM's effective pressure field over the grounding zone (near point B) is noisier than that of BedMachine.

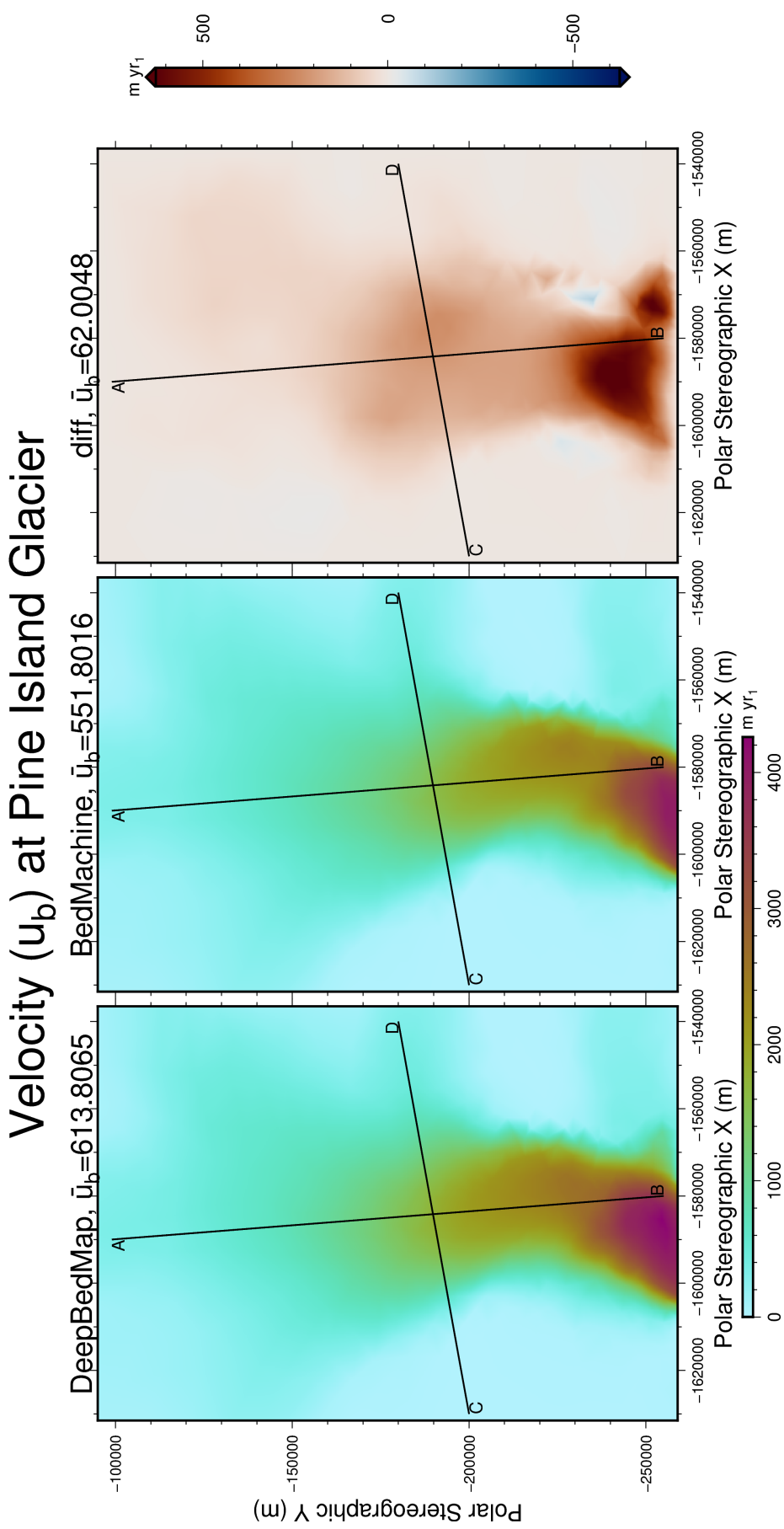


Figure 3.3: Comparison of basal velocity u_b over Pine Island Glacier for DeepBedMap and BedMachine. Ice flow direction is from top (point A) to bottom (point B). Transect lines cut along flow from upstream point A to downstream point B, and transversely from high elevation point C to low elevation point D. Plotted on an Antarctic Stereographic Projection with a standard latitude of 71°S (EPSG:3031).

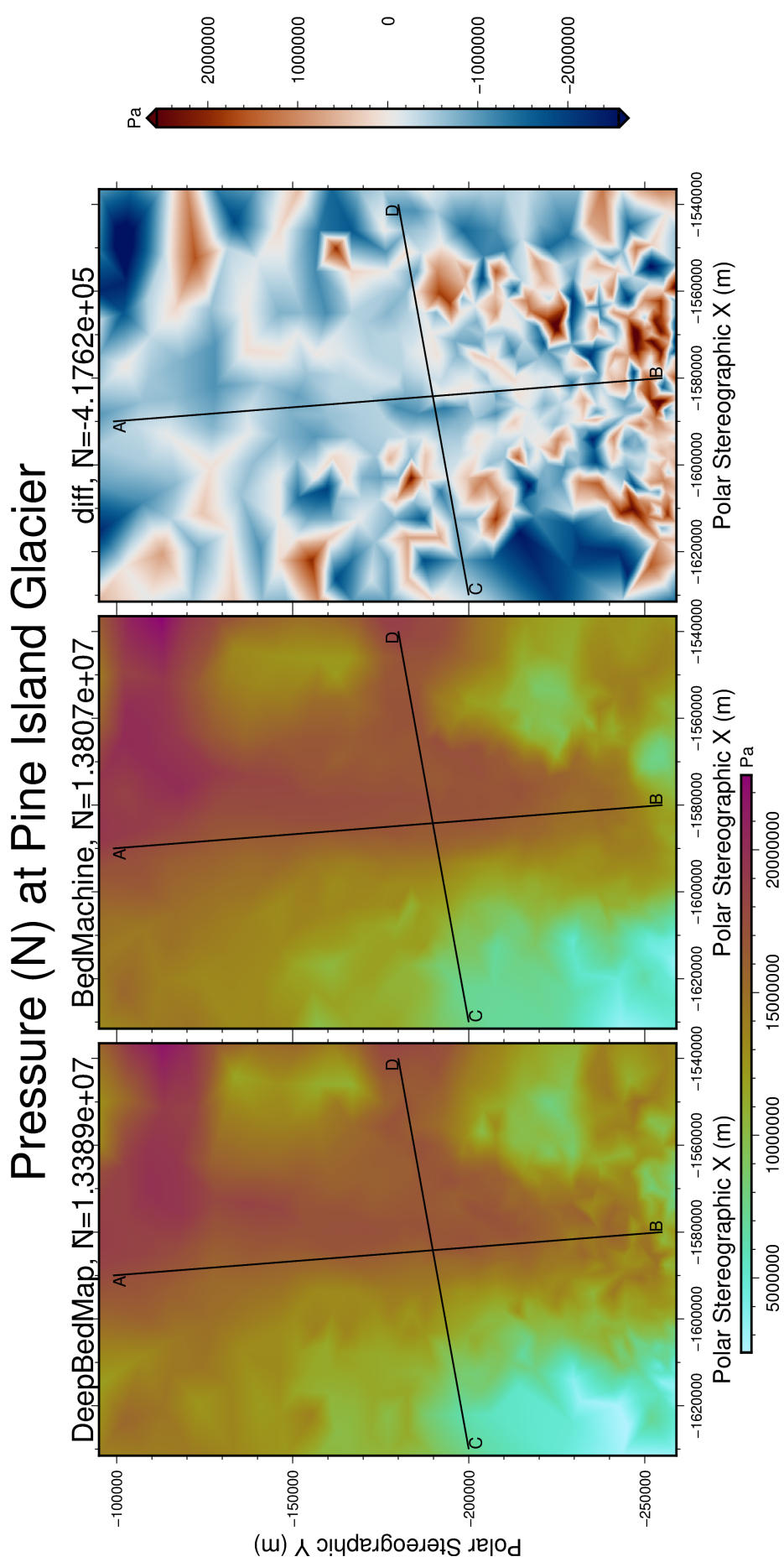


Figure 3.4: Comparison of effective pressure N over Pine Island Glacier for DeepBedMap and BedMachine. Ice flow direction is from top (point A) to bottom (point B). Transect lines cut along flow from upstream point A to downstream point B, and transversely from high elevation point C to low elevation point D. Plotted on an Antarctic Stereographic Projection with a standard latitude of 71°S (EPSG:3031).

Slipperiness (C)

In Fig. 3.5, slipperiness C (friction coefficient) is shown to increase from the upstream part of the glacier (A) to the downstream part of the glacier (B) near the grounding zone for both DeepBedMap and BedMachine. The mean slipperiness (\bar{C}) for DeepBedMap_DEM ($31.39 \text{ (Pa yr/m)}^{1/2}$) is slightly higher than that of BedMachine ($31.33 \text{ (Pa yr/m)}^{1/2}$), a difference of $0.06 \text{ (Pa yr/m)}^{1/2}$. The along-flow transect plot (see Fig. 3.7d) shows that DeepBedMap_DEM is missing one slipperiness peak at Y:-130000 compared to BedMachine Antarctica, owing to an offset of one ridge.

Basal drag (τ_b)

In Fig. 3.6, basal drag τ_b is shown to increase from the upstream part of the glacier (A) to the downstream part of the glacier (B) near the grounding zone for both DeepBedMap and BedMachine. The mean basal drag ($\bar{\tau}_b$) for DeepBedMap_DEM (203 Pa) is slightly higher than that of BedMachine (192 Pa), a difference of 11 Pa. Spatially, the difference in basal drag between the two beds appears more pronounced near the shear margins along the main trunk of the glacier (see across-track transect at Fig. 3.8e).

Transect along Pine Island Glacier trunk

Transect plots are shown along the main trunk of Pine Island Glacier from upstream point A to downstream point B (Fig. 3.7), and across flow from high elevation point C to low elevation point D (Fig. 3.8), with DeepBedMap_DEM (Leong & Horgan, 2020a) and BedMachine (Morlighem, 2020) both showing the same broad trends. Modelled basal velocity (u_b) for BedMachine appears to fit closer to the ground-truth velocities observed by remote sensing methods (Mouginot et al., 2019b) than for DeepBedMap_DEM (Fig. 3.7b, Fig. 3.8b). Effective pressure (N) tends to be lower for DeepBedMap_DEM than that of BedMachine across both transect lines (Fig. 3.7c, Fig. 3.8c), except for near the grounding line close to point B (Fig. 3.7c). Slipperiness (C , Fig. 3.7d, Fig. 3.8d) and basal drag (τ_b , Fig. 3.7e, Fig. 3.8e) fields are mostly comparable for both bed topographies.

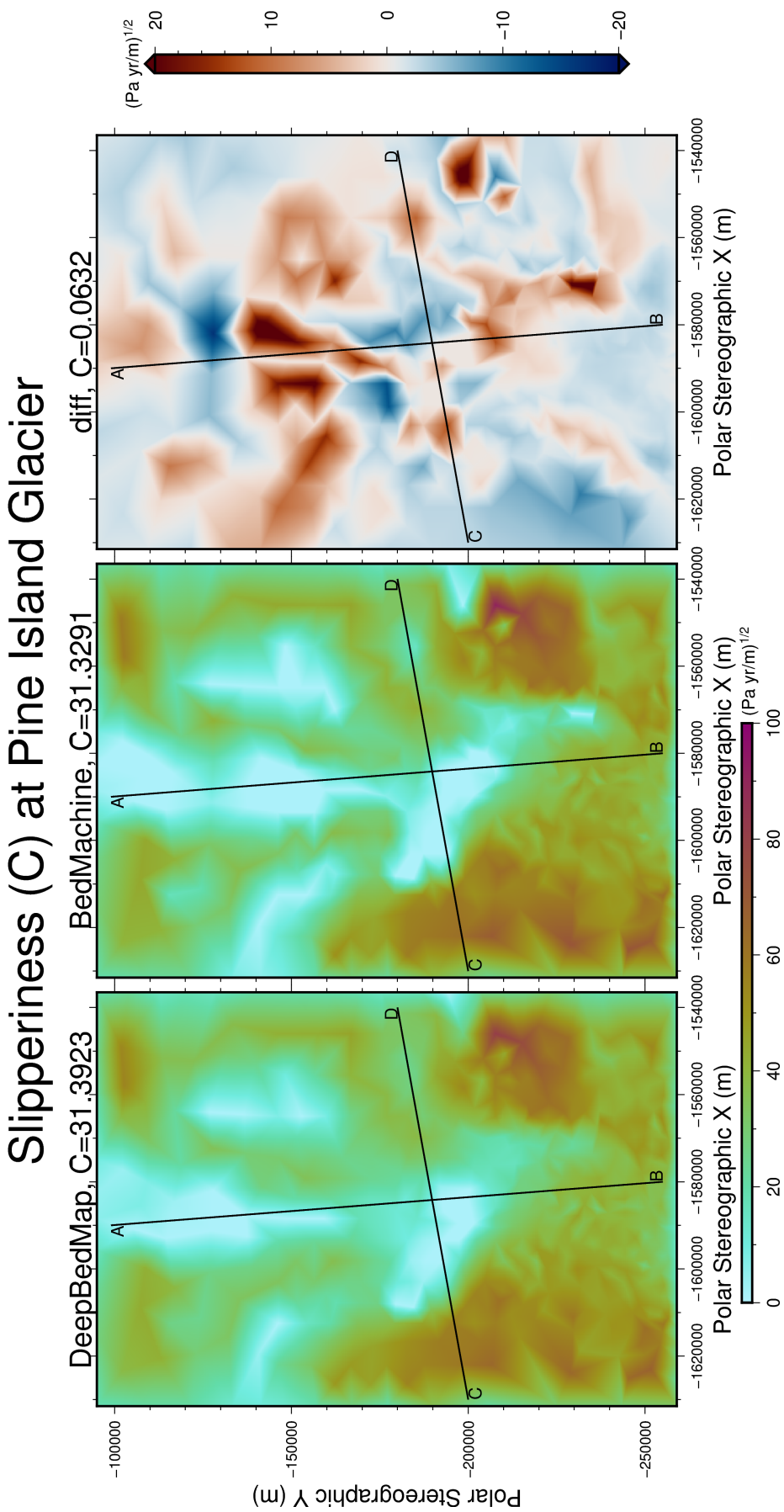


Figure 3.5: Comparison of slipperiness C (friction coefficient) over Pine Island Glacier for DeepBedMap and BedMachine. Ice flow direction is from top (point A) to bottom (point B). Transect lines cut along flow from upstream point A to downstream point B, and transversely from high elevation point C to low elevation point D. Plotted on an Antarctic Stereographic Projection with a standard latitude of 71°S (EPSG:3031).

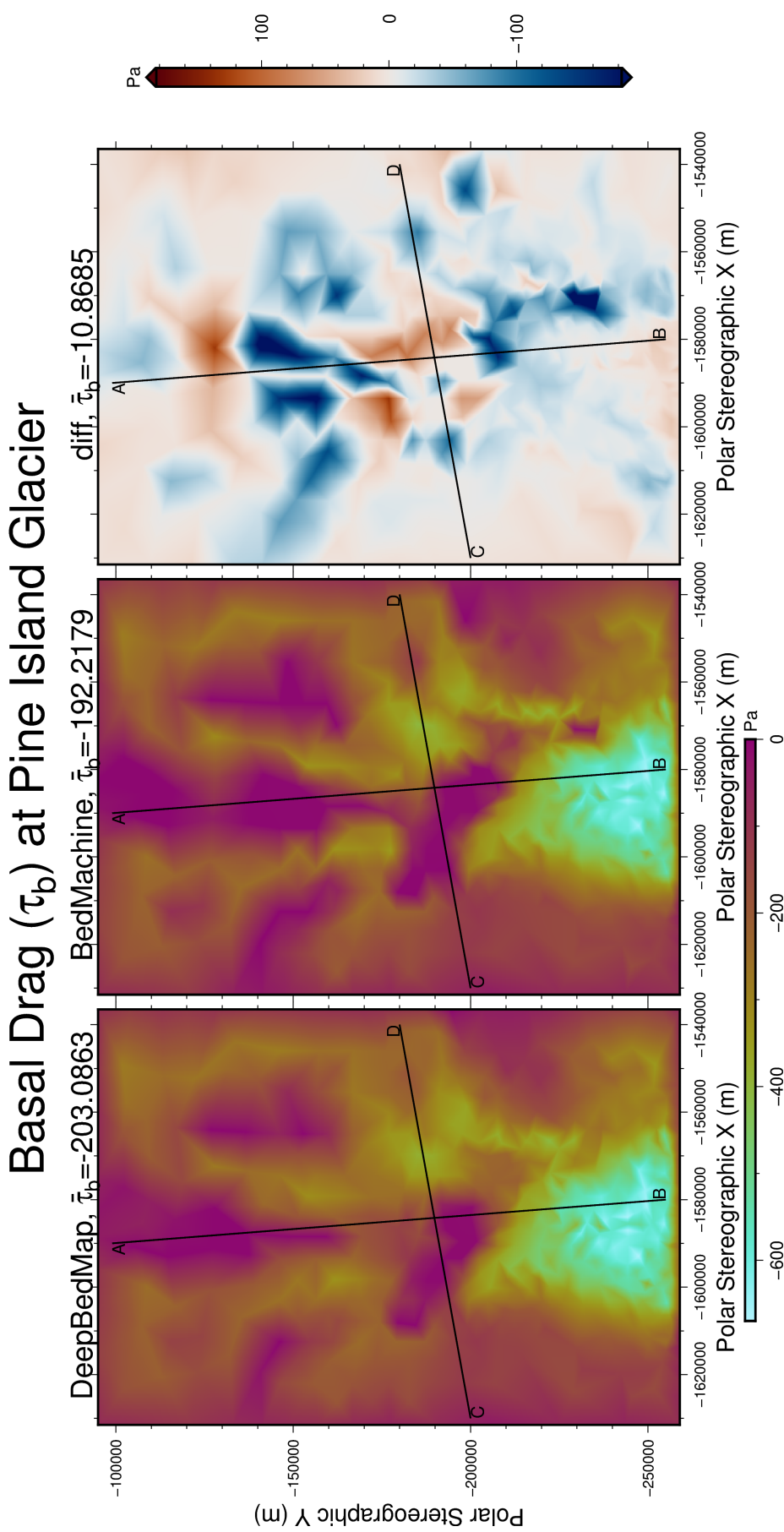


Figure 3.6: Comparison of basal drag τ_b over Pine Island Glacier for DeepBedMap and BedMachine. Ice flow direction is from top (point A) to bottom (point B). Transect lines cut along flow from upstream point A to downstream point B, and transversely from high elevation point C to low elevation point D. Plotted on an Antarctic Stereographic Projection with a standard latitude of 71°S (EPSG:3031).

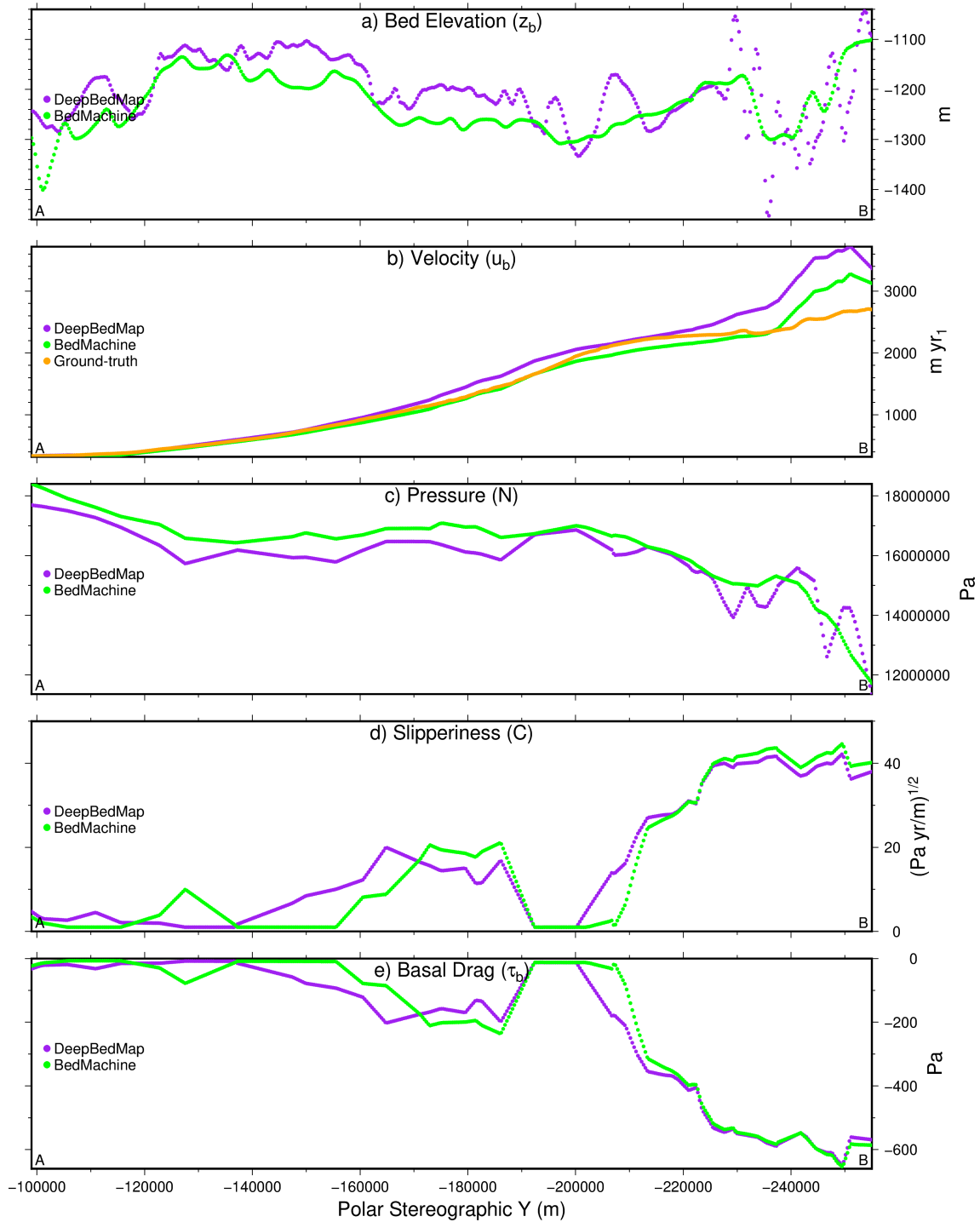


Figure 3.7: Transect plot along Pine Island Glacier trunk from upstream point A to downstream point B. Panels from top to bottom shows comparison of DeepBedMap DEM and BedMachine in terms of: a) Bed elevation (z_b), b) Ice surface velocity (u_s), c) Effective pressure (N), d) Slipperiness (C), e) Basal drag (τ_b).

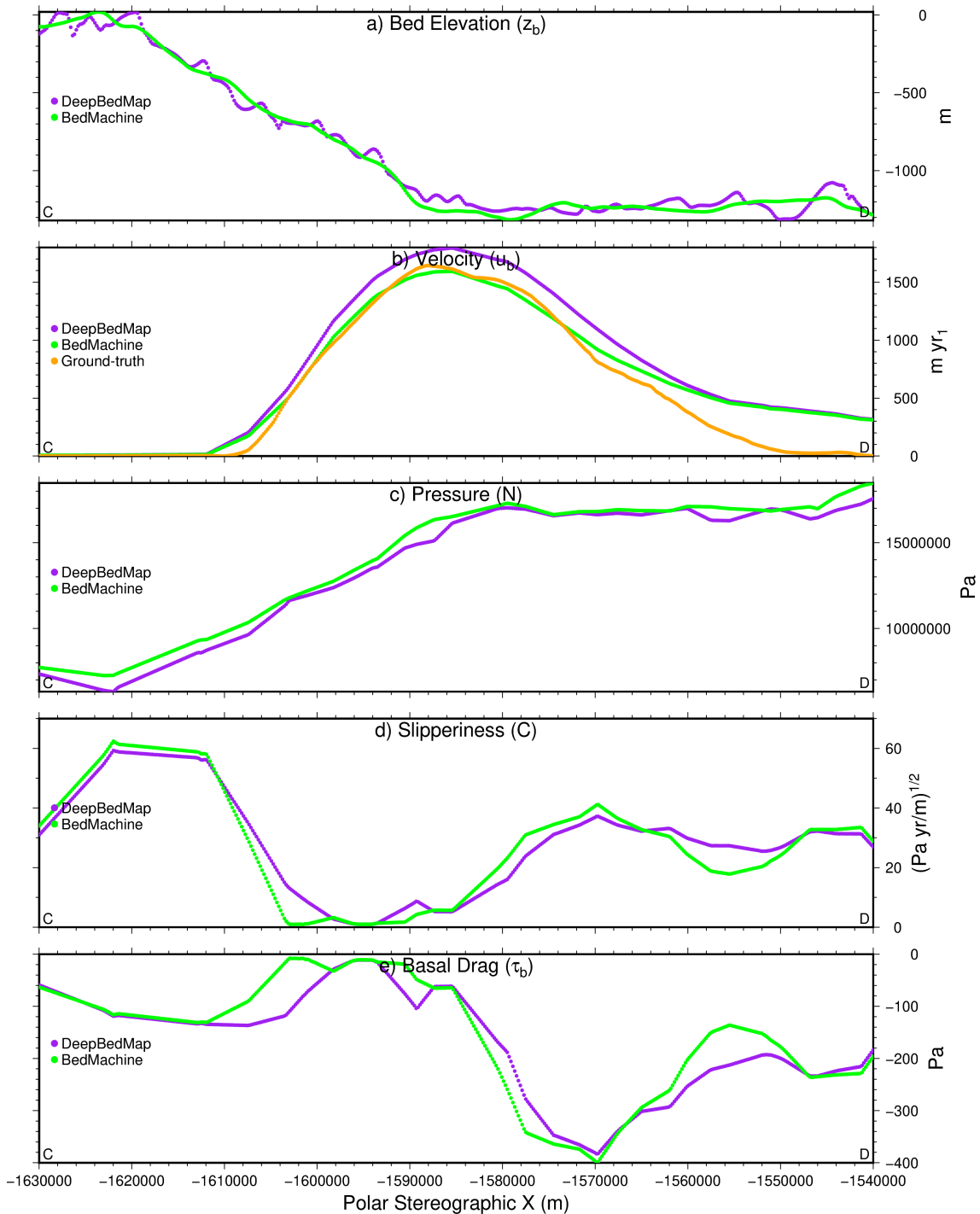


Figure 3.8: Transect plot cutting across Pine Island Glacier trunk from high elevation point C to low elevation point D. Panels from top to bottom shows comparison of DeepBedMap DEM and BedMachine in terms of: a) Bed elevation (z_b), b) Ice surface velocity (u_s), c) Effective pressure (N), d) Slipperiness (C), e) Basal drag (τ_b).

3.4 Discussion and Conclusion

The inverted basal drag ($\bar{\tau}_b$, Fig. 3.6) and slipperiness (\bar{C} , Fig. 3.5) over Pine Island Glacier is slightly higher for DeepBedMap_DEM than BedMachine Antarctica, while effective pressure (\bar{N} , Fig. 3.4) is generally lower (see Sec. 3.3). This mean difference in basal drag from using two different resolution beds is only 11 Pa and not very significant. In particular, this result is different to the findings of Kyrke-Smith et al. (2018) who showed a reduction in basal drag (less skin drag) and slipperiness C when using a higher resolution basal topography (more form drag). Several factors could account for this discrepancy.

Firstly, the 250 m difference in spatial resolution between DeepBedMap_DEM (Leong & Horgan, 2020a) and BedMachine Antarctica (Morlighem, 2020) is much smaller than the 950 m difference between DELORES DEM (Bingham et al., 2017) and BEDMAP2 (Fretwell et al., 2013). This smaller resolution difference may mean that the differences in basal drag (Fig. 3.6) and slipperiness (Fig. 3.5) are less apparent. It could also be a higher resolution (≤ 100 m) bed is needed (e.g. Graham et al., 2017) before the effects of form drag are significant enough to affect slipperiness C and hence basal drag τ_b . Alternatively, the effects may have been masked when bed elevation is interpolated to the same 250–20 000 m resolution mesh for both experiments (Sec. 3.2.1.3), and future studies should investigate such resolution dependence effects.

Secondly, the use of a Schoof-type friction law in our inversion (see 3.2) instead of a Weertman-type sliding law as in Kyrke-Smith et al. (2018) may mean that form drag from high resolution topography has less of an effect on basal drag τ_b (i.e. skin drag). Following the logic of Kyrke-Smith et al. (2018), a more accurate, high-resolution bed topography model (i.e. more form drag) should lower basal drag (τ_b , i.e. skin drag). Theoretically, this would shift parts of glaciers flowing at a rate close to the transitional velocity (u_t) from a skin drag regime to a transitional or form drag regime (see Fig. 1.3, Minchew & Joughin, 2020). This logic implies that subglacial water which influences skin drag (related to form drag τ_b) plays a less important role in ice dynamics when rougher, higher resolution bed elevation models (i.e. more form drag) are used, supporting studies where subglacial water inputs did not lead to significant speed ups in ice flow (e.g. B. E. Smith et al., 2017).

However, observed velocities over most of Pine Island Glacier are $> 100 \text{ m yr}^{-1}$ (see Fig. 3.2b) which suggests a predominantly Coulomb-type (skin drag based) flow regime rather than a Weertman-type (form drag based) flow regime (see Fig. 1.3, Minchew & Joughin, 2020). The decrease in basal drag τ_b (i.e. less skin drag) from using a higher resolution topography (i.e. more form drag) observed by Kyrke-Smith et al. (2018) may be an artifact of using an unbounded Weertman-type sliding relation, as our experiments using a Schoof-type sliding law did not reproduce this behaviour. In fact, Fig. 3.6 shows that using a higher resolution DeepBedMap_DEM over the lower resolution BedMachine (i.e. more form drag) actually led to a slight increase in inverted form drag τ_b (i.e. more skin drag), contrary to the findings of Kyrke-Smith et al. (2018). The Weertman-style sliding law used by Kyrke-Smith et al. (2018) in their inversion experiments lacks a parameterization of effective pressure N , thus excluding the possible effects of water cavitation (Budd et al., 1979; Gagliardini et al., 2007) or ice flow over deformable till (Zoet & Iverson, 2020). Their Weertman stress exponent value of $m = 3$ also differs from that of Joughin et al. (2019) who recommends using $m = 8$ for a Weertman slip relation to

best match observed velocity data over Pine Island Glacier. It thus remains to be seen whether our findings and those of Kyrke-Smith et al. (2018) reporting on the effects of high resolution topography affecting skin drag can be generalized to more realistic sliding laws, and a wider area of the Antarctic Ice Sheet.

The inversion study here over the main trunk of Pine Island Glacier used a Schoof-type sliding relation on two beds with different spatial resolutions and roughness (i.e. different form drag). Our findings suggest that skin drag (influenced by subglacial water and bed material properties) cannot be ruled out as an important factor in ice dynamics when using a high resolution bed, because basal drag (τ_b , i.e. skin drag) did not noticeably decrease when more form drag was added with the use of a higher resolution (250 m) DeepBedMap_DEM over the medium resolution (500 m) BedMachine (Fig. 3.6). Future modelling work could include better parametrizations of effective pressure N , such as with an evolving subglacial hydrology model (e.g. Sommers et al., 2018). Inversion experiments should also be carried out on even higher resolution (≤ 100 m) bed elevation models (e.g. Graham et al., 2017). A more thorough sensitivity analysis should be carried out to test different values of parameters such as C_{\max} in the Schoof sliding law, and also regularization parameters γ_1 and γ_2 (or others) to see how basal drag τ_b may change in magnitude or spatially. A prognostic forward model run using these high resolution bed elevation models with a Schoof-type sliding law and Full Stokes (or higher order) stress balance equations would also be useful to assess the potential effects of different basal traction and slipperiness fields on Antarctic grounding line migration and its resulting contribution to sea level rise.

Chapter 4

Automated classification of active subglacial lakes in Antarctica from ICESat-2/ATLAS laser altimetry (2018–2020)

Abstract

To examine an aspect of subglacial water movement in Antarctica, we present a new map of active subglacial lakes inferred from spatiotemporal patterns of ice surface elevation trends. An unsupervised density-based classification technique is applied to pre-processed ICESat-2/ATLAS laser altimetry point clouds to detect localized clusters with anomalous rates of elevation change ($> 0.2 \text{ m yr}^{-1}$) over a short period of time ($< 1 \text{ yr}$). These elevation anomaly clusters are inferred to be due to basal water movement. Our compilation counted a total of 194 active subglacial lakes over the 2018-2020 period, including 36 potential new lakes in the 86–88°S area not detected by the previous ICESat (2003-2009) mission. We detail a cascading series of active subglacial lakes exhibiting drain-fill activity along the Whillans Ice Stream central basin, including a rapid ($\sim 7 \text{ m}$ vertical displacement over 3 months) filling event at Subglacial Lake Whillans IX. The high resolution ($< 40 \text{ m}$ along-track spacing) ICESat-2 laser altimetry data also reveal the presence of multi-lobe subglacial lake clusters separated by ridges, with implications for our understanding of subglacial bedforms, and hydrological connectivity along the Siple Coast.

4.1 Introduction

NASA’s Ice, Cloud, and land Elevation Satellite 2 (ICESat-2) laser altimeter launched in 2018 (Markus et al., 2017; Neumann et al., 2019) and has already produced an order of magnitude more data over the previous generation ICESat (2003-2009; Shuman et al., 2006; Zwally et al., 2002), allowing us to map the surface of the Antarctic in great detail. This high data volume presents opportunities to capture glaciological processes at an unprecedented scale, both spatially and temporally. It also comes with computational challenges, prompting a revision to classic analysis techniques. We present an efficient method to identify elevation change from dense point clouds to classify high magnitude ($> 0.2 \text{ m}$), short duration ($< 1 \text{ yr}$) ice surface

elevation change events for subglacial lake detection. Our main contributions are to: (1) extend the inventory of over 400 subglacial lakes reported in Antarctica by Siegfried and Fricker (2018) (see Fig. 4.1), and (2) provide a view of the interaction of subglacial lakes and bedforms in a contemporary setting over the Siple Coast ice streams at seasonal timescales.

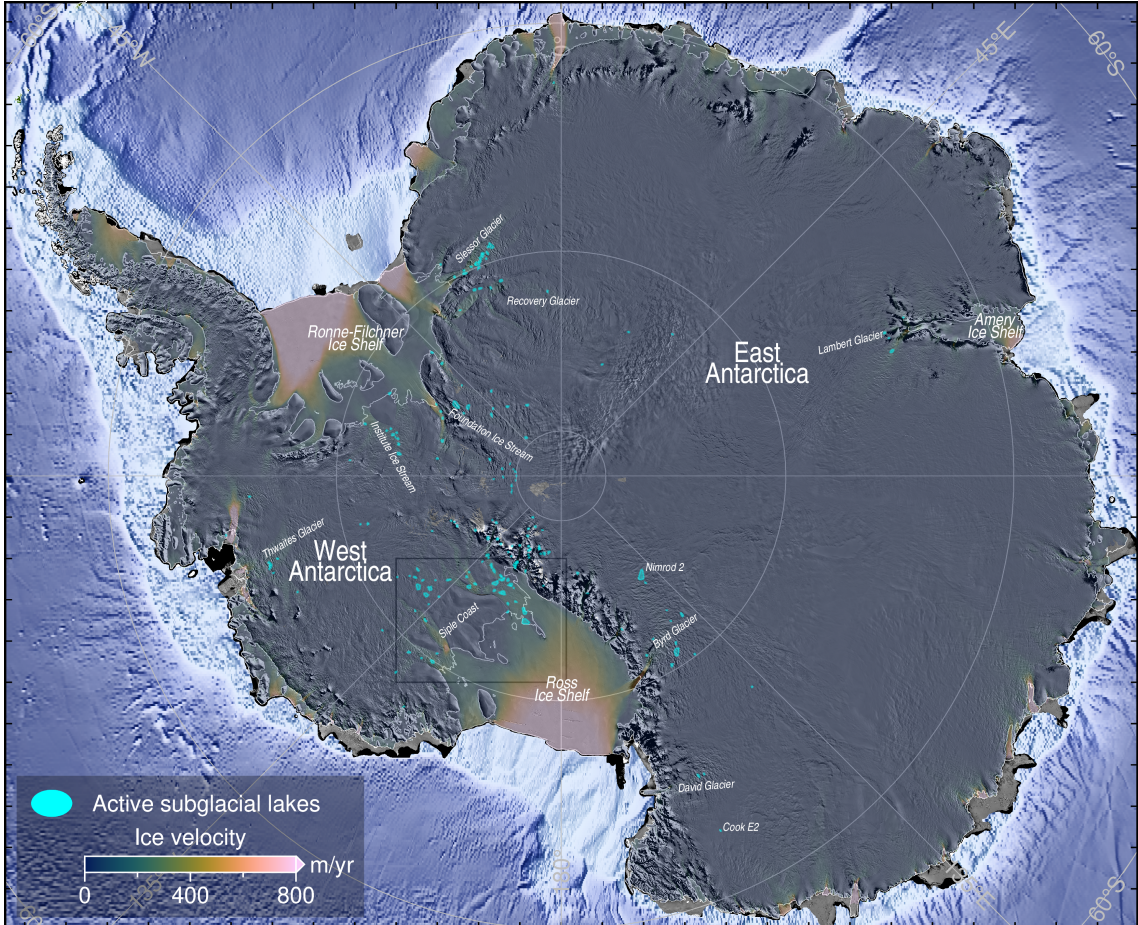


Figure 4.1: Distribution of active subglacial lakes over Antarctica detected by ICESat-2 laser altimetry for the 2018-2020 period. Grounding line and coastline (Depoorter et al., 2013) are plotted as thin white lines. Background image is MODIS Mosaic of Antarctica 2009 (Haran et al., 2014) overlaid with MEaSUREs Phase-based Ice Velocity (Mouginot et al., 2019b), offshore bathymetry is from SRTM15+V2.1 (Tozer et al., 2019). Antarctic place names are labelled in white. Siple Coast study area for Fig. 4.5 is plotted as a black box. Figure produced using PyGMT (Uieda et al., 2020; Wessel et al., 2019) with scientific colour maps (Crameri, 2018). Plotted on an Antarctic Stereographic Projection with a standard latitude of 71°S (EPSG:3031).

4.1.1 Subglacial lakes in Antarctica

In 1967, the first evidence of a subglacial lake in Antarctica was obtained using radio-echo sounding (RES) data obtained by a joint programme between the UK Scott Polar Research Institute, the US National Science Foundation and the Technical University of Denmark (Robin et al., 1969). This work led to the first subglacial lake inventory of 17 lakes (Oswald & Robin, 1973), followed by a second inventory

of 77 lakes (Siegert et al., 1996), and a third inventory of 145 lakes (Siegert et al., 2005), all detected using RES. A fourth inventory with 379 subglacial lakes was compiled, this time including both ‘classic’ RES detected lakes and active subglacial lakes detected by satellite remote sensing (Wright & Siegert, 2012). ‘Classic’ lakes are classified from radar transects on the basis of hydraulic flatness, with a specular reflection across $\geq 5\%$ of its extent while maintaining a reflection coefficient of $\geq 10\text{ dB}$ across 5% of its extent, together with a brightness of $> 2\text{ dB}$ relative to its surroundings (Carter et al., 2007). ‘Active’ lakes are classified on the basis of localized ice volume displacements, whereby a $> 0.1\text{ m}$ elevation anomaly is observed that is not attributed to secular mass imbalance or other errors (see Siegfried & Fricker, 2018; B. E. Smith et al., 2009). In Fig. 4.1, we show the distribution of 194 active subglacial lakes detected on the basis on ICESat-2 laser altimetry vertical elevation change anomalies for the 2018-2020 time period following the methodology described in Sec. 4.2.4.

4.1.1.1 Satellite detected active subglacial lakes

The volume of water in subglacial lakes can change rapidly over sub-annual to annual timescales. Lakes exhibiting such behaviour are termed active subglacial lakes (B. E. Smith et al., 2009), in contrast to ‘classic’ subglacial lakes detected on the basis of specular radar reflections (Carter et al., 2007). If the water volume changes are large enough, these can result in vertical surface displacements that can be detected using satellite remote sensing. Using radar interferometry, Gray (2005) noted a 24-day vertical lowering of $\sim 0.5\text{ m}$ in 1997 over a $\sim 125\text{ m}^2$ area at Kamb Ice Stream or a rate of up to 2 cm per day, with similar vertical displacements detected at the neighbouring Bindschadler Ice Stream. This pattern of vertical surface displacements was interpreted as due to an imbalance in subglacial water input and output from hydropotential depressions. Fricker et al. (2007) used ICESat laser altimetry and MODIS optical image differencing to deduce a network of Siple Coast active subglacial lakes on the basis of geographically localized height change anomalies from 2003 to 2006. They estimated a volume increase of 1.2 km^3 at Subglacial Lake Conway and oscillatory behaviour leading to a net volume increase of 0.12 km^3 at Subglacial Lake Mercer. At Subglacial Lake Engelhardt, $\sim 2.0\text{ km}^3$ of water was estimated to have drained over a period of 2.7 yr .

The ICESat-based lake detection technique was then applied by B. E. Smith et al. (2009) to the whole Antarctic continent, yielding a total of 124 active subglacial lakes, 31 of which had volume ranges $> 0.2\text{ km}^3$. The active subglacial lakes from B. E. Smith et al. (2009) are typically small with $< 20\text{ km}$ widths and a median size of $\sim 13\text{ km}^2$. In contrast to larger lakes like Lake Vostok and the Recovery Lakes which have flat surfaces, many of these small active lakes have a rougher textured surface, making them more difficult to identify using optical imagery. The spatial distribution of these ICESat detected active subglacial lakes was mostly clustered within 200 km of major outlet glaciers and ice streams. Filling and draining patterns of lakes varied across the continent, with no apparent linkage between closely situated lakes in Academy Glacier while a partial linkage was observed between adjacent lakes over Slessor Glacier (B. E. Smith et al., 2009). There appeared to be a direct linkage at Recovery Glacier however, where $\sim 3.0\text{ km}^3$ of water drained from upstream lakes while downstream lakes filled by $\sim 3.1\text{ km}^3$ from November 2002 to February 2008 (B. E. Smith et al., 2009), corroborating previous observations by Bell et al. (2007). Subsequent discoveries have followed to bring the number of

subglacial lakes in Antarctica to above 400 (e.g. Kim et al., 2016; Napoleoni et al., 2020; Rivera et al., 2015; B. E. Smith et al., 2017; Wright et al., 2012; Wright et al., 2014).

4.1.1.2 Geophysical surveys of active subglacial lakes

Several active lakes originally detected by satellite remote sensing were also surveyed using oversnow geophysical methods (e.g. Christianson et al., 2012; Wright et al., 2014). Few showed up with flat, bright specular reflections indicative of a ‘classic’ subglacial lake detected using radar surveys (Carter et al., 2007). This disconnect between oversnow detected ‘classic’ lakes and satellite detected ‘active’ lakes was a puzzle to glaciologists for some years (Siegert et al., 2016). A targeted RES study of Lake Institute E2, previously detected using ICESat (B. E. Smith et al., 2009), yielded non-specular and non-flat radar reflections that did not meet the criteria of a deep-water subglacial lake (Siegert, Ross, Corr, et al., 2014). This discrepancy may be due to a limitation of RES methods that cannot resolve shallow ($< 10\text{ m}$) water bodies owing to very high frequency (VHF, $\sim 60\text{ MHz}$) radio waves penetrating shallow layers and also from interference of RES reflections off the floor and ceiling of subglacial lakes (Gorman & Siegert, 1999). Modelling conducted by Carter et al. (2017) suggests that the water of active subglacial lakes may be stored in soft sediment which would not show as a bright specular surface in RES data. Tulaczyk and Foley (2020) cautioned that the electrical conductivity properties of deformable clay-rich materials as detected by lower frequency radar waves (5 MHz central frequency) could be falsely misinterpreted as subglacial water. The electrical conductivity properties of subglacial materials should thus be carefully accounted for when interpreting the presence or absence of subglacial water from RES data.

One exception is Lake CookE2 in East Antarctica (see Fig. 4.1) which is both an active lake and a ‘classic’ radar lake. CookE2 was originally detected using ICESat laser altimetry by B. E. Smith et al. (2009), and reanalyzed by Cryosat-2 radar altimetry (McMillan et al., 2013) and ASTER and SPOT5 stereo imagery (Flament et al., 2014), with a measured ice surface lowering of $\sim 70\text{ m}$ from November 2006 to October 2008 equivalent to $\sim 6\text{ Gt}$ of water or $\sim 8\%$ of the Antarctic ice sheet’s mass imbalance (Shepherd et al., 2012). An airborne-radar resurvey by Y. Li et al. (2020) showed that Lake CookE2 is bounded by steep topography, with a constrained lake area of $\sim 46\text{ km}^2$ and a minimum lake depth 10 m (Gorman & Siegert, 1999). Based on the bright and smooth reflection observed in the radar transects, Y. Li et al. (2020) derived a lake length and width of $\sim 12.2\text{ km}$ and $\sim 4.1\text{ km}$, smaller than the $\sim 16.6\text{ km}$ and $\sim 9.9\text{ km}$ ICESat measured lake outline (B. E. Smith et al., 2009) derived from a 0.1 m elevation anomaly. There was also no radar evidence for water found in the adjacent hook-shaped zone previously classified as part of the Lake CookE2 based on satellite measured elevation changes. The ICESat derived lake area was as much as six times overestimated compared to that derived from airborne radar-based assessments (Y. Li et al., 2020), cautioning the use of using vertical displacements as the sole basis of inferring true lake outlines.

4.1.1.3 Subglacial lake direct access programmes

To examine subglacial lakes and the boundary condition at the ice-bed interface, several drilling campaigns have directly accessed the bed of the Antarctic ice sheet. The first attempt to drill into a subglacial lake was conducted at Lake Vostok in

February 2012 (Lukin & Vasiliev, 2014). While direct water samples yielded two unknown bacterial phylotypes with no biogeochemical signatures (Bulat, 2016), previous DNA studies from lake accretion ice samples have isolated the thermophile bacteria *Hydrogenophilus thermoluteolus* which indicate near-bottom water temperatures reaching up to 50°C or a geothermal heat flux of 200–240 W m⁻² in the lake sediments (Bulat et al., 2012; Bulat et al., 2004; Talalay et al., 2020), pointing to a direct source of energy for meltwater production. On January 2013, the Whillans Ice Stream Subglacial Access Research Drilling (WISSARD) team managed to successfully sample Subglacial Lake Whillans (Tulaczyk et al., 2014). They found a rich ecosystem of chemolithoautotrophs in a wedge of water only ~ 2.2 m deep under ~ 800 m of ice (Christner et al., 2014; Mikucki et al., 2016). Sediment cores retrieved from Subglacial Lake Whillans were composed of a macroscopically structure-less diamicton similar to subglacial tills found under other ice streams on the Siple Coast, with a shear strength ranging from 2 kPa near the core top, increasing to 6 kPa at 0.2 m below surface (Tulaczyk et al., 2014). The borehole measured 2.2 m lake depth stands in contrast with the 8 ± 2 m depth inferred from seismic measurements done 2 years previously (Horgan et al., 2012), pointing to limitations in the spatial resolution of geophysical methods (Tulaczyk et al., 2014). These direct access studies act to complement and inform remote sensing work, pointing to geothermal heat as a potential source of subglacial lake water, and also providing constraints on the possible forms of water storage and flow across Antarctica's subglacial hydrological system.

4.1.2 Antarctic subglacial water system interactions

4.1.2.1 Sources of subglacial water

The Antarctic ice sheet has low amounts of surface meltwater inputs, making it different from the Greenland ice sheet and temperate glaciers (Bell et al., 2018). While water can be seen on the surface in places close to dark, low-albedo areas like blue ice regions (e.g. Kingslake et al., 2017), the total area of supraglacial lakes detected upstream of the grounding line in East Antarctica is only 253 ± 2.53 km² in 2017 (Stokes et al., 2019), with most developing at low elevations (<100 m) and near rock outcrops (Dierscherl et al., 2020; Stokes et al., 2019). Most of the production of Antarctic subglacial water comes from basal melt processes, either from geothermal heat flow (e.g. Burton-Johnson et al., 2020; Fisher et al., 2015) or frictional heating under fast flowing ice streams (e.g. M. Hoffman & Price, 2014; Zhao et al., 2018). Where there are low hydraulic slopes and less frictional heating from water flow, upstream sources can still contribute significant amounts of subglacial water, such as on the Siple Coast (Alley, 1989; Bougamont et al., 2003). Subglacial water flows from areas of high to low hydraulic potential (see Sec. C), and this flow happens through a dynamic subglacial drainage system which can take varying forms.

4.1.2.2 Subglacial water drainage systems

A range of subglacial pathways have been proposed and observed, ranging from fast flow in concentrated channels, to slower distributed sheet flow and porous groundwater flow (Fig. 4.2; Flowers, 2015). The type of subglacial drainage system is likely to be influenced by factors like bedrock geology, the temperature profile of the ice column, as well as the rate and amount input water into the system (see Flowers,

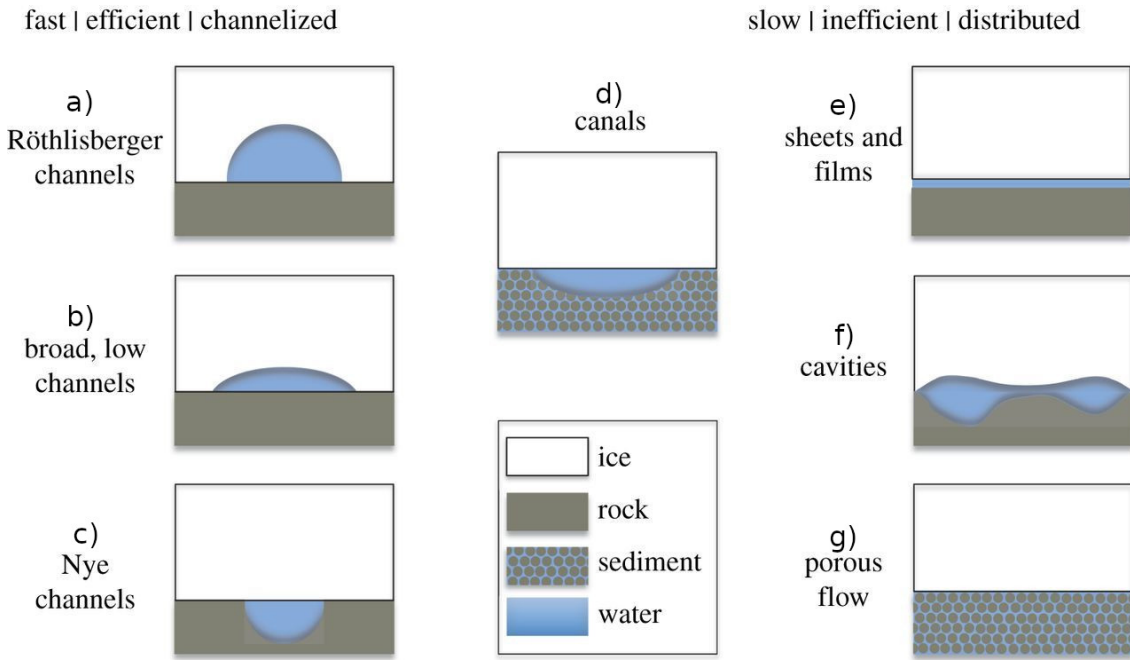


Figure 4.2: Channelized vs Distributed flow in a subglacial drainage system. Figure adapted from Flowers (2015).

2015, for a review). For soft bed types, water can incise into the bed to form Nye channels (Fig. 4.2c, Nye, 1969) or broad shaped canals (Fig. 4.2d, Ng, 2000), flow along cavities (Fig. 4.2f, Lliboutry, 1968), or if the rock is permeable, the water may flow within the rock itself (Fig. 4.2g, Shoemaker, 1986). For hard bed types, water may incise instead into the basal ice, forming semi-circular Röthlisberger channels (Fig. 4.2a, Röthlisberger, 1972) or broad low channels (Fig. 4.2b, Hooke et al., 1990), or flow as a thin sheet of water between the ice-rock interface (Fig. 4.2e, Weertman, 1957). Over space and time, these subglacial drainage structures can change between the two extremes of efficient and inefficient regimes (Fig. 4.2) which has important consequences for ice dynamics (Sec. 4.1.2.4)

4.1.2.3 Drumlins shaped by subglacial water

The type of subglacial drainage system (Fig. 4.2) may play a role in shaping the subglacial terrain. Elongated subglacial landforms oriented parallel to ice flow direction such as flutes, drumlins and mega-scale glacial lineations (see Ely et al., 2016) have been observed beneath Antarctica at Thwaites glacier (Holschuh et al., 2020), Rutford Ice Stream (King et al., 2016) and Whillans Ice Stream (Rooney et al., 1987). However, the formation of such elongated subglacial landforms has only been observed using repeat measurements once in Antarctica, from seismic measurements acquired in 1991, 1997, and 2004 at Rutford Ice Stream by A. Smith et al. (2007). Two main mechanisms of drumlin formation were proposed. The first interpretation is that of a glacial flute (Boulton, 1976) where sediment infills a groove or channel at the base of the ice (e.g. an R-channel, see Fig. 4.2a). The second interpretation is that of a viscous deformation model (e.g. Hindmarsh, 1998), whereby soft underlying till is shaped into drumlin formations. Either way, both these mechanisms share a common requirement for the presence of a soft deformable sediment (e.g. Fig. 4.2d, Fig. 4.2g) that can be reworked into an elongated subglacial landform.

4.1.2.4 The influence of water on ice flow

Glaciers have been observed to flow faster after heavy rainfall or during the spring melt season in alpine settings (e.g. Iken et al., 1983), and in Greenland (Zwally, 2002). Over Antarctica, a review by Fricker et al. (2016) detailed three documented cases of temporary ice acceleration that coincides with active subglacial lake drainage events. Scambos et al. (2011) reported on a subglacial lake drainage event (measured by ICESat laser altimetry) potential linked to a speed up event (measured by image feature tracking) at Crane Glacier, Antarctic Peninsula. Bell et al. (2007) found the onset of rapid flow at the downslope margins of four Recovery subglacial lakes. Over Byrd glacier, subglacial lake drainage has also been linked to glacier acceleration (Stearns et al., 2008; Wright et al., 2014). Still, there has been considerable debate on the influence of water versus topographic controls on the flow of ice. Siegfried et al. (2016) analyzed continuous GPS data on Whillans and Mercer Ice Stream, linking a subglacial flood event with a two year (2012-2013) period of increased ice velocity up to 3.8 % above the previous background trend (2010-2011). However, two separate Subglacial Lake Mercer drainage events were both correlated with increased velocity (in late 2012) and decreasing velocity (late 2014), which points to the varying influence of active subglacial lakes on Antarctic ice flow and the need for better ice sheet models that can capture this level of complex behaviour (Siegfried et al., 2016). Winsborrow et al. (2010) reviewed the locations of ice streams - areas of fast ice flow bounded by slower ice, suggesting that topographic focusing is typically more important than meltwater or soft beds. Over Thwaites Glacier, it has been suggested that extra water had little or no influence on the speed of the lower trunk of Thwaites Glacier, owing to a stronger control by bed topography (A. O. Hoffman et al., 2020; B. E. Smith et al., 2017). Over the Recovery/Slessor/Bailey Region, Diez et al. (2018) suggests that flow in the downstream areas of Recovery Glacier are topographically controlled, while upstream parts are controlled by basal water. The mobility of subglacial water over short timescales and across diverse geographical settings indicate that efficient methods for mapping spatiotemporal patterns of subglacial hydrology are needed, and this forms the focus of the following sections.

4.2 Methods

To map the location of Antarctic active subglacial lakes, we present an automated algorithm focused on elevation time-series data from the ICESat-2 laser altimeter (Markus et al., 2017; Neumann et al., 2019). First, we detail the components of ice surface elevation change over time, and outline methods for measuring these vertical displacements using satellite based sensors. Next, we present a point-cloud based algorithm for detecting active subglacial lake clusters from elevation change anomaly clusters. The algorithm is designed to efficiently leverage the high (60 m along-track spacing) density ICESat-2/ATLAS land ice time-series data product (ATL11; B. E. Smith et al., 2021). We then conduct crossover track analyses over individual lake areas and use it to generate a time-series of ice volume displacement.

4.2.1 Components of ice surface elevation change over time

Surface elevation change over a column of ice is described by Cuffey and Paterson (2010, p.335) as follows:

$$\frac{\delta S}{\delta t} - \frac{\delta B}{\delta t} = \underbrace{\frac{\dot{b}_s}{\rho_s} + \frac{\dot{b}_b}{\rho_i}}_{\text{Accumulation Terms}} - \underbrace{\nabla \cdot \vec{q}}_{\text{Flux Divergence}} - \underbrace{\int_B^S \frac{1}{\rho} \frac{D\rho}{Dt} dz}_{\text{Densification}} \quad (4.1)$$

where ice surface elevation is S , bed elevation is B and time is t . The vertical accumulation terms are made of the surface specific balance rate \dot{b}_s and surface ice density ρ_s , basal specific balance rate \dot{b}_b and basal ice density ρ_i , and rate of mass loss by melt $\dot{\mu}_i$. A glossary description for these terms can be found in Cogley et al. (2011).

The horizontal flux divergence term is calculated as follows:

$$\nabla \cdot \vec{q} = \frac{\delta q_x}{\delta x} + \frac{\delta q_y}{\delta y} \quad (4.2)$$

where q_x and q_y are ice fluxes in the along-flow x and across-flow y direction.

The densification rate $\frac{D\rho}{Dt}$ is calculated as follows:

$$\frac{D\rho}{Dt} = \underbrace{-\rho \left[\frac{\delta u}{\delta x} + \frac{\delta v}{\delta y} + \frac{\delta w}{\delta z} \right]}_{\text{volumetric strain}} - \underbrace{\dot{\mu}_i}_{\text{internal melt}} \quad (4.3)$$

where u, v, w are ice velocities in the x, y and z components respectively. Further details of the derivation of Equations (4.1), (4.2) and (4.3) can be obtained in Whillans (1977) and Reeh et al. (1999).

Our study focuses on changes in the subglacial component δB , but since satellites measure the total change in ice surface elevation $\delta z = \delta S - \delta B$, we need to separate the different surface and basal processes that lead to the total elevation change observed (see Fig. 4.3). As the magnitude of vertical elevation changes and the timespan in which this elevation change occurs differ between surface and basal processes, these elevation time-series patterns can be used to determine the cause of elevation changes. The following paragraphs lists out some of the major components affecting ice surface elevation changes on short (< 1 yr) timescales.

Surface balance

On the surface (air-ice interface), snow accumulation (Fig. 4.3 green) can lead to an increase in elevation, while a decrease in elevation can come from snow compaction (Fig. 4.3 red) or mass wasting processes (Fig. 4.3 blue). Surface processes are seasonally dependent, with a greater increase in elevation due to snow accumulation over the austral winter than in the austral summer due to more firn compaction (Fig. 4.3, Ligtenberg et al., 2012). In Antarctica, accumulation tends to be a slow and gradual process due to the low precipitation over the continent, in the order of $\sim 2 \text{ mm yr}^{-1}$ (Fig. 4.3 green, Arthern et al., 2006). Mass wasting processes (Fig. 4.3 blue) typically occur in fast flowing ice regions like glaciers and ice streams. Over a year, the net contribution of these surface processes are typically in the order of centimetres to tens of centimetres a year. Over a decade, these may amount to about a metre or less of elevation change, and we can observe this stable linear trend in most parts of the Antarctic continent over the satellite era (B. E. Smith, Fricker, Gardner, Medley, et al., 2020).

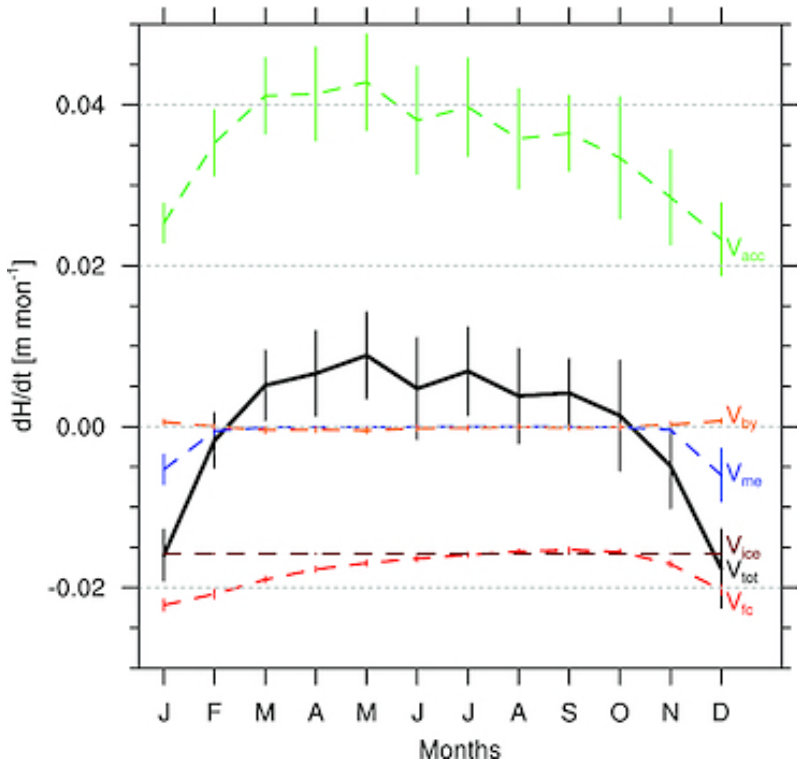


Figure 4.3: Seasonal cycle of ice surface elevation change (dH/dt) over Antarctica. Total monthly surface change (v_{tot} , black) components are: accumulation (v_{acc} , green) and snowmelt (v_{me} , blue), densification/firn compaction (v_{fc} , red), flux divergence/vertical downward movement of ice (v_{ice} , brown) and tidal buoyancy effects (v_{by} , orange). Figure is from Ligtenberg et al. (2012).

Densification

The conversion of snow to firn and then to glacier ice through the process of densification results in a change in the height of an ice column. The rate of densification varies throughout the ice column, and is affected by temperature and the snow accumulation rate (Herron & Langway, 1980). Over Antarctica, thickness change from

densification can be greater than that due to mass-balance changes, and the magnitude of simulated firn depth changes of $\pm 0.2 \text{ m yr}^{-1}$ (Fig. 4.3 red) is a source of uncertainty when converting altimetry derived ice elevation changes to mass balance changes (Helsen et al., 2008). Firn densification is also strongly time-dependent, with winter months showing slower rates of firn compaction due to snow accumulation and summer months showing more firn compaction due to higher temperatures (see Fig. 4.3, Ligtenberg et al., 2011).

Flux divergence

Flux divergence is the vertical component of ice thickness change at a fixed point in space occurring due to ice flow, independent of changes in accumulation, ablation or ice density (Fig. 4.3 brown, see Cogley et al., 2011, p.43). Over Antarctica, this is seen as a dynamic thickening signal over Kamb Ice Stream (B. E. Smith et al., 2005), and dynamic thinning signal over the Amundsen Sea sector and Totten Glacier (Flament & Rémy, 2012; Pritchard et al., 2009).

Basal balance

On the bottom (ice-rock interface), changes in the volume accreted basal ice or subglacial water can also lead to ice surface elevation changes. At Dome A in East Antarctica, RES observations revealed ice accretion plumes up to 1100 m in height that result in a thicker ice column, and the rates of basal ice freeze-on could be greater than surface accumulation rates in localized areas (Bell et al., 2011). The mechanism of subglacial lake drainage and filling events are thought to be through sediment-floored canals at the Whillans Ice Stream in Antarctica (Carter et al., 2017), though predicting the onset of these draining and filling events remain an elusive task. The drainage or filling however, can take place rapidly at time scales of a few days or weeks, with ice surface elevation changes up to a few metres observed (e.g. Siegfried et al., 2016). The pattern of sudden elevation change over a short timescale caused by subglacial water volume changes typically occurs over a limited geographical region of a few square kilometres (e.g. Siegfried & Fricker, 2018; B. E. Smith et al., 2009). This stands in contrast with the background gradual trend in elevation change caused by surface processes. It is this anomalous pattern which is used as the basis of active subglacial lake detection. Besides subglacial water volume changes affecting ice surface elevation, variability in basal traction can also lead to ice surface changes (Gudmundsson, 2003; Raymond & Gudmundsson, 2005; Sergienko et al., 2007).

4.2.2 Active subglacial lake detection from remote sensing

4.2.2.1 Satellite sensors measuring elevation over Antarctica

Several satellite sensors exist to measure ice surface height, such as laser and radar altimeters, or optical photogrammetry (see Fricker et al., 2016, for a review). A comparison of three main satellite-based methods as of 2020 is given below:

REMA stereophotogrammetry

The Worldview-1/2/3 and GeoEye-1 satellites capture optical images, and ice surface elevation estimated via stereophotogrammetry is used to create the Reference Elevation Model of Antarctica (REMA) DEM (Howat et al., 2019). The visible light part of the electromagnetic spectrum (e.g Red, Green, Blue, Infrared bands) detected by optical sensors are affected by cloud cover, and can only work during summer months with daylight. Stereophotogrammetry requires at least two views of the same location taken at different viewpoints to derive the parallax measurement. The Worldview-1/2/3 and GeoEye-1 satellites used by REMA reaches 88°S, with the remainder 2° radius pole hole filled in the REMA mosaic products. Compared to laser and radar altimeters, this method can achieve a high spatiotemporal resolution under cloud-free weather conditions. The REMA strip DEM products have a spatial resolution of 2 m over West Antarctica and 8 m over East Antarctica.

Cryosat-2 radar altimeter

The CryoSat-2/SIRAL radar altimeter (2010- ; Wingham et al., 2006) allows for direct measurement of the ice surface, subjected to a correction for firn penetration. It uses radio waves (Ku band, 13.6 GHz) that is unaffected by cloud cover. Cryosat-2 reaches 88°S. It is less capable of detecting signals over steep undulating topography compared to ICESat-2. In SARIn mode, the beam ‘footprint’ is approximately 380–410 m along-track and 1.7 km across-track (McMillan et al., 2013).

ICESat-2 laser altimeter

The ICESat-2/ATLAS (2018- ; Markus et al., 2017) laser altimeter offers the most precise measurement of the ice surface, with little to no firn penetration. It shoots green 532nm wavelength photon light that is affected by cloud cover. ICESat-2 can reach 88°S which is an additional 2 degrees of latitude over ICESat’s 86°S limit. The ICESat-2/ATLAS instrument’s 6 laser beam architecture allow us to better handle anomalous heights due to cross-track slopes that was a major issue in the previous generation ICESat/GLAS mission. There is an order of magnitude increase in track density, and thus greater coverage of Northern areas of the Antarctica continent, notably near the coastal areas. ICESat-2’s 3 beam pairs are separated by ~ 3 km across-track and beams within a pair separated by ~ 90 m. The laser has a footprint size of 17 m, with an along-track sampling interval of 0.7 m, the ATL06 land ice product has 40 m along-track resolution (B. E. Smith et al., 2019). Assessment of the ICESat-2 ATL06 land ice height product over relatively homogeneous and low-slope areas in Antarctica yielded an vertical accuracy and precision of $\sim 3 \pm 9$ cm (Brunt et al., 2019).

We will focus on the ICESat-2/ATLAS satellite sensor in our study, as it is offers the highest spatial and temporal resolution product for obtaining ice surface height

information. In particular, a more precise cross-track slope correction enabled by ICESat's 6 laser-beam setup allows us to simplify the active subglacial lake detection algorithm in B. E. Smith et al. (2009) considerably. However, the increased data density of ICESat-2 over ICESat also requires a more deliberate data engineering process which will be outlined next.

4.2.3 Measuring rapid height change signals

ICESat-2's ATLAS instrument has six laser beams which pulses at 10 000 Hz compared to the previous generation ICESat's GLAS instrument at 40 Hz (Markus et al., 2017), providing a dense point cloud that enables development of more precise change detection algorithms. To realize the full potential of these dense point clouds, a fundamental rethink is needed in the way we isolate elevation change signals over noise at scale. Lake outline delineation has to shift away from using spatially averaged gridded change measures (c.f. Siegfried & Fricker, 2018; B. E. Smith et al., 2009) to discrete point-based measurements that can capture change exactly at where it is happening, so as to resolve higher spatial resolution outlines at sub-decimetre scales.

This point cloud based revolution of delineating active subglacial lake outlines is enabled by ICESat-2's ATL11 land-ice time-series product (B. E. Smith et al., 2021), based on the ATL06 land-ice height product (B. E. Smith et al., 2019) but with several enhancements conducive to ice elevation time-series analysis. The ATL11 product (B. E. Smith et al., 2021) is created by taking the six tracks from ATL06 and performing a height correction to account for spatial offsets between repeat track measurements (see https://nsidc.org/sites/nsidc.org/files/technical-references/ICESat2_ATL11_ATBD_r002.pdf for more details), resulting in three 'pair' tracks that provide a robust point-based time-series of height measurements.

4.2.3.1 Magnitude of height change h_{range}

In Siegfried and Fricker (2018) and B. E. Smith et al. (2009), active subglacial lakes are detected on the basis of the magnitude of vertical elevation change $h_{range} = h_{max} - h_{min}$. This approach is prone to outliers and requires a pre-processing step to filter out elevation anomalies such as ones caused by cloud interference which lead to incorrect h_{range} values. The pre-filtering step can be too aggressive and may waste data incorrectly classified as false negatives. However, range calculations are fast to compute and scale linearly with the number of data points. They can be used to quickly locate areas that have experienced a significant amount of elevation change. Areas with high h_{range} values can then be analyzed further using regression methods.

4.2.3.2 Rate of ice surface elevation change over time (dh/dt)

The rate of ice surface elevation change over time can be calculated using a linear least-squares regression formula. The rate of elevation change over time $\frac{dh}{dt}$ can be found through a linear regression of data points elevation h_0 at time t_0 until h_n at time t_n . This is more computationally expensive than the h_{range} calculation, and thus more effort is required to scale it to continent-wide analysis. This approach is more robust to outliers than h_{range} . While pre-processing steps can be used, it is not an essential requirement and the filters can be less aggressive to minimize

waste of false negative data. In the case of ICESat-2, this pre-processing filter can be done on the basis of quality assessment criteria such as the photon return signal. Alternatively, a weighted linear regression can be used to give more weight to good data points (i.e. those less affected by clouds) and less weight to the anomalous points, thereby keeping data culling to a minimum.

Still, we may need to account for temporal dependence when interpreting rate of elevation change $\frac{dh}{dt}$ at any given point. Details in the elevation trend may be masked, for example, if the surface were to rise at t_1 and fall at t_2 , resulting in a $\frac{dh}{dt}$ value that may not indicate a significant change. The short two-year time period (2018-2020) used in this study allows us to neglect this temporal dependence effect, but $\frac{dh}{dt}$ should be interpreted carefully when using longer term time-series data to avoid masking out elevation anomalies with a cyclic nature.

4.2.4 Clustering active lakes: Using DBSCAN

To detect subglacial lake clusters directly on our dense point cloud, we utilize the Density-based spatial clustering of applications with noise (DBSCAN) algorithm (Schubert et al., 2017). DBSCAN is an unsupervised classification algorithm that does not require the operator to pre-determine the number of clusters (as with K-means clustering). It is suited ideally for our active subglacial lake detection task, as it can handle non-spherical shapes. There are only two parameters that need to be set. ϵ defines the maximum distance between which two points can be linked in a cluster. To filter out outliers, there is a $minPts$ setting that sets the minimum number of points in a neighborhood (ϵ) surrounding a point which is needed such that the point is considered to be a core point of a cluster.

Algorithm 1 Subglacial Lake Finder algorithm

```

for basin in basins do            $\triangleright$  loop through each Antarctic drainage basin
    Let basin_points be a set of points inside the drainage basin with  $\frac{dh}{dt}$  values
    Let x be an empty point database to store filtered points
    tolerance  $\leftarrow 3 \times \text{Median}(|\text{basin\_points}|)$ 
    for basin_point in basin_points do
        if basin_point  $\geq$  tolerance then  $\triangleright$  Find points with above average dhdt
            Add basin_point to x
        end if
    end for
    lakes_drain  $\leftarrow$  DBSCAN(x with  $\frac{dh}{dt} < 0$ )            $\triangleright$  Labelled draining lake points
    lakes_fill  $\leftarrow$  DBSCAN(x with  $\frac{dh}{dt} > 0$ )            $\triangleright$  Labelled filling lake points
    lakes  $\leftarrow$  lakes_drain  $\oplus$  lakes_fill            $\triangleright$  Concatenate all lakes
    return lakes
end for

```

Full details of the active subglacial lake finder algorithm are presented in pseudocode format at Algorithm 1. Empirically, we determine DBSCAN parameter values of $\epsilon = 3000$ m (same as the across-track spacing of ICESat-2's 3 laser beam pairs) and $minPts = 300$ to work well for finding potential elevation anomaly clusters while isolating spurious elevation change signals (e.g. due to cloud cover or steep slopes).

The resulting set of potential active subglacial lake clusters (both draining and filling lakes), are then passed though a post-processing stage to prune out false

positive lakes. The criteria in this post-processing filtering algorithm is adapted from those used in the ICESat (2003-2009) (Fricker et al., 2007; B. E. Smith et al., 2009) and Cryosat-2 (2013-) (e.g. Kim et al., 2016; Siegfried & Fricker, 2018) missions, but revised for the current ICESat-2 (2018-) mission. Full details of the subglacial lake filtering algorithm are presented in pseudocode format at Algorithm 2.

Algorithm 2 Subglacial Lake Filtering algorithm

Require: *lakes*

```

Let lakedb be an empty lake database to store filtered lakes
for lake in lakes do
    Let pointsinner be a set of points inside the potential lake with  $\frac{dh}{dt}$  values
     $dhdt_{inner} \leftarrow \text{Median}(\text{points}_{inner})$ 
     $lake\_polygon \leftarrow \text{ConvexHull}(\text{points}_{inner})$ 
    Let pointsouter be all points within a 5000m buffer zone outside the
    lake_polygon
     $dhdt_{outer} \leftarrow \text{Median}(\text{points}_{outer})$ 
     $mad_{outer} \leftarrow \text{Median}(|\text{points}_{outer} - dhdt_{outer}|)$   $\triangleright$  Median Absolute Deviation of
    pointsouter
    if  $|dhdt_{inner} - dhdt_{outer}| \geq 3 \times mad_{outer}$  then
        Add lake_polygon to lakedb
    end if
end for
return lakedb

```

Algorithm 2 produces a database of lake polygon outlines *lakedb* directly from ICESat-2 points using a convex hull (Barber et al., 1996) without the use of an intermediate grid interpolation step. This database of active subglacial lake boundaries *lakedb* is supplemented with additional statistics within and outside of the subglacial lake's perimeter. Inside the polygon, we include the maximum absolute elevation change over time ($\max |\frac{dh}{dt}|$) as well as the median and mean elevation change over time ($dhdt_{inner}$, \overline{dhdt}). Outside the polygon, we store information on the background median elevation change over time ($dhdt_{outer}$) as well as the median absolute deviation and standard deviation of elevation change over time values (mad_{outer} , std_{outer}). The database *lakedb* also includes a list of ICESat-2 reference ground track number and laser pair names (*refgtracks*) crossing the polygon area.

Owing to the dynamic nature of these subglacial lake activity, wherein lakes can drain in a matter of weeks or months, we have automated the procedure to make it easier to get into more detailed analysis sooner. The automation allows us to detect such events every season, or every month, depending on data availability.

4.2.5 Crossover track analysis and ice volume displacement

Once the lake outlines are obtained, we conducted further crossover analysis to generate a higher temporal resolution (< ICESat-2's 91-day repeat cycle) elevation change time-series on areas of interest (see Fig.4.4). We utilized the x2sys_cross package (Wessel, 2010), setting a maximum crossover distance threshold of 250 m, with crossover values linearly interpolated from their actual track points. For each crossover point, an elevation anomaly time series is generated by subtracting the

crossover elevation at any time (h_n at t_n) with the first crossover elevation value (h_0 at t_0). The crossover elevation anomalies of individual lakes will be presented in Sec. 4.3.2 in conjunction with an ice surface elevation plot and an along-track transect plot.

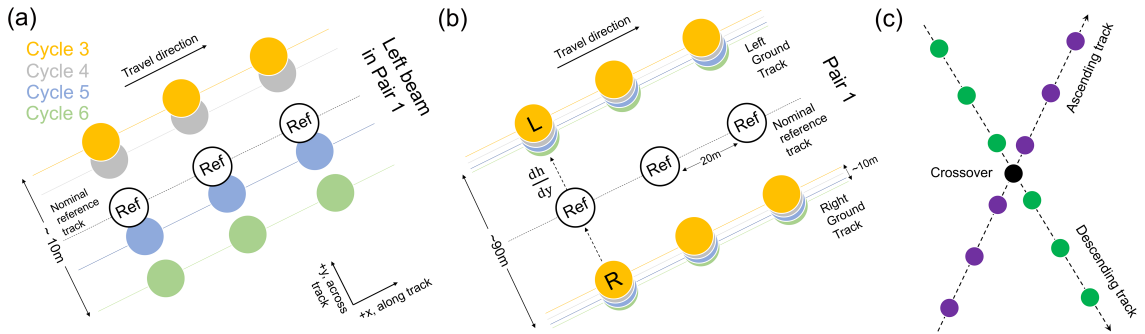


Figure 4.4: Schematic of ICESat-2 altimetry repeat-track and crossover-track analysis. **a** Repeat-track analysis on a single ICESat-2 beam pair over four ICESat-2 cycles, with each cycle repeating over the same reference track every 91 days. **b** Closeup view of a single ICESat-2 beam pair separated into left and right tracks. These two tracks in an ATL06 beam pair are normalized into a single track in the ATL11 product after cross-track slope corrections are applied, as illustrated by the nominal reference track (black) in the middle. **c** Crossover-track analysis is conducted at the interpolated intersection point (black) of two tracks - the ascending track (purple) and descending track (green). Figure is from T. Li et al. (2020), licensed under CC-BY-4.0.

A time-series of ice volume displacement is estimated by multiplying lake area with elevation anomalies, following Kim et al. (2016) and Siegfried et al. (2016). Specifically, we use the rolling mean of the elevation anomaly crossover time-series over a 91 day period. Siegfried et al. (2016) recommends using the term ice volume displacement, which represents an upper limit on likely basal water volume changes. These ice volume displacement results will be presented in Sec. 4.4.3.

4.3 Results

4.3.1 ICESat-2 active subglacial lake inventory

Here we present an inventory of Antarctic active subglacial lakes for the time period 2018–2020 as detected by ICESat-2 laser altimetry. The Antarctic-wide inventory (Fig. 4.1) consists of individual lake polygons classified using elevation anomalies (Sec. 4.2.4). ICESat-2’s increased spatial data density identified a greater distribution of Antarctic active subglacial lakes, including 36 potential new lakes in the 86–88°S area missing from the previous ICESat mission (Fig. 4.1). Instead of ~ 131 active subglacial lakes with a combined area of $\sim 25\,793\text{ km}^2$ detected over 13 years (Siegfried & Fricker, 2018), we detected ~ 194 active subglacial lakes with a combined area of $\sim 15\,688\text{ km}^2$ over 2 years (Fig. 4.1). Elevation anomaly clusters prevalent along the Siple Coast (Fig. 4.5) are explored in Sec. 4.3.1.1.

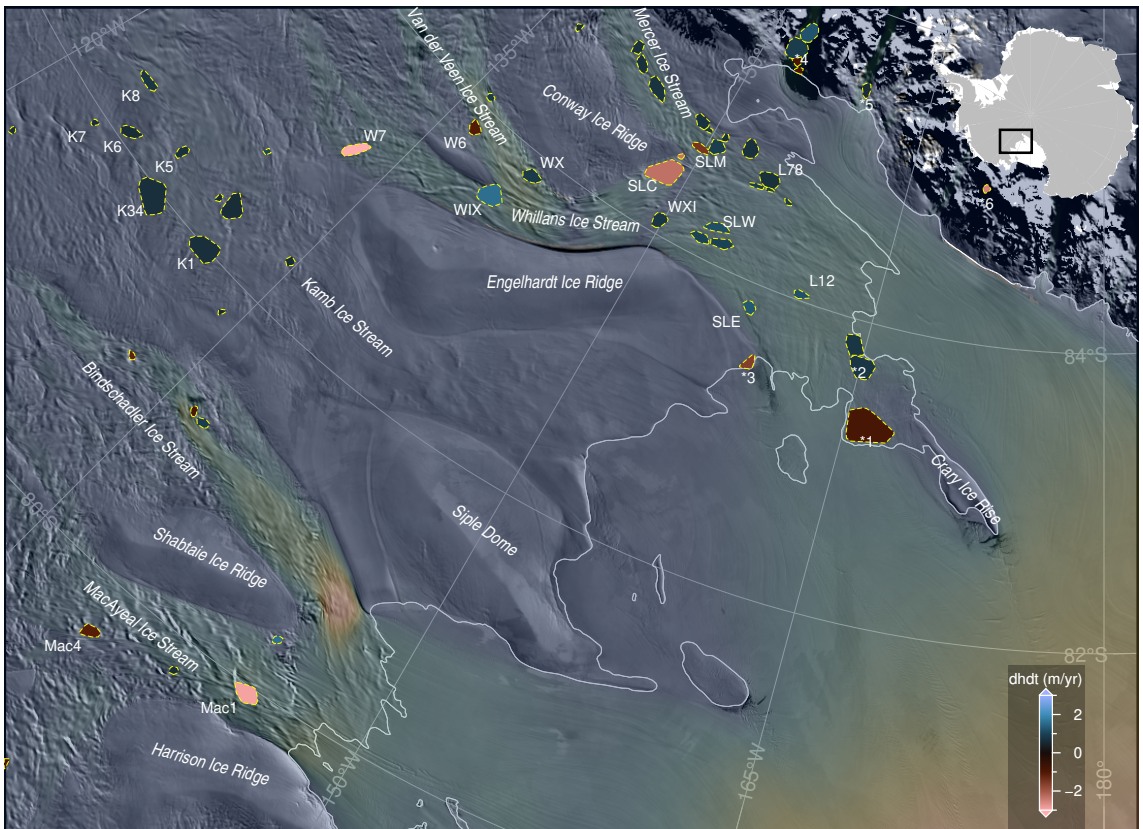


Figure 4.5: Siple Coast active subglacial lakes detected by ICESat-2 laser altimetry. Coloured polygons show areas with elevation anomalies (high $|dhdt|$) from 2018-10-14 to 2020-11-11, going from red (surface lowering) to blue (surface uplift). Selected active subglacial lakes and other features of interest (denoted with an asterisk *) are labelled in white. Abbreviations are: Mac1: MacAyeal 1, Mac4: MacAyeal 4, K1: Kamb 1, K34: Kamb 34, K5: Kamb 5, K6: Kamb 6, K8: Kamb 8, SLE: Subglacial Lake Engelhardt, SLW: Subglacial Lake Whillans, WIX: Whillans IX, WX: Whillans X, WXI: Whillans XI, W6: Whillans 6, W7: Whillans 7, L12: Lake 12, L78: Lake 78, SLM: Subglacial Lake Mercer, SLC: Subglacial Lake Conway. Grounding line (Depoorter et al., 2013) is plotted as a white line. Ice flow is from top left to bottom right. Plotted on an Antarctic Stereographic Projection with a standard latitude of 71°S (EPSG:3031).

4.3.1.1 Siple Coast active subglacial lakes

Active subglacial lake boundaries classified from the DBSCAN-based algorithm (Sec. 4.2.4) that coincide with previous lake inventories (Siegfried & Fricker, 2018; B. E. Smith et al., 2009) are labelled in Fig. 4.5 alongside some newly discovered lakes labelled with roman numerals (Whillans IX, X and XI). Over MacAyeal Ice Stream, the algorithm detected two draining lakes - MacAyeal 1 (Mac1) and MacAyeal 4 (Mac4) documented in Fricker et al. (2010), and two potential new active subglacial lakes, one filling between Mac1 and Mac4, one filling to the South of Mac1 next to Shabtaie Ice Ridge. Over Bindschadler Ice Stream three small elevation anomaly clusters are identified, one pair which is draining and filling close together, and a further one upstream to the West that is draining. Over Kamb Ice Stream, the algorithm detected filling lakes Kamb 1 (K1), Kamb 34 (K34, see also Kim et al., 2016), Kamb 5 (K5), Kamb 6 (K6), Kamb 7 (K7) and Kamb 8 (K8) originally reported in B. E. Smith et al. (2009).

Further South along the Siple Coast, more clusters of elevation anomalies/active subglacial lakes are identifiable, with some forming mega-clusters. Over the upstream area of Whillans Ice Stream, the algorithm detected lakes Whillans 6 (W6) and Whillans 7 (W7) reported in B. E. Smith et al. (2009), and three other filling lakes including Whillans IX (WIX) to be discussed in Sec. 4.3.2. Over the downstream area of Whillans Ice Stream, the algorithm detected Subglacial Lake Conway (SLC), Subglacial Lake Engelhardt (SLE), Subglacial Lake Whillans (SLW) and Lake 12 (L12) reported in Fricker and Scambos (2009), and a new filling lake named Whillans XI (WXI) upstream of Subglacial Lake Whillans. Note that SLC exists as a mega-cluster of 2 draining lakes, and SLW (see also Sec. 4.3.2) is a mega-cluster consisting of 3 filling lakes. Over Mercer Ice Stream, the algorithm detected Lake 78 (L78; see also Siegfried & Fricker, 2018) and Subglacial Lake Mercer (SLM) reported in Fricker and Scambos (2009), as well as one new filling lake upstream. Note that L78 exists as a mega-cluster of 4 filling lakes, and SLM consists of 3 lakes - one draining and two filling.

Some potentially erroneous classifications (*1 to *6 in Fig. 4.5) were also made. Sites *1 and *2 located upstream of Crary Ice Rise are unlikely to be active subglacial lakes because they are close to the grounding zone and exhibit oscillatory elevation anomaly patterns indicative of tidal cycle based fluctuations. Site *3 downstream of Subglacial Lake Engelhardt is likely the location of crevassing at the grounding zone transition which resulted in an elevation lowering. Sites *4, *5, and *6 are likely false positive lakes misclassified from altimetry errors over the steep topography of the Transantarctic Mountains.

In the following, we focus on analyzing surface elevation change along the Whillans Ice Stream central catchment saw a series of potentially connected elevation anomalies, including one cluster (Whillans IX) not identified in any previous lake inventory

4.3.2 Active subglacial lakes at Whillans Ice Stream central basin

To examine the spatiotemporal patterns of individual active subglacial lakes in greater detail, we present a time-series analysis using our methodology in Sec. 4.2.5, focusing on the Whillans Ice Stream at the Siple Coast (Fig. 4.5). Results are shown via 1) crossover analysis, 2) DEM differencing, and 3) Along track plots.

Whillans 7

At Whillans 7, a decrease in ice surface elevation occurred from November 2019 to November 2020 (Fig. 4.6). Within the lake area of $\sim 125.24 \text{ km}^2$ (Fig. 4.7), the median rate of elevation change is $\sim -3.03 \text{ m yr}^{-1}$ while the mean rate of elevation change is $\sim -3.30 \text{ m yr}^{-1}$. The maximum vertical displacement observed over the time period is $\sim -7.32 \text{ m}$, translating to a maximum rate of elevation change of $\sim -9.82 \text{ m yr}^{-1}$, concentrated at the Western part (right-hand side of Fig. 4.8) of the subglacial lake.

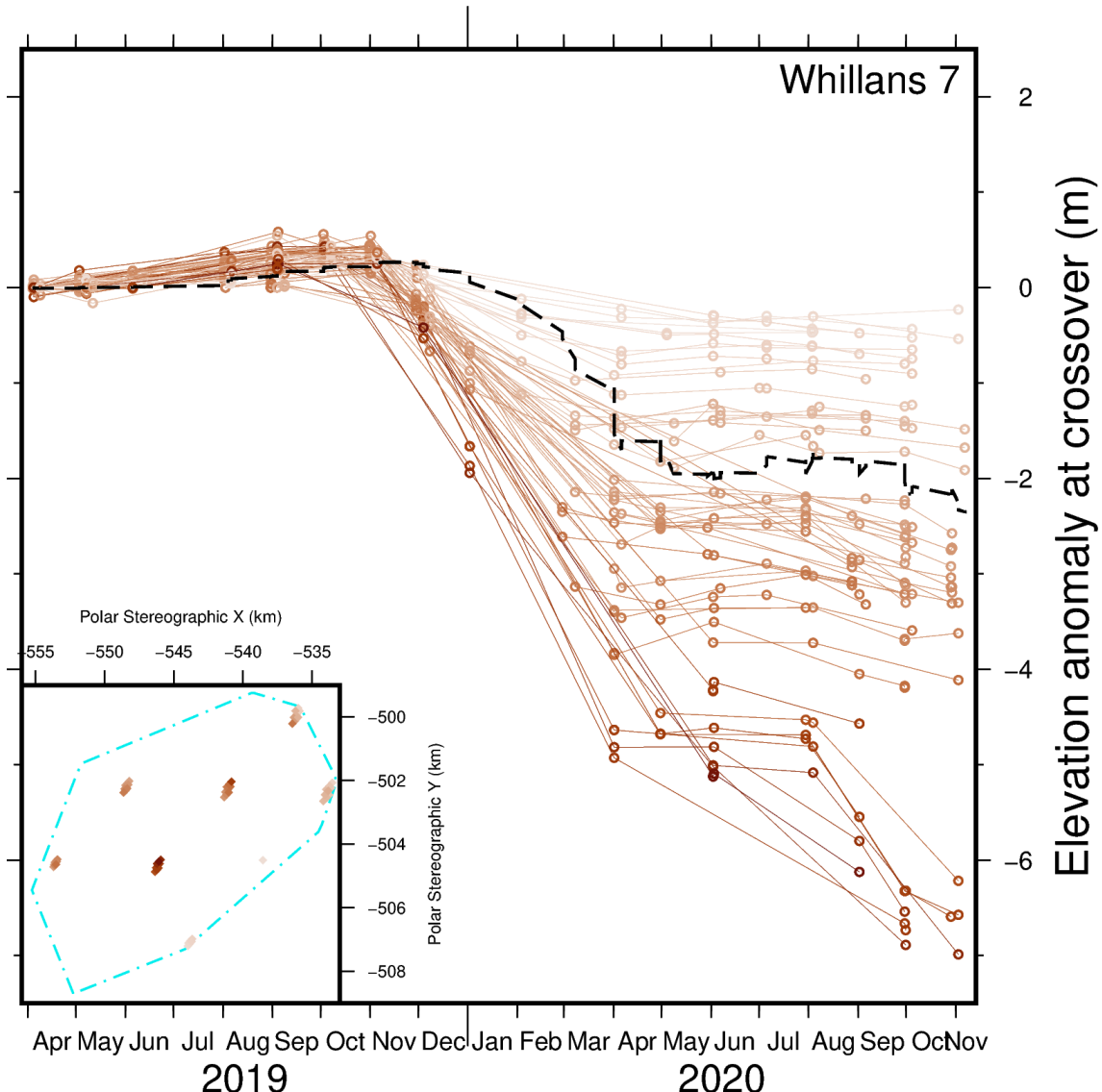


Figure 4.6: Elevation anomaly of crossover points within Whillans 7. 91 day rolling mean of elevation anomalies shown as black dashed line. Inset plot shows locations of crossover points (brown) within lake outline (cyan).

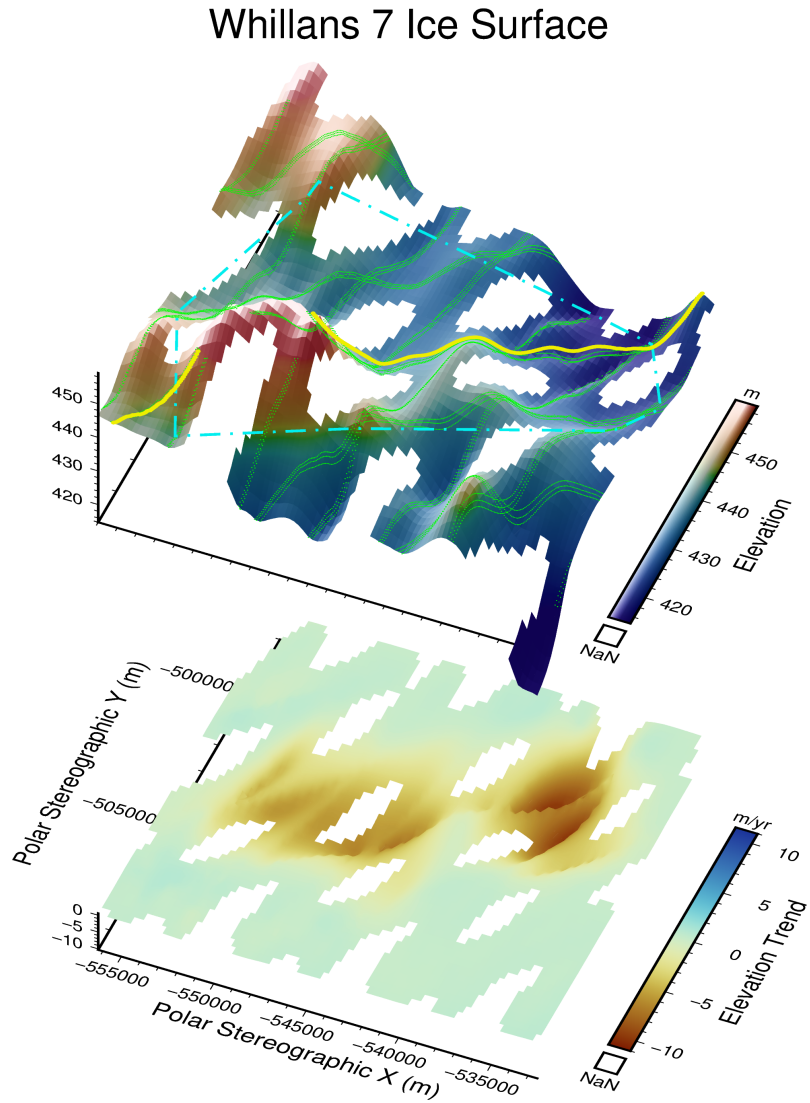


Figure 4.7: Top: Digital Surface Elevation Model at Whillans 7 from interpolating the mean elevation measured by ICESat-2 over 2018-2020. Overlaid on top are ICESat-2 points (green), transect line in Fig. 4.8 (yellow) and lake outline (cyan). Bottom: Trend map of ice surface elevation change over time (dhdt).

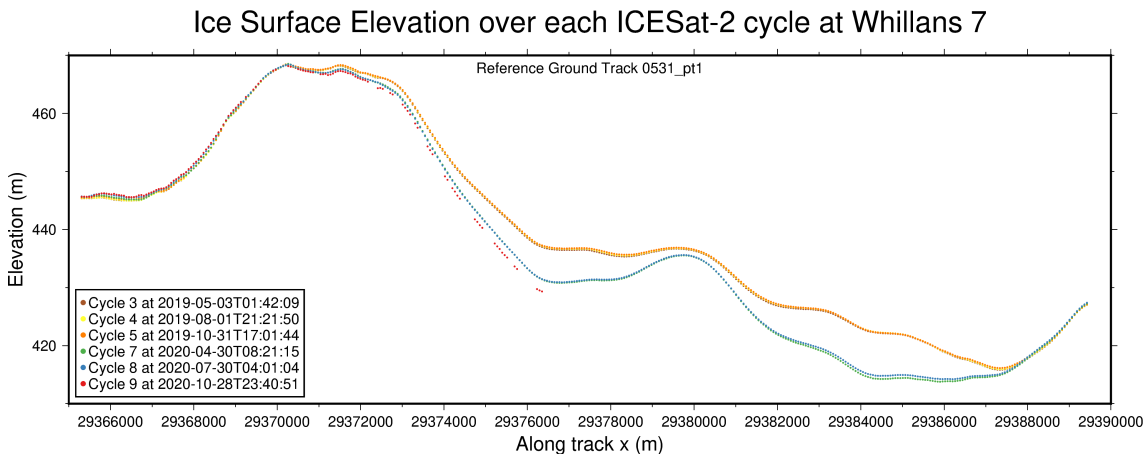


Figure 4.8: Along track view of ice surface elevation over Whillans 7 from ICESat-2 Cycle 3 to Cycle 9. Ice surface elevation is changing by $\sim 10 \text{ m yr}^{-1}$ over a distance of $\sim 14 \text{ km}$ for this lake.

Whillans IX

At Whillans IX, an increase in ice surface elevation occurred from November 2019 to March 2020 (Fig. 4.9). Within the lake area of $\sim 221.22 \text{ km}^2$ (Fig. 4.10), the median rate of elevation change is $\sim 1.57 \text{ m yr}^{-1}$ while the mean rate of elevation change is $\sim 1.92 \text{ m yr}^{-1}$. The maximum vertical displacement observed over the time period is $\sim 7.60 \text{ m}$, translating to a maximum rate of elevation change of $\sim 7.26 \text{ m yr}^{-1}$, concentrated at the Western part (right-hand side of Fig. 4.11) of the subglacial lake centred around EPSG:3031 X:-445000, Y:-535000.

Subsequently from March 2020 to November 2020, the ice surface elevation decreased gradually over time. The transect view of the lake (Fig. 4.11) shows that the Western lobe (which previously experienced the most sudden rapid rise) lowered in elevation by $\sim 2 \text{ m}$, while the Eastern (left-hand side of Fig. 4.11) lobe saw a slight uplift of $<1 \text{ m}$.

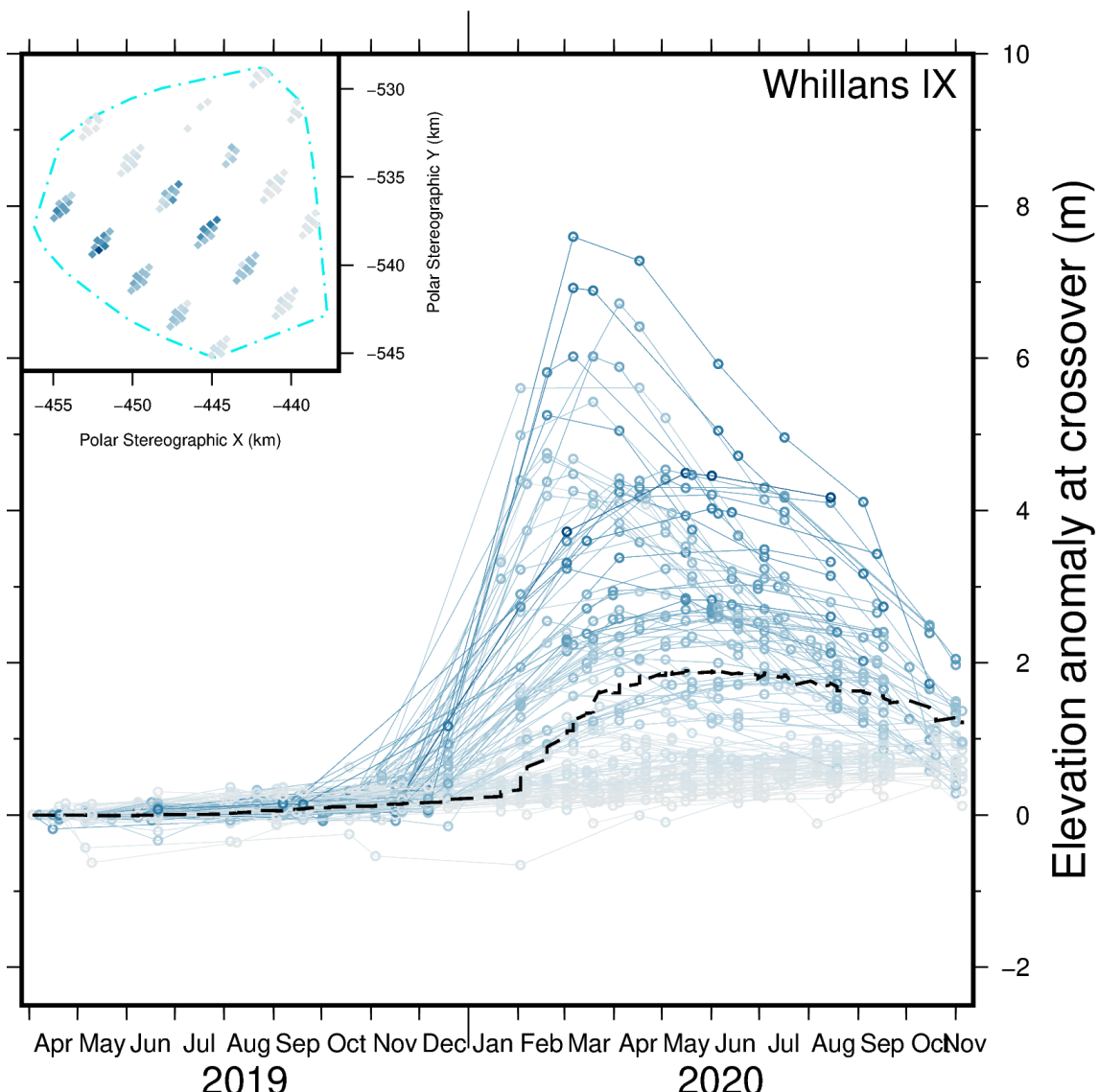


Figure 4.9: Elevation anomaly of crossover points within Whillans IX. 91 day rolling mean of elevation anomalies shown as black dashed line. Inset plot shows locations of crossover points (blue) within lake outline (cyan).

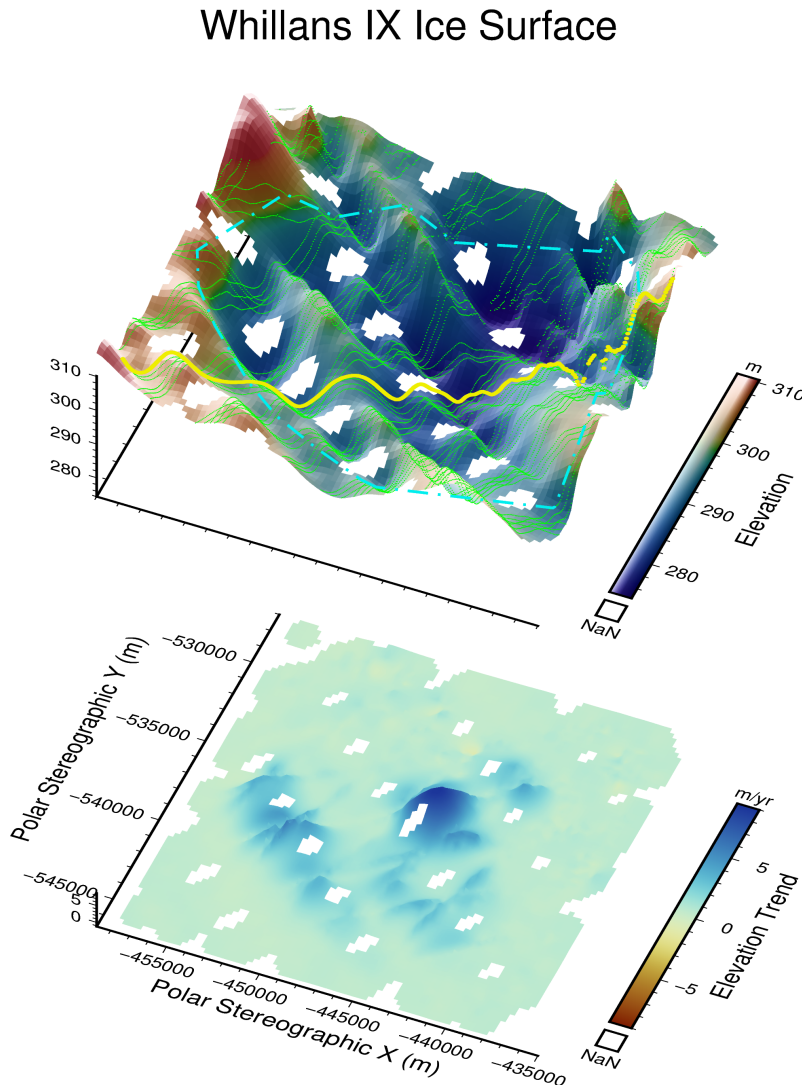


Figure 4.10: Top: Digital Surface Elevation Model at Whillans IX from interpolating the mean elevation measured by ICESat-2 over 2018-2020. Overlaid on top are ICESat-2 points (green), transect line in Fig. 4.11 (yellow) and lake outline (cyan). Bottom: Trend map of ice surface elevation change over time (dhdt).

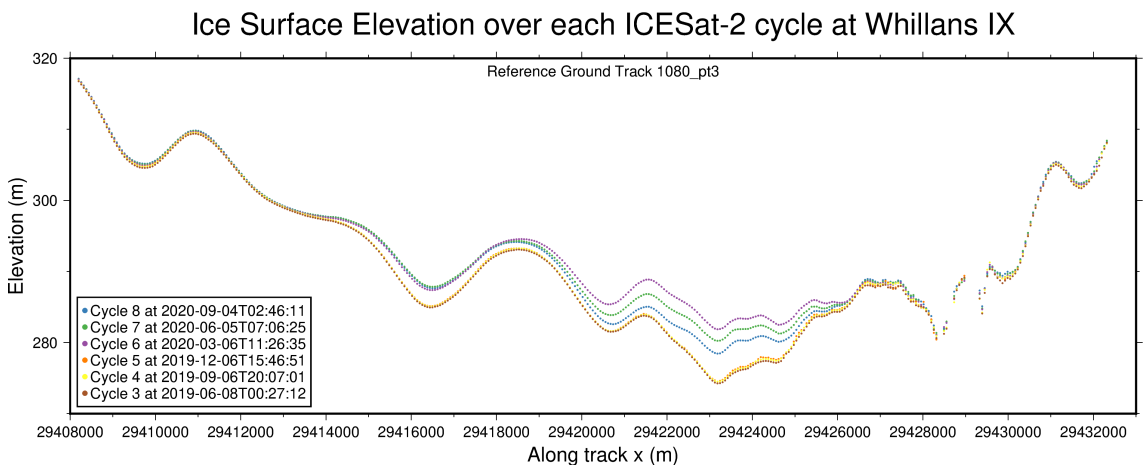


Figure 4.11: Along track view of ice surface elevation over Whillans IX from ICESat-2 Cycle 3 to Cycle 8. Ice surface elevation is changing by $\sim 7 \text{ m yr}^{-1}$ over a distance of $\sim 11 \text{ km}$ for this lake.

Subglacial Lake Whillans

At Subglacial Lake Whillans, an increase in ice surface elevation occurred from April 2019 to November 2020 (Fig. 4.12) across three separate clusters (Fig. 4.13). Within the combined lake area of $\sim 265.05 \text{ km}^2$ (Fig. 4.13), the median rate of elevation change is $\sim 1.01 \text{ m yr}^{-1}$ while the mean rate of elevation change is $\sim 1.05 \text{ m yr}^{-1}$. The maximum vertical displacement observed over the time period is $\sim 4.68 \text{ m}$, translating to a maximum rate of elevation change of $\sim 1.90 \text{ m yr}^{-1}$, concentrated at the Southern cluster (right-hand side of Fig. 4.14). A ridge $\sim 6 \text{ km}$ wide separates the Southern Subglacial Lake Whillans from two other Northern clusters. The two Northern elevation anomaly clusters themselves are separated by a distance of $\sim 1 \text{ km}$.

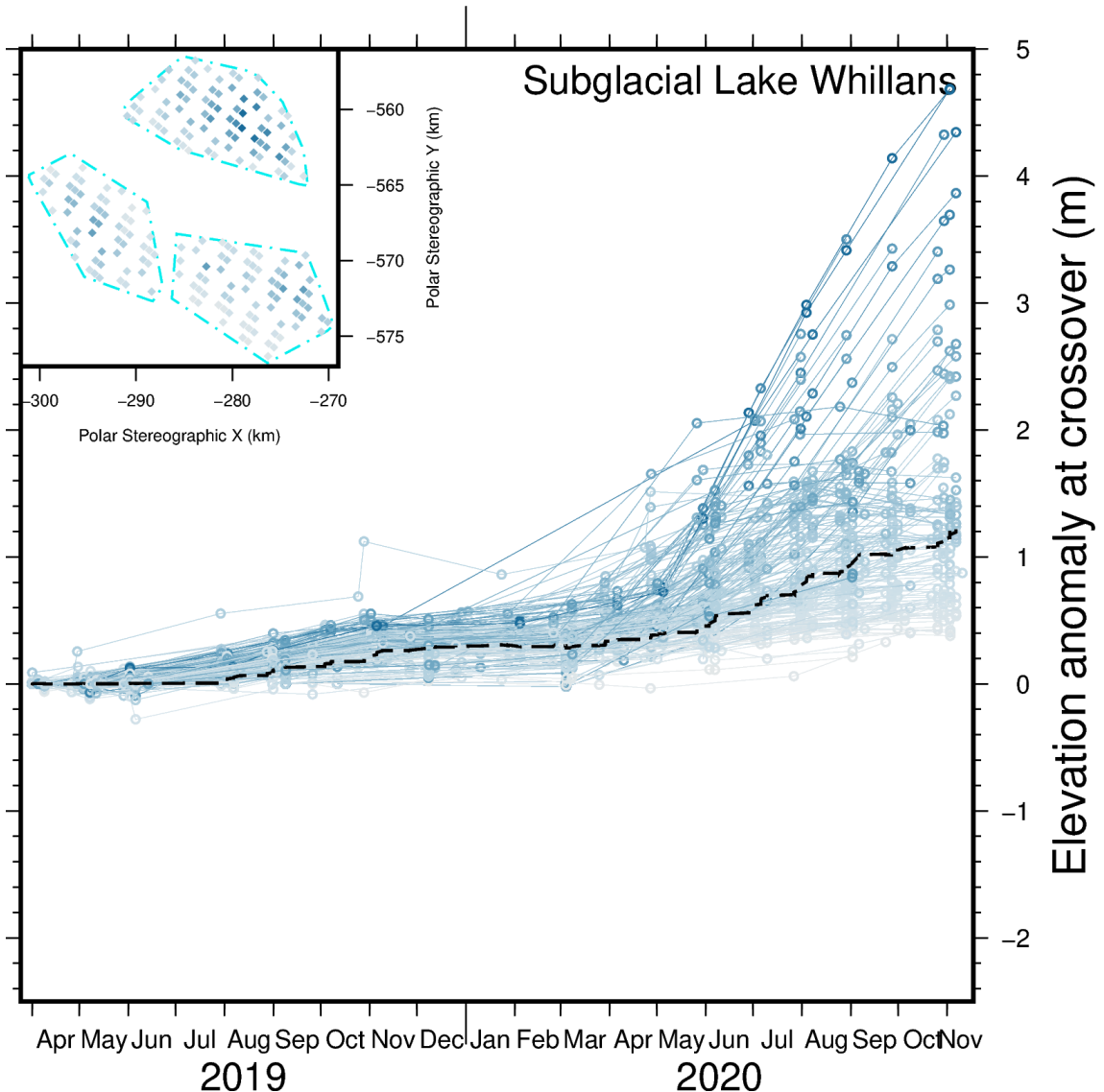


Figure 4.12: Elevation anomaly of crossover points within Subglacial Lake Whillans. 91 day rolling mean of elevation anomalies shown as black dashed line. Inset plot shows locations of crossover points (blue) within lake outline (cyan).

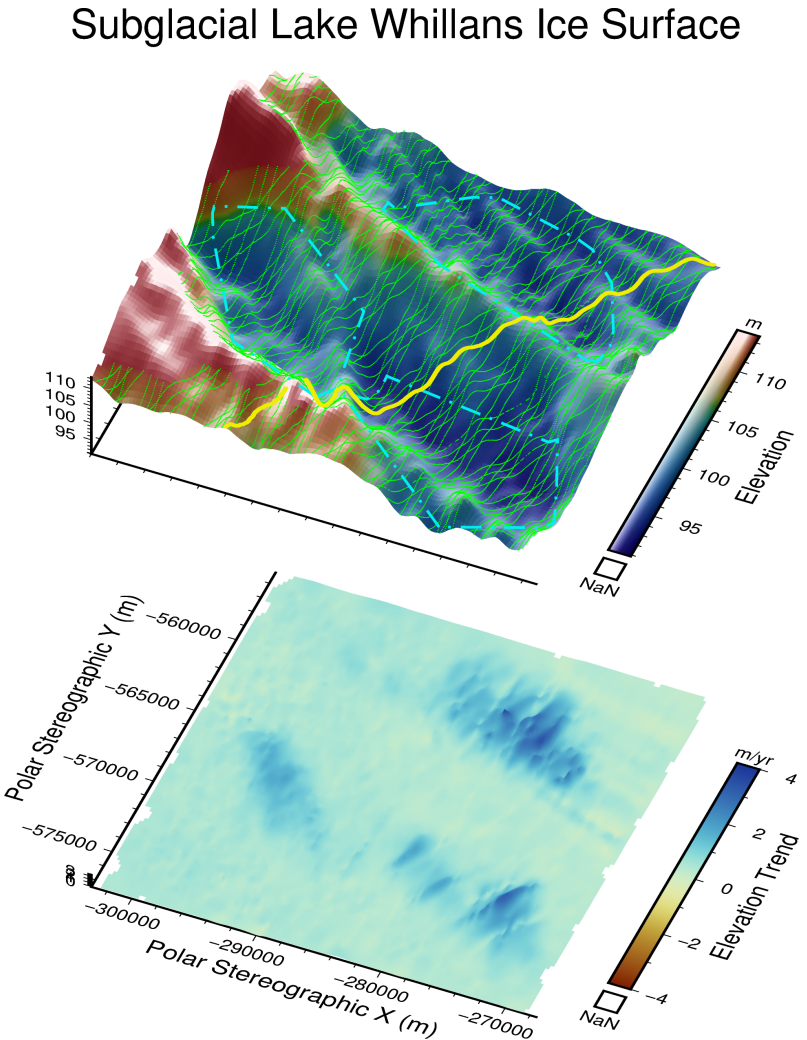


Figure 4.13: Top: Digital Surface Elevation Model at Subglacial Lake Whillans from interpolating the mean elevation measured by ICESat-2 over 2018-2020. Overlaid on top are ICESat-2 points (green), transect line in Fig. 4.14 (yellow) and lake outline (cyan). Bottom: Trend map of ice surface elevation change over time (dhdt).

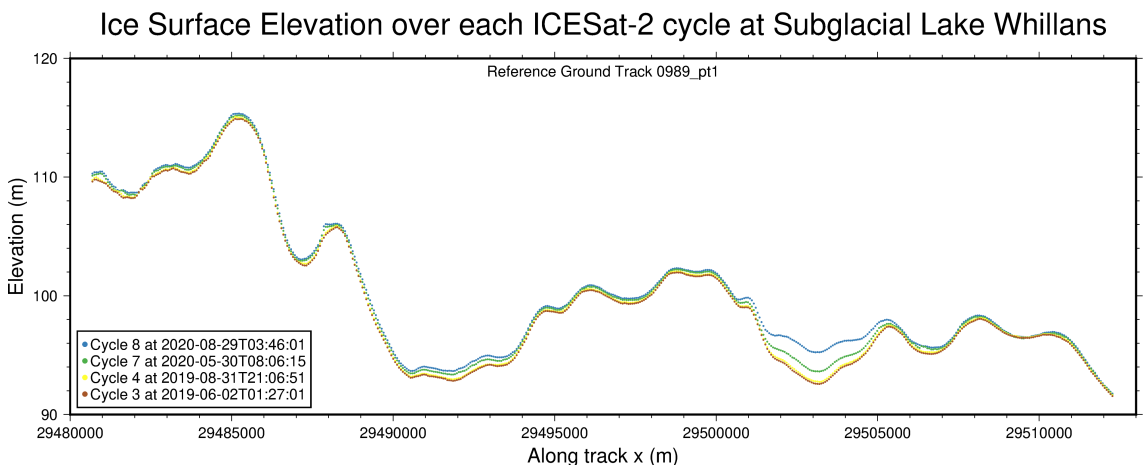


Figure 4.14: Along track view of ice surface elevation over Subglacial Lake Whillans from ICESat-2 Cycle 3 to Cycle 8. Ice surface elevation is changing by $\sim 2 \text{ m yr}^{-1}$ over a distance of $\sim 4 \text{ km}$ for the Southern (right-side) lake.

Lake 12

At Lake 12, an increase in ice surface elevation occurred from June 2020 to November 2020 (Fig. 4.15). Within the lake area of $\sim 50.57 \text{ km}^2$ (Fig. 4.16), the median rate of elevation change is $\sim 1.20 \text{ m yr}^{-1}$ while the mean rate of elevation change is $\sim 1.36 \text{ m yr}^{-1}$. The maximum vertical displacement observed over the time period is $\sim 4.24 \text{ m}$, translating to a maximum rate of elevation change of $\sim 3.55 \text{ m yr}^{-1}$, concentrated at the Eastern part (left-hand side of Fig. 4.17) of the subglacial lake.

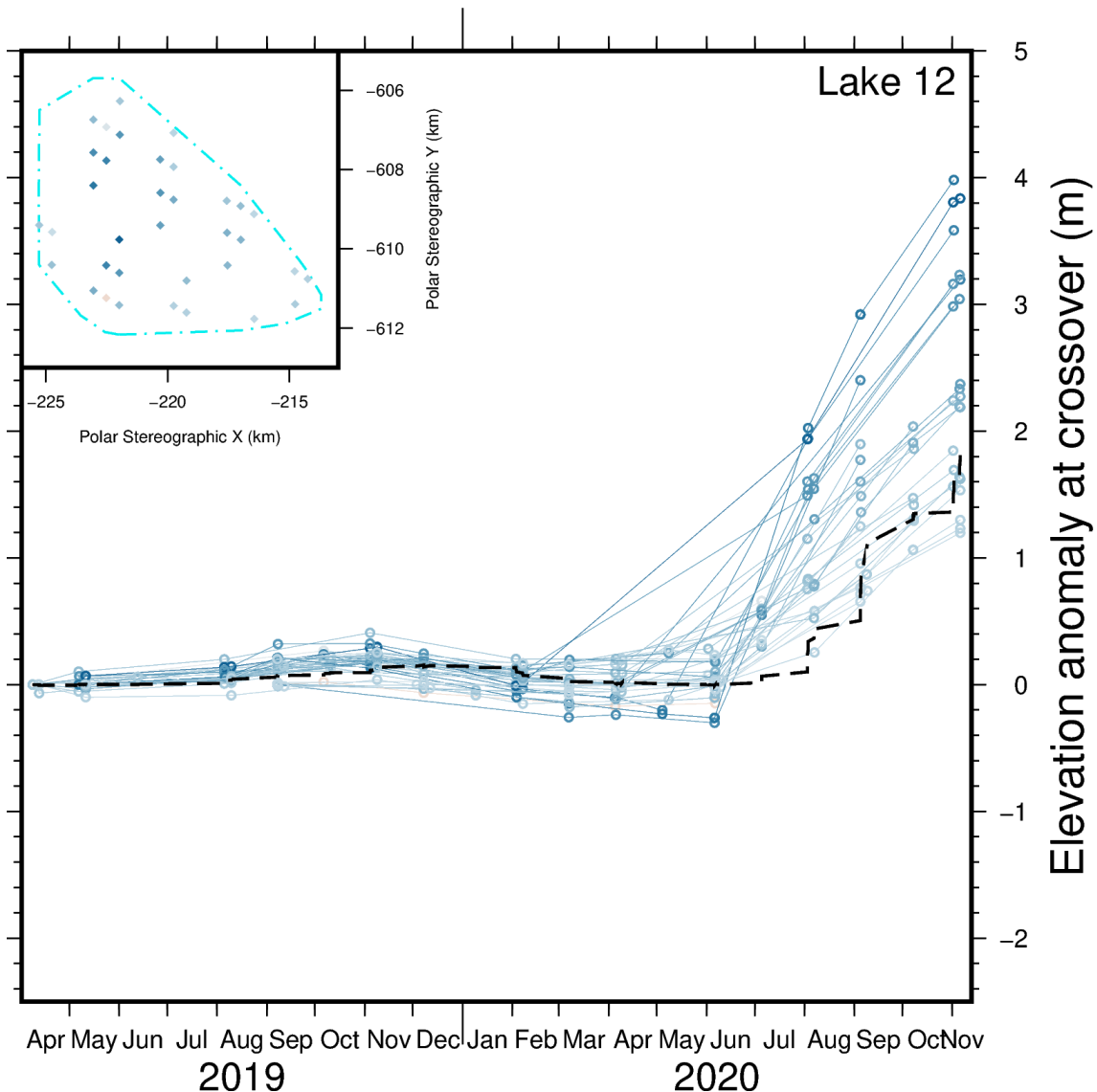


Figure 4.15: Elevation anomaly of crossover points within Lake 12. 91 day rolling mean of elevation anomalies shown as black dashed line. Inset plot shows locations of crossover points (blue) within lake outline (cyan).

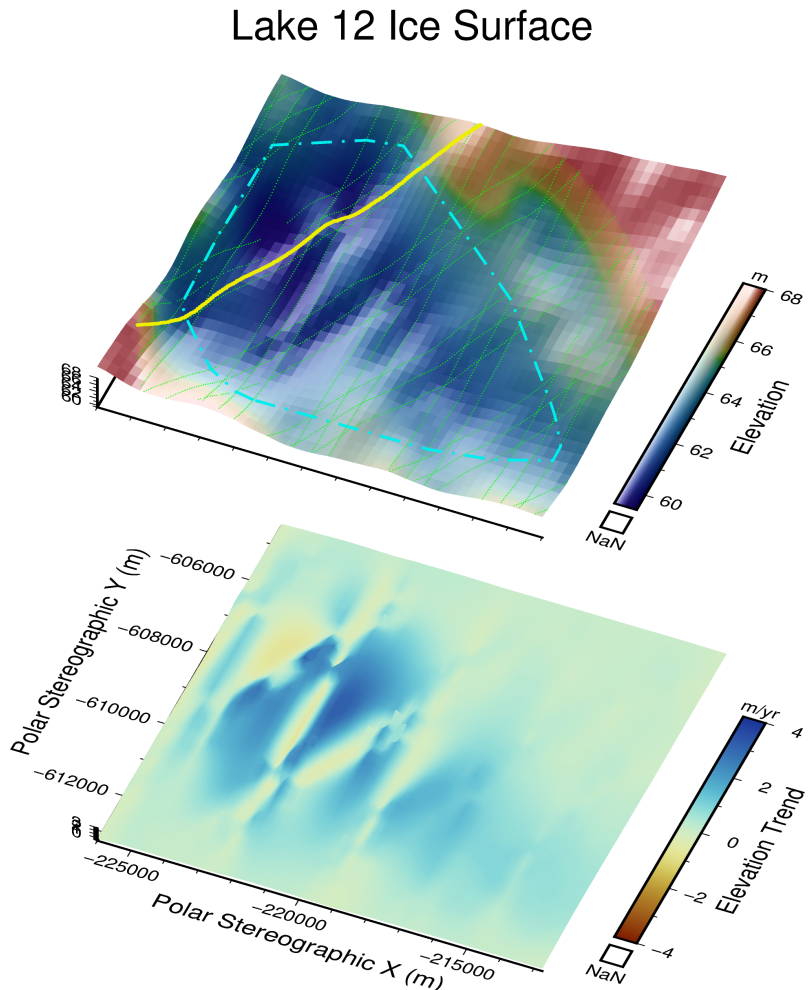


Figure 4.16: Top: Digital Surface Elevation Model at Lake 12 from interpolating the mean elevation measured by ICESat-2 over 2018-2020. Overlaid on top are ICESat-2 points (green), transect line in Fig. 4.17 (yellow) and lake outline (cyan). Bottom: Trend map of ice surface elevation change over time (dhdt).

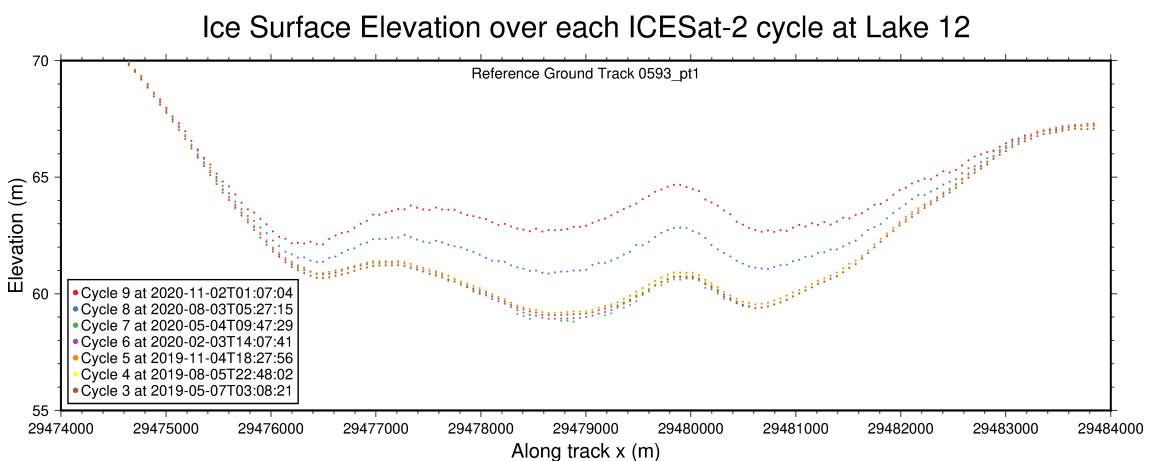


Figure 4.17: Along track view of ice surface elevation over Lake 12 from ICESat-2 Cycle 3 to Cycle 9. Ice surface elevation is changing by $\sim 4 \text{ m yr}^{-1}$ over a distance of $\sim 6 \text{ km}$ for this lake.

4.4 Discussion

4.4.1 Comparison to previous active subglacial lake studies

ICESat-2 classified Antarctic active subglacial lakes (Fig. 4.1) allow us to revisit previously studied lakes and observe new ones. As with the previous ICESat based inventory (B. E. Smith et al., 2009), most active subglacial lakes are located over West Antarctica (see Fig. 4.1), including significant clusters over the Institute Ice Stream and Foundation Ice Stream, as well as over Slessor Glacier and Recovery Glacier. No active subglacial lakes were detected over the Ellsworth Subglacial Highlands (c.f. Napoleoni et al., 2020) in this study, though this may be due to DB-SCAN parameters used in Sec. 4.2.4. Over Thwaites glacier, we observed drainage at Thw124 and filling at Thw170 in the 2018-2020 ICESat-2 laser altimetry data, matching those observed with Cryosat-2 radar altimetry (Malczyk et al., 2020; B. E. Smith et al., 2017) and Sentinel-1 SAR data (A. O. Hoffman et al., 2020). We primarily focus our study on the biggest cluster of active subglacial lakes over the Siple Coast (see Sec. 4.3.1.1, Sec. 4.4.2), building on the observations of Siegfried et al. (2016).

Active subglacial lakes were also observed over other parts of East Antarctica (Fig. 4.1). Significant clusters exist over Byrd Glacier (c.f. Wright et al., 2014) and David Glacier (c.f. Lindzey et al., 2020). Our ICESat-2 algorithm also detected surface uplift occurring at Lake Cook E2 (c.f. Y. Li et al., 2020) and surface lowering at Nimrod 2 (c.f. B. E. Smith et al., 2009). This ICESat-2 active subglacial lake inventory from 2018 to 2020 overlaps with many previously discovered lakes from the ICESat and Cryosat-2 missions (see Siegfried & Fricker, 2018; B. E. Smith et al., 2009), though the lake outlines can vary somewhat. Going forward, a systematic way of naming these dynamic lake features is needed as more subglacial lakes are discovered.

4.4.2 Multi-lobe active subglacial lakes

On the Siple Coast (Fig. 4.5) at Whillans 7 (Fig. 4.7), Subglacial Lake Whillans (Fig. 4.13) and Whillans IX (Fig. 4.10), we observed active subglacial lake clusters with multiple lobes closely spaced together, separated by ridge structures 1–4 km apart. These multi-cluster patterns of ice surface elevation change observed from precise ICESat-2 laser altimetry provide clues into subglacial water pathways and the subglacial geomorphology of the Antarctic ice sheet. From 2018-2020 at Subglacial Lake Whillans (Fig. 4.13) and Whillans IX (Fig. 4.10), there was a simultaneous filling up of water in multiple lobes straddling a relatively stable medial ridge with negligible surface elevation change. These stable medial ridges at Whillans Ice Stream are possibly surface expressions of subglacial ridges, and we can map the maximum width and minimum length of these features precisely using repeat ICESat-2 altimetry measurements. There are gaps of: ~ 4 km separating the Southern and Northern clusters of Subglacial Lake Whillans (Fig. 4.13); ~ 1 km separating clusters at Whillans 7 (Fig. 4.7); and ~ 1 km separating clusters at Whillans IX (Fig. 4.10). No maximum length can be determined however, so a length to width ratio for geomorphological classification of these ridges (Ely et al., 2016) would require further ground-based RES or active seismic surveys (e.g. Christianson et al., 2012; Horgan et al., 2012).

The pattern of filling and draining in distinct clusters of multi-lobe subglacial lake systems at Whillans Ice Stream occurred in tandem, albeit at different rates (Fig. 4.8, Fig. 4.11). This may be a subglacial distributary, with the subglacial water network branching off and causing differential inflow into the multi-lobe lakes. Alternatively, it could indicate the presence of a connected active subglacial water system straddling a permeable ridge-like structure, or that of a less permeable ridge-like seal breaking and healing over time, allowing for direct water movement across subglacial channels or canals (see Sec. 4.1.2.2). Similar lobe-like structures have been observed at the Whillans Southern catchment at Subglacial Lake Conway and Subglacial Lake Mercer where lake drainage occurred at the same time with Lower Subglacial Lake Conway and Lower Subglacial Lake Mercer respectively (Siegfried & Fricker, 2021), possibly occurring as a result of similar processes whereby subglacial ridge structures semi-separate each individual water store.

4.4.3 Cascading drain fill activity of Whillans subglacial lakes

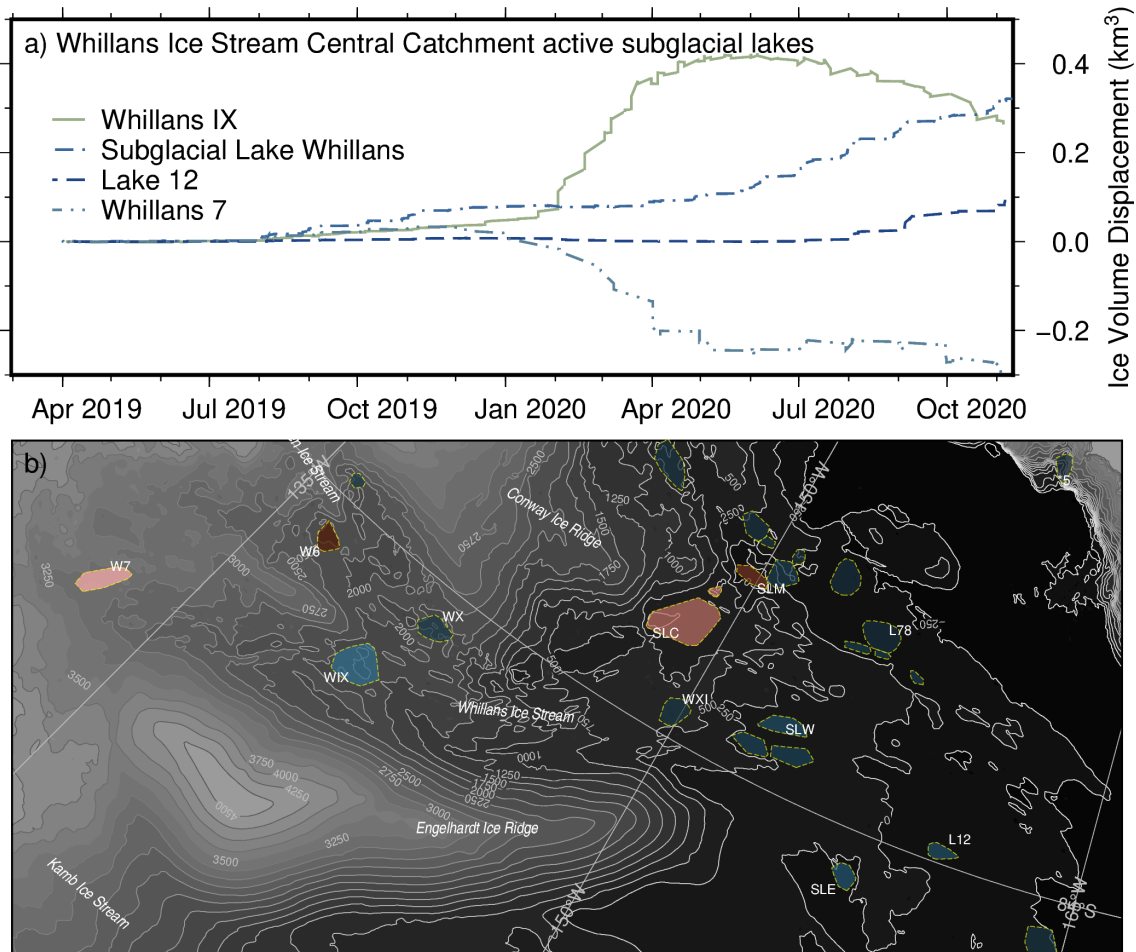


Figure 4.18: Active subglacial lakes over the Whillans Ice Stream Central Catchment. Ice flow direction is from left to right. a) Estimated ice volume displacement for: Whillans 7 (W7), Whillans IX (WIX), Subglacial Lake Whillans (SLW) and Lake 12 (L12). b) Hydropotential map of the study area with contours at 250 kPa intervals, overlaid with subglacial lake locations (red: draining, blue: filling).

4.4.3.1 Upstream drainage of Whillans 7 and Whillans IX

In Section 4.3.2, we showed a series of active subglacial lakes along the Whillans Ice Stream central basin undergoing localized ice surface elevation change from Whillans 7 (Fig. 4.6) to Lake 12 (Fig. 4.15). Using ice volume displacement time-series data (Sec. 4.2.5) and hydropotential maps (Appendix C), we detail a cascading pattern of lake drainage (see Fig. 4.18) similar to those observed at Recovery Glacier (Dow et al., 2018) and Thwaites Glacier (B. E. Smith et al., 2017). The drainage activity started from November 2019 at Whillans 7 (Fig. 4.6) with a maximum volume displacement of 0.3 km^3 , and this lake is likely the main source of basal water input to Subglacial Lake Whillans IX (Fig. 4.9) which experienced a volume increase of up to 0.4 km^3 from November 2019 to March 2020. The remaining 0.1 km^3 not accounted for by Whillans 7 could be sourced from draining lake Whillans 6 (W6) on the van der Veen Ice Stream that connects into Whillans Ice Stream's main trunk according to the hydropotential map (see Fig. 4.18b), though previously modelled subglacial water flux (Fig. 4.19, Carter et al., 2013; Le Brocq et al., 2009) indicated that Whillans 6 flows South into Subglacial Lake Conway. From April 2020 to November 2020, the ice volume of Whillans 7 decreased at a slower rate with a total drop in ice volume of about 0.1 km^3 , while Subglacial Lake Whillans IX experienced a greater drop in ice volume of about 0.2 km^3 over the same period.

4.4.3.2 Downstream filling of Subglacial Lake Whillans and Lake 12

Water that drained from the two upstream lakes induced localized uplifts further downstream (Fig. 4.18). The area around Subglacial Lake Whillans (Fig. 4.13, Tulaczyk et al., 2014) saw an elevation uplift from April to November 2020 in three distinct clusters (Fig. 4.12), corresponding to an increase in ice volume displacement of almost 0.4 km^3 . From there, the water appeared to have flowed into Subglacial Lake 12 (Fig. 4.15) which saw an increase in ice volume displacement of 0.1 km^3 from June to November 2020. Previous hydropotential maps for the ICESat time period (2003-2009, see Fig. 4.19, Carter et al., 2013) suggested that subglacial water at the Whillans central catchment flowed along a more Southern path closer to Lake 10 (Siegfried et al., 2016) and out to the ice shelf cavity via the Whillans Grounding Zone subglacial estuary (see Horgan et al., 2012). The ICESat-2 observations did not detect any significant elevation anomaly over Lake 10 (see Fig. 4.19, Fig. 4.18b, Fig. 4.5), and we suggest that a more Northern path via Lake 12 (Fig. 4.15) was taken instead over the course of 2020, indicating that flow re-routing may have occurred at the Whillans Ice Stream Central Catchment (c.f. Carter et al., 2013). Still, subglacial water flow could be occurring along the Southern route, just that no active subglacial lake activity was detected by the DBSCAN algorithm in Sec. 4.2.4.

4.4.3.3 Rate and periodicity of water output into the ocean

The high temporal resolution (< 3 months) data from our crossover analysis can reveal the timing and volume of subglacial water discharge. Filling events can be very rapid, with Whillans IX (Fig. 4.9) showing a maximum elevation change of $\sim 8 \text{ m}$ from December 2019 to March 2020, corresponding to an ice volume displacement of 0.4 km^3 (Fig. 4.18a) over 3 months. Conversely, drainage events can be slow and sustained, as in Whillans 7 (Fig. 4.6) with a maximum elevation change of $\sim -7 \text{ m}$ from Oct 2019 to November 2020, corresponding to an ice volume dis-

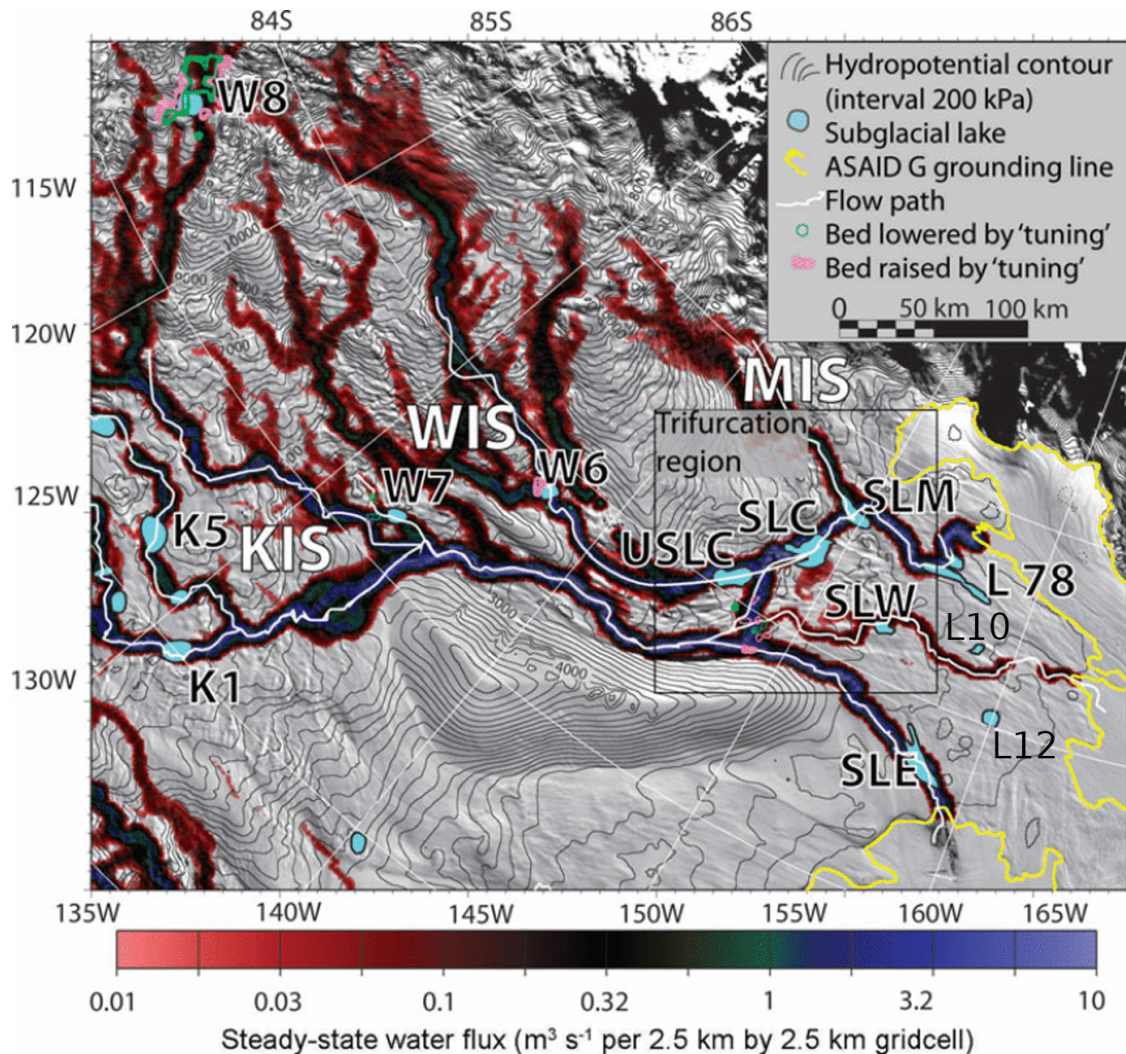


Figure 4.19: Modelled subglacial water flux (2003–2009) over Kamb (KIS), Whillans (WIS) and Mercer Ice Stream (MIS). Abbreviated lake names are: K1, K5: Kamb 1 and 5, W8, W7, W6: Whillans 8, 7, and 6; USLC: Upper Subglacial Lake Conway, SLC: Subglacial Lake Conway, SLM: Subglacial Lake Mercer, SLW: Subglacial Lake Whillans, SLE: Subglacial Lake Engelhardt, L78, L12, L10: Lake 78, 12, and 10. Flow direction is from left to right. Figure adapted from Carter et al. (2013).

placement of 0.3 km^3 (Fig. 4.18a) over 11 months. This unusual pattern of a rapid filling and slow drainage at Subglacial Lake Whillans IX (Fig. 4.9) and Whillans 7 (Fig. 4.6) stands in contrast to previous patterns of slow fill and rapid drainage in the Whillans catchment (e.g. Siegfried & Fricker, 2018; Siegfried et al., 2016). This 2019 subglacial lake drainage event is the 5th one observed along the Whillans Ice Stream central catchment since satellite observations started in 2003 (Siegfried & Fricker, 2018). Cryosat-2 observations from 2013 onwards appear to show more frequent fill-drain cycles over Subglacial Lake Whillans, with an event in 2014 (Siegfried et al., 2016), 2017 (Siegfried & Fricker, 2018), and now in 2019 (Fig. 4.12). This short residence time of water (2–3 yr) observed along the Whillans Ice Stream central catchment from 2013–2020 has implications for the biogeochemical cycling in the Southern Ocean which was previously inferred to be longer (years to decades) based on measurements at Subglacial Lake Mercer (Hawkings et al., 2020; Vick-Majors et al., 2020). Further repeat satellite altimeter measurements into the future (e.g. CRISTAL; Kern et al., 2020) will be needed to capture the periodicity of these trends.

4.4.4 Limitations

The clustering algorithm was ran on ICESat-2 ATL11 land ice time-series (B. E. Smith et al., 2021) points which have a lower data density (3 laser tracks) than the ATL06 land ice (B. E. Smith, Fricker, Gardner, Siegfried, et al., 2020) or raw ATL03 (Neumann et al., 2020) point cloud products (6 laser tracks). The tradeoff was made here on the basis of higher vertical accuracy and precision, rather than denser spatial coverage. This means that our active subglacial lake outlines loses $\sim 45 \text{ m}$ of horizontal precision (half the 90 m spacing of an ICESat-2 laser pair), compared to if the ATL06 product was used as in Siegfried and Fricker (2021). However, we note that determining active subglacial lake polygon areas here on the basis of vertical displacement may represent an overestimate of the true lake area owing to the complexity of vertical ice dynamic signals (c.f. Y. Li et al., 2020; Sergienko et al., 2007).

Furthermore, the elevation anomalies clusters may be due to other factors other than basal water volume changes (see Sec. 4.2.1). Sergienko et al. (2007) notes that basal traction variability is another potential source of ice surface elevation change, and argues that simultaneous analysis of surface velocity changes (e.g. Siegfried et al., 2016) is required to interpret the likely cause of change. Our classification of active subglacial lakes on the sole basis of vertical elevation change thus represents an upper estimate on inferred subglacial water volume changes. Integration of horizontal displacements from InSAR speckle-tracking, SAR offset-tracking or Optical feature-tracking (e.g. Gardner et al., 2018) is left to future work, and a challenge will be in sourcing year-round, cloud-free, satellite measurements that reach up to 88°S (currently only available with ICESat-2 and Cryosat-2).

4.5 Conclusions

This ICESat-2 (2018-) active subglacial lake time series extends that of the ICE-Sat (2003–2009) and ongoing Cryosat-2 (2010-) mission (Siegfried & Fricker, 2018). Using an unsupervised clustering method (DBSCAN), we identified localized ice

surface anomalies over the whole Antarctic continent that are likely caused by subglacial water movement. Along the central catchment of Whillans Ice Stream, we applied crossover track analysis to look at the temporal evolution of these elevation anomalies at short (< 3 month) timescales. A cascading pattern of subglacial lake drainage was observed, starting upstream at Whillans 7 from November 2019 and ending downstream at Lake 12 up to November 2020. Along this cascading drainage path, we detected several new active subglacial lakes, including one named Whillans IX at near the intersection of van der Veen Ice Stream and Whillans Ice Stream. Notably, the rapid rate of filling (~ 8 m of vertical displacement over 3 months) at Whillans IX has not been observed previously, and these observations of short water residence times have implications for biogeochemical cycling in the Siple Coast and Ross Ice Shelf area. Some active subglacial lakes also exhibited multi-lobe cluster patterns, which we infer to be an indication of subglacial ridges that have some form of subglacial water connectivity. A challenge remains in reconciling active subglacial lake outline classifications from different satellite sensors over time, while systematically naming the lakes in a standardized way as more lakes become discovered in the future.

Chapter 5

Conclusion

This thesis maps the subglacial world of Antarctica using satellite surface observations. A series of machine learning, inverse modelling and remote sensing methods were presented, utilizing high spatial resolution (≤ 250 m) datasets to investigate Antarctica's subglacial topography and hydrology, with implications for ice flow dynamics and future sea level projections. This section synthesizes the findings made in the context of our original research questions, highlights gaps remaining in both our observations and numerical models of subglacial Antarctica, and presents a path forward for future studies.

5.1 Research Questions

1. How can we integrate existing high spatial resolution remote sensing products to boost the resolution of existing bed elevation maps of Antarctica?

A deep neural network called DeepBedMap was designed to super-resolve the bed elevation of Antarctica (Leong & Horgan, 2020b), with the model architecture adapted from an Enhanced Super-Resolution Generative Adversarial Network (X. Wang et al., 2019). The DeepBedMap model is trained on areas in Antarctica where high-resolution (250 m) ground-truth bed elevation grid images are available, and then applied across the entire Antarctic continent. Inputs to the model are a prior low-resolution (1 km) BEDMAP2 image, and conditional remote sensing images of ice surface elevation, velocity and snow accumulation. Model training occurs via an iterative error minimization approach with a custom perceptual loss function that pushes the predicted images to be as close as possible to the ground-truth images. The model output is a four-times-upsampled super-resolution (250 m) bed elevation model of Antarctica called DeepBedMap_DEM that preserves detail in bed roughness and can be used for catchment- to continent-scale ice sheet modelling studies.

2. What effect does a rough surface, high-resolution (250 m) bed topography have on the friction parameters of an ice sheet model?

To examine the relative contributions of form drag and skin drag which opposes the driving stress of a glacier, a basal inversion experiment was performed on two different bed topographies - a rougher high-resolution (250 m) DeepBedMap_DEM (Leong & Horgan, 2020b) and a smoother medium-resolution (500 m) BedMachine Antarctica (Morlighem et al., 2019). The inversion was conducted via an iterative least-squares control method using the Ice-sheet and

Sea-level System Model (ISSM; Larour et al., 2012) with a Coulomb-limited Schoof-type sliding law. The inverted basal fields between DeepBedMap_DEM and BedMachine did not appear to be significantly different, though both basal drag and slipperiness fields are slightly higher while effective pressure is generally lower for the inversions that used the higher-resolution DeepBedMap_DEM. We did not observe a noticeable decrease in basal drag (i.e. less skin drag) when higher resolution topography (i.e. more form drag) was used, in contrast to previous studies using a Weertman-style sliding relation by Kyrke-Smith et al. (2018) who indicated that basal drag was reduced (i.e. less skin drag) when high resolution bed topography (i.e. more form drag) was incorporated into the model. Our findings in this chapter highlight that more ice sheet modelling research is needed over diverse subglacial settings in West Antarctica. Specifically, to investigate the role of subglacial hydrology which influences skin drag, and the effects of using high resolution bed topographies (≤ 100 m) which increases form drag.

3. Where does water drain and accumulate underneath the Antarctic Ice Sheet, how much volume is mobilized, and at what timescales do these processes occur?

A map of active subglacial lakes in Antarctica is presented, detected using ICESat-2 laser altimetry data over the 2018–2020 time period. Active subglacial lake locations were determined via an unsupervised density-based classification method on ICESat-2 point cloud data pre-processed to highlight anomalous ice surface elevation change rates. The algorithm yielded a total of 195 active subglacial lakes, including 36 new lakes in the 86–88°S area not detected by the previous ICESat (2003–2009) mission. We detailed a cascading pattern of drain-fill activity over the Whillans Ice Stream central basin at the Siple Coast, and revealed multi-lobe subglacial lake clusters separated by ridges using the high resolution (< 40 m along-track spacing) ICESat-2 laser altimetry data. An interesting observation was the unusually high rate of surface elevation uplift and slow descent at Subglacial Lake Whillans IX (~ 8 m vertical rise over 3 months) and Whillans 7 (~ -7 m lowering over 11 months) which stands in contrast with previous studies over the Whillans Ice Stream catchment area that tend to show slow fill and rapid drainage (Siegfried & Fricker, 2018; Siegfried et al., 2016).

5.2 Future work

Many advances in glaciology are driven by the availability of newer, high quality datasets combined with better, physical numerical models. In particular, highly parallel compute processors such as general purpose graphical processing units has opened up new possibilities around the use of neural network models on remote sensing data. Computational glaciology can greatly benefit from new machine learning tools that allow us to see and predict changes that were previously unattainable. One of the exciting ideas emerging from this work, is how measurement data collected at multiple scales (satellite, airborne, ground-based) can be integrated statistically and be used to infer high resolution data at unsurveyed sites, while providing the intelligence to suggest new sites where field measurements should go next. In the

following, we highlight data gaps to be filled, and missing components in our understanding of the physical mechanisms of ice flow over the subglacial terrain of Antarctica.

5.2.1 Towards BEDMAP3 - More data to super-resolve the bed topography of Antarctica

In Chapter 2, we indicated that there is missing coverage of bed elevation data in parts of Antarctica, and that Radio-echo sounding (RES) is the best tool available to fill in these gaps. Swath processing of RES data (e.g. Holschuh et al., 2020) should become a priority, and new acquisitions should target a diverse range of bed and flow types. Furthermore, we should continue to survey formerly glaciated beds around the margins of Antarctica using ship-based swath bathymetry instruments and on land in areas like the former Laurentide ice sheet using LIDAR. Continued measurements by remote sensing satellites is also needed to patch up data gaps in surface elevation, velocity and snow accumulation. All this new data will be used to inform the next generation bed topography model of Antarctica - BEDMAP3.

5.2.2 Coupling ice flow models with evolving subglacial hydrological models

In Chapter 3, our basal inversion experiment suggested that subglacial water which influences skin drag cannot be ruled out as an important factor that affects ice dynamics when using a high resolution bed. Hence, future modelling studies could include a coupling with an evolving subglacial hydrology model (e.g. Sommers et al., 2018) to better parametrize the effective pressure field in a Coulomb-limited sliding law. More prognostic forward model runs should be done on high resolution bed elevation models with a Schoof-type sliding law and Full Stokes (or higher order) stress balance equations to assess the potential effects of different basal traction and slipperiness fields on Antarctic grounding line migration and its resulting contribution to sea level rise.

5.2.3 Continuous active subglacial lake time-series data

In Chapter 4, we used the ICESat-2 laser altimeter to create an inventory of active subglacial lakes for a short time period from 2018-2020, but future work should extend the record both backwards in time to the ICESat era (2003-2009) and into the future such as with the CRISTAL radar altimeter mission (Kern et al., 2020). A priority for the remote sensing community will be to mitigate against any interruptions in the data record (such as between ICESat and Cryosat-2 previously), utilizing airborne geophysical surveys or GPS stations (such as with Operation IceBridge) if necessary on key sites to minimize loss of continuous coverage. One critical piece of work will lie in calibrating differences in elevation measurements across laser- and radar-based satellite altimeters (c.f. Siegfried & Fricker, 2018), for the currently operational ICESat-2 and Cryosat-2 (Brunt et al., 2020) and in the future as new satellite altimeters come online.

5.3 Concluding remark

The objective of this thesis were to 1) create a high-resolution (250 m) map of Antarctica's bed, 2) investigate how high-resolution bed topography affects basal friction, and 3) map out the active subglacial hydrological system of Antarctica. These are addressed using a series of novel machine learning and automated satellite remote sensing methods that use surface observations to infer the nature of Antarctica's subglacial topography and hydrology.

Appendix A

Details of loss function components

The loss function, or cost function, is a mathematical function that maps a set of input variables to an output loss value. The loss value can be thought of as a weighted sum of several error metrics between the neural network’s prediction and the expected output or ground truth. It is this loss value which we want to minimize so as to train the neural network model to perform better, and we do this by iteratively optimizing the parameters in the loss function. Following this are the details of the various loss functions that make up the total loss function of the DeepBedMap generative adversarial network model.

A.1 Content Loss

To bring the pixel values of the generated images closer to those of the ground truth, we first define the content-loss function L_1 . Following ESRGAN (X. Wang et al., 2019), we have

$$L_1 = \frac{1}{n} \sum_{i=1}^n \|\hat{y}_i - y_i\|_1 , \quad (\text{A.1})$$

where we take the mean absolute error between the generator network’s predicted value \hat{y}_i and the ground-truth value y_i , respectively, over every pixel i .

A.2 Adversarial Loss

Next, we define an adversarial loss to encourage the production of high-resolution images \hat{y} closer to the manifold of natural-looking digital-elevation-model images. To do so, we introduce the standard discriminator in the form of $D(y) = \sigma(C(y))$, where σ is the sigmoid activation function and $C(y)$ is the raw, non-transformed output from a discriminator neural network acting on high-resolution image y . The ESRGAN model (X. Wang et al., 2019), however, employs an improved relativistic-average discriminator (Jolicoeur-Martineau, 2018) denoted by D_{Ra} . It is defined as $D_{\text{Ra}}(y, \hat{y}) = \sigma(C(y) - \mathbb{E}_{\hat{y}}[C(\hat{y})])$, where $\mathbb{E}_{\hat{y}}[\cdot]$ is the arithmetic mean operation carried out over every generated image \hat{y} in a mini batch. We use a binary cross-entropy loss as the discriminator’s loss function defined as follows:

$$L_{\text{D}}^{\text{Ra}} = -\mathbb{E}_y[\ln(D(y, \hat{y}))] - \mathbb{E}_{\hat{y}}[\ln(1 - D(\hat{y}, y))]. \quad (\text{A.2})$$

The generator network's adversarial loss is in a symmetrical form:

$$L_G^{\text{Ra}} = -\mathbb{E}_y[\ln(1 - D(y, \hat{y}))] - \mathbb{E}_{\hat{y}}[\ln(D(\hat{y}, y))]. \quad (\text{A.3})$$

A.3 Topographic Loss

We further define a topographic loss so that the elevation values in the super-resolved image make topographic sense with respect to the original low-resolution image. Specifically, we want the mean value of each 4×4 grid on the predicted super-resolution (DeepBedMap) image to closely match its spatially corresponding $1 \text{ pixel} \times 1 \text{ pixel}$ area on the low-resolution (BEDMAP2) image.

First, we apply a 4×4 mean pooling operation on the generator network's predicted super-resolution image:

$$\bar{\hat{y}}_j = \frac{1}{n} \sum_{i=1}^n \hat{y}_i, \quad (\text{A.4})$$

where $\bar{\hat{y}}_j$ is the mean of all predicted values \hat{y}_i across the 16 super-resolved pixels i within a 4×4 grid corresponding to the spatial location of 1 low-resolution pixel at position j . Following this, we can compute the topographic loss as follows:

$$L_T = \frac{1}{m} \sum_{i=1}^m \|\bar{\hat{y}}_j - x_j\|_1, \quad (\text{A.5})$$

where we take the mean absolute error between the mean of the 4×4 super-resolved pixels calculated in Eq. (A.4) $\bar{\hat{y}}_j$ and those of the spatially corresponding low-resolution pixel x_j , respectively, over every low-resolution pixel j .

A.4 Structural Loss

Lastly, we define a structural loss that takes into account luminance, contrast and structural information between the predicted and ground-truth images. This is based on the structural similarity index (SSIM; Z. Wang et al., 2004) and is calculated over a single window patch as

$$\text{SSIM}(\hat{y}, y) = \frac{(2\mu_{\hat{y}}\mu_y + c_1)(2\sigma_{\hat{y}y} + c_2)}{(\mu_{\hat{y}}^2 + \mu_y^2 + c_1)(\sigma_{\hat{y}}^2 + \sigma_y^2 + c_2)}, \quad (\text{A.6})$$

where $\mu_{\hat{y}}$ and μ_y are the arithmetic mean of predicted image \hat{y} and ground-truth image y , respectively, over a single window that we set to 9 pixels \times 9 pixels; $\sigma_{\hat{y}y}$ is the covariance of \hat{y} and y ; $\sigma_{\hat{y}}^2$ and σ_y^2 are the variances of \hat{y} and y , respectively; and c_1 and c_2 are two variables set to 0.01^2 and 0.03^2 to stabilize division with a weak denominator. Thus, we can formulate the structural loss as follows:

$$L_S = 1 - \frac{1}{p} \sum_{i=1}^p \text{SSIM}(\hat{y}, y)_p, \quad (\text{A.7})$$

where we take 1 minus the mean of all structural similarity values $\text{SSIM}(\hat{y}, y)$ calculated over every patch p obtained via a sliding window over the predicted image \hat{y} and ground-truth image y .

A.5 Total Loss Function

Finally, we compile the loss functions for the discriminator and generator networks as follows:

$$L_D = L_D^{\text{Ra}}, \quad (\text{A.8})$$

$$L_G = \eta L_1 + \lambda L_G^{\text{Ra}} + \theta L_T + \zeta L_S, \quad (\text{A.9})$$

where η , λ , θ and ζ are the scaled weights for the content L_1 , adversarial L_D , topographic L_T and structural losses L_S , respectively (see Table B.1 for values used). The loss functions L_D and L_G are minimized in an alternate 1 : 1 manner so as to solve the entire generative adversarial network's objective function defined in Eq. (2.4).

Appendix B

Neural Network Training Details

The neural networks were developed using Chainer v7.0.0 (Tokui et al., 2019) and trained using full-precision (floating point 32) arithmetic. Experiments were carried out on four graphical processing units (GPUs), specifically two Tesla P100 GPUs and two Tesla V100 GPUs. On the Tesla V100 GPU setup, one training run with about 150 epochs takes about 30 min. This is using a batch size of 128 on a total of 3826 training image tiles, with 202 tiles reserved for validation, i.e. a 95/5 training/validation split. We next describe the method used to evaluate each DeepBedMap candidate model, as well as the high-level way in which we semi-automatically arrived at a good model via semi-automatic hyperparameter tuning.

To check for overfitting, we evaluate the generative adversarial network model using the validation dataset after each epoch using two performance metrics – a peak signal-to-noise ratio (PSNR) metric for the generator and an accuracy metric for the discriminator. Training stops when these validation performance metrics show little improvement, roughly at 140 epochs.

Next, we conduct a full evaluation on an independent test dataset, comparing the model’s predicted grid output with actual ground-truth *xyz* points. Using the “grdtrack” function in Generic Mapping Tools v6.0 (Wessel et al., 2019), we obtain the grid elevation at each ground-truth point and use it to calculate the elevation error on a point-to-point basis. All of these elevation errors are then used to compute a root mean square error (RMSE) statistic over this independent test site. This

Table B.1: Optimized hyperparameter settings.

Hyperparameter	Setting	Tuning range
Learning rate (for both generator and discriminator)	1.7×10^{-4}	2×10^{-4} to 1×10^{-4}
Number of residual-in-residual blocks	12	8 to 14
Mini-batch size	128	64 or 128
Number of epochs	140	90 to 150
Residual scaling	0.2	0.1 to 0.5
Content-loss weighting η	1×10^{-2}	Fixed
Adversarial-loss weighting λ	2×10^{-2}	Fixed
Topographic-loss weighting θ	2×10^{-3}	Fixed
Structural-loss weighting ζ	5.25	Fixed
He normal initialization scaling	0.1	Fixed
Adam optimizer epsilon	0.1	Fixed
Adam optimizer beta1	0.9	Fixed
Adam optimizer beta2	0.99	Fixed

RMSE value is used to judge the model’s performance in relation to baseline bicubic interpolation and is also the metric minimized by a hyperparameter optimization algorithm which we will describe next.

Neural networks contain a lot of hyperparameter settings that need to be decided upon, and generative adversarial networks are particularly sensitive to different hyperparameter settings. To stabilize model training and obtain better performance, we tune the hyperparameters (see Table B.1) using a Bayesian approach. Specifically, we employ the Tree-structured Parzen Estimator (Bergstra et al., 2011) from the Optuna v2.0.0 (Akiba et al., 2019) library with default settings as per the Hyperopt library (Bergstra et al., 2015). Given that we have four GPUs, we choose to parallelize the hyperparameter tuning experiments asynchronously between all four devices. The estimator first conducts 20 random experimental trials to scan the hyperparameter space, gradually narrowing down its range to a few candidate hyperparameters in subsequent experiments. We set each GPU to run a target of 60 experimental trials (i.e. a total of 240), though unpromising trials that have exploding or vanishing gradients are pruned prematurely using the Hyperband algorithm (L. Li et al., 2018) to save on time and computational resources. The top models from these experiments undergo further visual evaluation, and we continue to conduct further experiments until a suitable candidate model is found.

Appendix C

Hydropotential

Hydropotential (or hydrostatic pressure) refers to the static energy of water available at a particular time and place. It is a function of the amount of pressure exerted on a water body, located at a particular elevation relative to a reference datum. By calculating hydropotential over a spatial surface, we can then derive the hydropotential gradients which provides us with a measure of the direction and tendency of water to flow if suitable conduits exist in its path. Following the methods of Shreve (1972), basal hydropotential ϕ is calculated as follows:

$$\phi = \phi_0 + p_w + \rho_w g z_b \quad (\text{C.1})$$

where ϕ denotes hydropotential at the base of the ice, ϕ_0 is an arbitrary constant, p_w is water pressure and $\rho_w g z_b$ is the elevation potential term. The elevation potential term is made up of the density of water ρ_w multiplied by the gravitational acceleration term g multiplied by the bed elevation z_b . In most cases, subglacial water pressure p_w can be approximated as the pressure induced by the overlying ice (overburden pressure):

$$p_w = \rho_i * g * (z_s - z_b) \quad (\text{C.2})$$

where the static water pressure p_w is equal to the density of ice ρ_i multiplied by the gravitational acceleration term g multiplied by the thickness of ice $z_s - z_b$ obtained from the ice surface elevation z_s minus the ice bed elevation z_b . Using a gravitational acceleration g of 9.8 m s^{-2} , ice density ρ_i of 917 kg m^{-3} , and water density ρ_w of 1000 kg m^{-3} , we can substitute Equation (C.2) into (C.1) to obtain the following equation:

$$\phi = 813.4 \left(\frac{917}{83} * z_s + z_b \right) \quad (\text{C.3})$$

where the ice surface elevation z_s is about $\frac{917}{83} = 11.05$ times more important than bed surface elevation z_b for its effect on hydropotential ϕ . This is an oft-cited constant, and varies across the literature from as low as 8 to as high as 11 depending on what densities of water ρ_w and ice ρ_i are used in the calculation.

Bibliography

- Aitken, A. R. A., Young, D. A., Ferraccioli, F., Betts, P. G., Greenbaum, J. S., Richter, T. G., Roberts, J. L., Blankenship, D. D., & Siegert, M. J. (2014). The subglacial geology of Wilkes Land, East Antarctica. *Geophysical Research Letters*, 41(7), 2390–2400. <https://doi.org/10.1002/2014GL059405> (cit. on p. 42)
- Akiba, T., Sano, S., Yanase, T., Ohta, T., & Koyama, M. (2019–August 8). Optuna: A Next-generation Hyperparameter Optimization Framework. *Proceedings of the 25th ACM SIGKDD International Conference on Knowledge Discovery & Data Mining - KDD '19*, 2623–2631. <https://doi.org/10.1145/3292500.3330701> (cit. on p. 108)
- Alley, R. B. (1989). Water-Pressure Coupling of Sliding and Bed Deformation: I. Water System. *Journal of Glaciology*, 35(119), 108–118. <https://doi.org/10.3189/002214389793701527> (cit. on p. 71)
- Arnold, N. S., Conway, S. J., Butcher, F. E. G., & Balme, M. R. (2019). Modeled Subglacial Water Flow Routing Supports Localized Intrusive Heating as a Possible Cause of Basal Melting of Mars' South Polar Ice Cap. *Journal of Geophysical Research: Planets*, 124(8), 2101–2116. <https://doi.org/10.1029/2019JE006061> (cit. on p. 18)
- Arthern, R. J., Winebrenner, D. P., & Vaughan, D. G. (2006). Antarctic snow accumulation mapped using polarization of 4.3-cm wavelength microwave emission. *Journal of Geophysical Research*, 111(D6), D06107. <https://doi.org/10.1029/2004JD005667> (cit. on pp. 30, 31, 43, 44, 75)
- Attema, E., Davidson, M., Snoeij, P., Rommen, B., & Flouri, N. (2009). Sentinel-1 mission overview. *2009 IEEE International Geoscience and Remote Sensing Symposium*, I-36-I-39. <https://doi.org/10.1109/IGARSS.2009.5416921> (cit. on p. 18)
- Barber, C. B., Dobkin, D. P., & Huhdanpaa, H. (1996). The quickhull algorithm for convex hulls. *ACM Transactions on Mathematical Software*, 22(4), 469–483. <https://doi.org/10.1145/235815.235821> (cit. on p. 80)
- Bell, R. E., Ferraccioli, F., Creyts, T. T., Braaten, D., Corr, H., Das, I., Damaske, D., Frearson, N., Jordan, T., Rose, K., Studinger, M., & Wolovick, M. (2011). Widespread Persistent Thickening of the East Antarctic Ice Sheet by Freezing from the Base. *Science*, 331(6024), 1592–1595. <https://doi.org/10.1126/science.1200109> (cit. on p. 76)
- Bell, R. E., Banwell, A. F., Trusel, L. D., & Kingslake, J. (2018). Antarctic surface hydrology and impacts on ice-sheet mass balance. *Nature Climate Change*, 8(12), 1044–1052. <https://doi.org/10.1038/s41558-018-0326-3> (cit. on p. 71)
- Bell, R. E., Studinger, M., Shuman, C. A., Fahnestock, M. A., & Joughin, I. (2007). Large subglacial lakes in East Antarctica at the onset of fast-flowing ice

- streams. *Nature*, 445(7130), 904–907. <https://doi.org/10.1038/nature05554> (cit. on pp. 22, 69, 73)
- Bergstra, J., Bardenet, R., Bengio, Y., & Kégl, B. (2011–December 17). Algorithms for Hyper-parameter Optimization. *Proceedings of the 24th International Conference on Neural Information Processing Systems*, 24, 2546–2554. Retrieved April 16, 2019, from <http://dl.acm.org/citation.cfm?id=2986459.2986743> (cit. on p. 108)
- Bergstra, J., Komor, B., Eliasmith, C., Yamins, D., & Cox, D. D. (2015). Hyperopt: A Python library for model selection and hyperparameter optimization. *Computational Science & Discovery*, 8(1), 014008. <https://doi.org/10.1088/1749-4699/8/1/014008> (cit. on p. 108)
- Bindschadler, R., Choi, H., Wichlacz, A., Bingham, R., Bohlander, J., Brunt, K., Corr, H., Drews, R., Fricker, H., Hall, M., Hindmarsh, R., Kohler, J., Padman, L., Rack, W., Rotschky, G., Urbini, S., Vornberger, P., & Young, N. (2011). Getting around Antarctica: New high-resolution mappings of the grounded and freely-floating boundaries of the Antarctic ice sheet created for the International Polar Year. *The Cryosphere*, 5(3), 569–588. <https://doi.org/10.5194/tc-5-569-2011> (cit. on p. 34)
- Bingham, R. G., Vaughan, D. G., King, E. C., Davies, D., Cornford, S. L., Smith, A. M., Arthern, R. J., Brisbourne, A. M., De Rydt, J., Graham, A. G. C., Spagnolo, M., Marsh, O. J., & Shean, D. E. (2017). Diverse landscapes beneath Pine Island Glacier influence ice flow. *Nature Communications*, 8(1), 1618. <https://doi.org/10.1038/s41467-017-01597-y> (cit. on pp. 20, 26, 29, 41, 44, 48, 52, 64)
- Blau, Y., Mechrez, R., Timofte, R., Michaeli, T., & Zelnik-Manor, L. (2018, September 20). *2018 PIRM Challenge on Perceptual Image Super-resolution*. arXiv: 1809.07517 [cs]. Retrieved December 30, 2018, from <https://arxiv.org/abs/1809.07517v2>. (Cit. on p. 28)
- Bougamont, M., Tulaczyk, S. M., & Joughin, I. (2003). Numerical investigations of the slow-down of Whillans Ice Stream, West Antarctica: Is it shutting down like Ice Stream C? *Annals of Glaciology*, 37, 239–246. <https://doi.org/10.3189/172756403781815555> (cit. on p. 71)
- Boulton, G. S. (1976). The Origin of Glacially Fluted Surfaces-Observations and Theory. *Journal of Glaciology*, 17(76), 287–309. <https://doi.org/10.3189/S002214300013605> (cit. on p. 72)
- Brondex, J., Gagliardini, O., Gillet-Chaulet, F., & Durand, G. (2017). Sensitivity of grounding line dynamics to the choice of the friction law. *Journal of Glaciology*, 63(241), 854–866. <https://doi.org/10.1017/jog.2017.51> (cit. on pp. 51, 53)
- Brondex, J., Gillet-Chaulet, F., & Gagliardini, O. (2019). Sensitivity of centennial mass loss projections of the Amundsen basin to the friction law. *The Cryosphere*, 13(1), 177–195. <https://doi.org/10.5194/tc-13-177-2019> (cit. on pp. 51, 53)
- Brunt, K. M., Neumann, T. A., & Smith, B. E. (2019). Assessment of ICESat-2 Ice Sheet Surface Heights, Based on Comparisons Over the Interior of the Antarctic Ice Sheet. *Geophysical Research Letters*, 46(22), 13072–13078. <https://doi.org/10.1029/2019GL084886> (cit. on p. 77)
- Brunt, K. M., Smith, B. E., Sutterley, T. C., Kurtz, N. T., & Neumann, T. A. (2020). Comparisons of Satellite and Airborne Altimetry with Ground-Based Data

- from the Interior of the Antarctic Ice Sheet. *Geophysical Research Letters*. <https://doi.org/10.1029/2020GL090572> (cit. on p. 101)
- Budd, W. F., Keage, P. L., & Blundy, N. A. (1979). Empirical Studies of Ice Sliding. *Journal of Glaciology*, 23(89), 157–170. <https://doi.org/10.3189/S0022143000029804> (cit. on pp. 51, 64)
- Bulat, S. A., Marie, D., & Petit, J.-R. (2012). Prospects for life in the subglacial Lake Vostok. *Ice and Snow*, 52(4). Retrieved December 7, 2020, from <https://www.elibrary.ru/item.asp?id=18286425> (cit. on p. 71)
- Bulat, S. A. (2016). Microbiology of the subglacial Lake Vostok: First results of borehole-frozen lake water analysis and prospects for searching for lake inhabitants. *Philosophical Transactions of the Royal Society A: Mathematical, Physical and Engineering Sciences*, 374(2059), 20140292. <https://doi.org/10.1098/rsta.2014.0292> (cit. on p. 71)
- Bulat, S. A., Alekhina, I. A., Blot, M., Petit, J.-R., de Angelis, M., Wagenbach, D., Lipenkov, V. Y., Vasilyeva, L. P., Wloch, D. M., Raynaud, D., & Lukin, V. V. (2004). DNA signature of thermophilic bacteria from the aged accretion ice of Lake Vostok, Antarctica: Implications for searching for life in extreme icy environments. *International Journal of Astrobiology*, 3(1), 1–12. <https://doi.org/10.1017/S1473550404001879> (cit. on p. 71)
- Bulthuis, K., Arnst, M., Sun, S., & Pattyn, F. (2019). Uncertainty quantification of the multi-centennial response of the Antarctic ice sheet to climate change. *The Cryosphere*, 13(4), 1349–1380. <https://doi.org/10.5194/tc-13-1349-2019> (cit. on pp. 47, 51)
- Burton-Johnson, A., Dziadek, R., & Martin, C. (2020). Review article: Geothermal heat flow in Antarctica: Current and future directions. *The Cryosphere*, 14(11), 3843–3873. <https://doi.org/10.5194/tc-14-3843-2020> (cit. on p. 71)
- Carter, S. P., Blankenship, D. D., Peters, M. E., Young, D. A., Holt, J. W., & Morse, D. L. (2007). Radar-based subglacial lake classification in Antarctica. *Geochemistry, Geophysics, Geosystems*, 8(3), n/a–n/a. <https://doi.org/10.1029/2006GC001408> (cit. on pp. 69, 70)
- Carter, S. P., Fricker, H., & Siegfried, M. R. (2013). Evidence of rapid subglacial water piracy under Whillans Ice Stream, West Antarctica. *Journal of Glaciology*, 59(218), 1147–1162. <https://doi.org/10.3189/2013JoG13J085> (cit. on pp. 94, 95)
- Carter, S. P., Fricker, H. A., & Siegfried, M. R. (2017). Antarctic subglacial lakes drain through sediment-floored canals: Theory and model testing on real and idealized domains. *The Cryosphere*, 11(1), 381–405. <https://doi.org/10.5194/tc-11-381-2017> (cit. on pp. 70, 76)
- Chen, Z., Wang, X., Xu, Z., & Hou, W. (2016). Convolutional Neural Network Based Dem Super Resolution. *International Archives of the Photogrammetry, Remote Sensing and Spatial Information Sciences*, XLI-B3, 247–250. <https://doi.org/10.5194/isprsarchives-XLI-B3-247-2016> (cit. on p. 29)
- Christianson, K., Jacobel, R. W., Horgan, H. J., Anandakrishnan, S., & Alley, R. B. (2012). Subglacial Lake Whillans — Ice-penetrating radar and GPS observations of a shallow active reservoir beneath a West Antarctic ice stream. *Earth and Planetary Science Letters*, 331–332, 237–245. <https://doi.org/10.1016/j.epsl.2012.03.013> (cit. on pp. 70, 92)
- Christner, B. C., Priscu, J. C., Achberger, A. M., Barbante, C., Carter, S. P., Christianson, K., Michaud, A. B., Mikucki, J. A., Mitchell, A. C., Skidmore, M. L.,

- Vick-Majors, T. J., & the WISSARD Science Team. (2014). A microbial ecosystem beneath the West Antarctic ice sheet. *Nature*, 512(7514), 310–313. <https://doi.org/10.1038/nature13667> (cit. on p. 71)
- Clarke, G. K. C., Berthier, E., Schoof, C. G., & Jarosch, A. H. (2009). Neural Networks Applied to Estimating Subglacial Topography and Glacier Volume. *Journal of Climate*, 22(8), 2146–2160. <https://doi.org/10.1175/2008JCLI2572.1> (cit. on p. 27)
- Cogley, J. G., Hock, R., Rasmussen, L. A., Arendt, A. A., Bauder, A., Braithwaite, R. J., Jansson, P., Kaser, G., Möller, M., Nicholson, L., & Zemp, M. (2011). *Glossary of glacier mass balance and related terms, IHP-VII technical documents in hydrology No. 86, IACS Contribution No. 2*. UNESCO-IHP. <http://unesdoc.unesco.org/images/0019/001925/192525e.pdf>. (Cit. on pp. 74, 76)
- Cornford, S. L., Martin, D. F., Lee, V., Payne, A. J., & Ng, E. G. (2016). Adaptive mesh refinement versus subgrid friction interpolation in simulations of Antarctic ice dynamics. *Annals of Glaciology*, 57(73), 1–9. <https://doi.org/10.1017/aog.2016.13> (cit. on pp. 26, 48)
- Cornford, S. L., Seroussi, H., Asay-Davis, X. S., Gudmundsson, G. H., Arthern, R., Borstad, C., Christmann, J., Dias dos Santos, T., Feldmann, J., Goldberg, D., Hoffman, M. J., Humbert, A., Kleiner, T., Leguy, G., Lipscomb, W. H., Merino, N., Durand, G., Morlighem, M., Pollard, D., ... Yu, H. (2020). Results of the third Marine Ice Sheet Model Intercomparison Project (MISMIP+). *The Cryosphere*, 14(7), 2283–2301. <https://doi.org/10.5194/tc-14-2283-2020> (cit. on p. 51)
- Cox, S. C., Smith-Lytte, B., Siddoway, C., Capponi, G., Elvevold, S., Burton-Johnson, A., Halpin, J., Morin, P., Elliot, D., & Geomap Action Group. (2018–June 23). The GeoMAP dataset of Antarctic rock exposures. *POLAR2018*, 2428 (cit. on p. 42).
- Crameri, F. (2018, December 10). Scientific colour maps. <https://doi.org/10.5281/zenodo.1243862>. (Cit. on p. 68)
- Cuffey, K., & Paterson, W. S. B. (2010). *The physics of glaciers* (4th ed). Butterworth-Heinemann/Elsevier. (Cit. on pp. 19, 47, 53, 74)
OCLC: ocn488732494.
- Cui, X., Jeofry, H., Greenbaum, J. S., Guo, J., Li, L., Lindzey, L. E., Habbal, F. A., Wei, W., Young, D. A., Ross, N., Morlighem, M., Jong, L. M., Roberts, J. L., Blankenship, D. D., Bo, S., & Siegert, M. J. (2020). Bed topography of Princess Elizabeth Land in East Antarctica. *Earth System Science Data*, 12(4), 2765–2774. <https://doi.org/10.5194/essd-12-2765-2020> (cit. on pp. 20, 21)
- Culberg, R., & Schroeder, D. M. (2020). Firn Clutter Constraints on the Design and Performance of Orbital Radar Ice Sounders. *IEEE Transactions on Geoscience and Remote Sensing*, 58(9), 6344–6361. <https://doi.org/10.1109/TGRS.2020.2976666> (cit. on p. 18)
- Dai, J., Qi, H., Xiong, Y., Li, Y., Zhang, G., Hu, H., & Wei, Y. (2017, March 17). *Deformable Convolutional Networks*. arXiv: 1703.06211 [cs]. Retrieved September 6, 2019, from <http://arxiv.org/abs/1703.06211>. (Cit. on p. 33)
- De Fleurian, B., Werder, M. A., Beyer, S., Brinkerhoff, D. J., Delaney, I., Dow, C. F., Downs, J., Gagliardini, O., Hoffman, M. J., Hooke, R. L., Seguinot, J., & Sommers, A. N. (2018). SHMIP The subglacial hydrology model intercom-

- parison Project. *Journal of Glaciology*, 64(248), 897–916. <https://doi.org/10.1017/jog.2018.78> (cit. on p. 22)
- Depoorter, M. A., Bamber, J. L., Griggs, J. A., Lenaerts, J. T. M., Ligtenberg, S. R. M., van den Broeke, M. R., & Moholdt, G. (2013). *Antarctic masks (ice-shelves, ice-sheet, and islands), link to shape file*. PANGAEA - Data Publisher for Earth & Environmental Science. <https://doi.org/10.1594/PANGAEA.819147>. (Cit. on pp. 68, 82)
- Diez, A., Matsuoka, K., Ferraccioli, F., Jordan, T. A., Corr, H. F., Kohler, J., Olesen, A. V., & Forsberg, R. (2018). Basal Settings Control Fast Ice Flow in the Recovery/Slessor/Bailey Region, East Antarctica. *Geophysical Research Letters*, 45(6), 2706–2715. <https://doi.org/10.1002/2017GL076601> (cit. on p. 73)
- Dirsscherl, M., Dietz, A. J., Kneisel, C., & Kuenzer, C. (2020). Automated Mapping of Antarctic Supraglacial Lakes Using a Machine Learning Approach. *Remote Sensing*, 12(7), 1203. <https://doi.org/10.3390/rs12071203> (cit. on pp. 22, 71)
- Dong, C., Loy, C. C., He, K., & Tang, X. (2014, December 31). *Image Super-Resolution Using Deep Convolutional Networks*. arXiv: 1501.00092 [cs]. Retrieved March 9, 2018, from <http://arxiv.org/abs/1501.00092>. (Cit. on p. 27)
- Dow, C. F., Werder, M. A., Babonis, G., Nowicki, S., Walker, R. T., Csatho, B., & Morlighem, M. (2018). Dynamics of Active Subglacial Lakes in Recovery Ice Stream. *Journal of Geophysical Research: Earth Surface*, 123(4), 837–850. <https://doi.org/10.1002/2017JF004409> (cit. on p. 94)
- Dowdeswell, J. A., Canals, M., Jakobsson, M., Todd, B. J., Dowdeswell, E. K., & Hogan, K. A. (2016). The variety and distribution of submarine glacial landforms and implications for ice-sheet reconstruction. *Geological Society, London, Memoirs*, 46(1), 519–552. <https://doi.org/10.1144/M46.183> (cit. on p. 40)
- Dowdeswell, J. A., Solheim, A., & Ottesen, D. (2016). Rhombohedral crevasse-fill ridges at the marine margin of a surging Svalbard ice cap. *Geological Society, London, Memoirs*, 46(1), 73–74. <https://doi.org/10.1144/M46.62> (cit. on p. 40)
- Drews, R., Pattyn, F., Hewitt, I. J., Ng, F. S. L., Berger, S., Matsuoka, K., Helm, V., Bergeot, N., Favier, L., & Neckel, N. (2017). Actively evolving subglacial conduits and eskers initiate ice shelf channels at an Antarctic grounding line. *Nature Communications*, 8(1), 15228. <https://doi.org/10.1038/ncomms15228> (cit. on p. 40)
- Drusch, M., Del Bello, U., Carlier, S., Colin, O., Fernandez, V., Gascon, F., Hoersch, B., Isola, C., Laberinti, P., Martimort, P., Meygret, A., Spoto, F., Sy, O., Marchese, F., & Bargellini, P. (2012). Sentinel-2: ESA's Optical High-Resolution Mission for GMES Operational Services. *Remote Sensing of Environment*, 120, 25–36. <https://doi.org/10.1016/j.rse.2011.11.026> (cit. on p. 18)
- Dumoulin, V., Perez, E., Schucher, N., Strub, F., Vries, H., Courville, A., & Bengio, Y. (2018). Feature-wise transformations. *Distill*, 3(7), e11. <https://doi.org/10.23915/distill.00011> (cit. on p. 28)

- Durand, G., Gagliardini, O., Favier, L., Zwinger, T., & le Meur, E. (2011). Impact of bedrock description on modeling ice sheet dynamics. *Geophysical Research Letters*, 38(20). <https://doi.org/10.1029/2011GL048892> (cit. on pp. 26, 48)
- Ely, J. C., Clark, C. D., Spagnolo, M., Stokes, C. R., Greenwood, S. L., Hughes, A. L., Dunlop, P., & Hess, D. (2016). Do subglacial bedforms comprise a size and shape continuum? *Geomorphology*, 257, 108–119. <https://doi.org/10.1016/j.geomorph.2016.01.001> (cit. on pp. 72, 92)
- Falcini, F. A., Rippin, D. M., Krabbendam, M., & Selby, K. A. (2018). Quantifying bed roughness beneath contemporary and palaeo-ice streams. *Journal of Glaciology*, 64 (247), 822–834. <https://doi.org/10.1017/jog.2018.71> (cit. on pp. 20, 26)
- Farinotti, D., Brinkerhoff, D. J., Clarke, G. K. C., Fürst, J. J., Frey, H., Gantayat, P., Gillet-Chaulet, F., Girard, C., Huss, M., Leclercq, P. W., Linsbauer, A., Machguth, H., Martin, C., Maussion, F., Morlighem, M., Mosbeux, C., Pandit, A., Portmann, A., Rabatel, A., ... Andreassen, L. M. (2017). How accurate are estimates of glacier ice thickness? Results from ITMIX, the Ice Thickness Models Intercomparison eXperiment. *The Cryosphere*, 11(2), 949–970. <https://doi.org/10.5194/tc-11-949-2017> (cit. on p. 26)
- Farinotti, D., Huss, M., Bauder, A., Funk, M., & Truffer, M. (2009). A method to estimate the ice volume and ice-thickness distribution of alpine glaciers. *Journal of Glaciology*, 55(191), 422–430. <https://doi.org/10.3189/002214309788816759> (cit. on p. 26)
- Farinotti, D., Huss, M., Fürst, J. J., Landmann, J., Machguth, H., Maussion, F., & Pandit, A. (2019). A consensus estimate for the ice thickness distribution of all glaciers on Earth. *Nature Geoscience*, 12(3), 168–173. <https://doi.org/10.1038/s41561-019-0300-3> (cit. on p. 26)
- Ferraccioli, F., Corr, H., Jordan, T. A., Robinson, C., Armadillo, E., Bozzo, E., & Caneva, G. (2018, April 3). *Airborne radar bed elevation picks across the Wilkes Subglacial Basin, 2005-2006*. Polar Data Centre, Natural Environment Research Council, UK. <https://doi.org/10.5285/59e5a6f5-e67d-4a05-99af-30f656569401>. (Cit. on p. 44)
- Fisher, A. T., Mankoff, K. D., Tulaczyk, S. M., Tyler, S. W., Foley, N., & and the WISSARD Science Team. (2015). High geothermal heat flux measured below the West Antarctic Ice Sheet. *Science Advances*, 1(6), e1500093. <https://doi.org/10.1126/sciadv.1500093> (cit. on p. 71)
- Flament, T., Berthier, E., & Rémy, F. (2014). Cascading water underneath Wilkes Land, East Antarctic ice sheet, observed using altimetry and digital elevation models. *The Cryosphere*, 8(2), 673–687. <https://doi.org/10.5194/tc-8-673-2014> (cit. on p. 70)
- Flament, T., & Rémy, F. (2012). Dynamic thinning of Antarctic glaciers from along-track repeat radar altimetry. *Journal of Glaciology*, 58(211), 830–840. <https://doi.org/10.3189/2012JoG11J118> (cit. on p. 76)
- Flowers, G. E. (2015). Modelling water flow under glaciers and ice sheets. *Proceedings of the Royal Society A: Mathematical, Physical and Engineering Sciences*, 471(2176), 20140907–20140907. <https://doi.org/10.1098/rspa.2014.0907> (cit. on pp. 71, 72)
- Fretwell, P., Pritchard, H. D., Vaughan, D. G., Bamber, J. L., Barrand, N. E., Bell, R., Bianchi, C., Bingham, R. G., Blankenship, D. D., Casassa, G., Catania, G., Callens, D., Conway, H., Cook, A. J., Corr, H. F. J., Damaske, D., Damm,

- V., Ferraccioli, F., Forsberg, R., ... Zirizzotti, A. (2013). Bedmap2: Improved ice bed, surface and thickness datasets for Antarctica. *The Cryosphere*, 7(1), 375–393. <https://doi.org/10.5194/tc-7-375-2013> (cit. on pp. 20, 26, 27, 30, 31, 34, 35, 41, 42, 44, 48, 52, 64)
- Fricker, H. A., Scambos, T. A., Bindschadler, R., & Padman, L. (2007). An Active Subglacial Water System in West Antarctica Mapped from Space. *Science*, 315(5818), 1544–1548. <https://doi.org/10.1126/science.1136897> (cit. on pp. 69, 80)
- Fricker, H. A., & Scambos, T. (2009). Connected subglacial lake activity on lower Mercer and Whillans Ice Streams, West Antarctica, 2003–2008. *Journal of Glaciology*, 55(190), 303–315. <https://doi.org/10.3189/002214309788608813> (cit. on p. 83)
- Fricker, H. A., Scambos, T., Carter, S., Davis, C., Haran, T., & Joughin, I. (2010). Synthesizing multiple remote-sensing techniques for subglacial hydrologic mapping: Application to a lake system beneath MacAyeal Ice Stream, West Antarctica. *Journal of Glaciology*, 56(196), 187–199. <https://doi.org/10.3189/002214310791968557> (cit. on p. 83)
- Fricker, H. A., Siegfried, M. R., Carter, S. P., & Scambos, T. A. (2016). A decade of progress in observing and modelling Antarctic subglacial water systems. *Philosophical Transactions of the Royal Society A: Mathematical, Physical and Engineering Sciences*, 374(2059), 20140294. <https://doi.org/10.1098/rsta.2014.0294> (cit. on pp. 73, 77)
- Fukushima, K., & Miyake, S. (1982). Neocognitron: A new algorithm for pattern recognition tolerant of deformations and shifts in position. *Pattern Recognition*, 15(6), 455–469. [https://doi.org/10.1016/0031-3203\(82\)90024-3](https://doi.org/10.1016/0031-3203(82)90024-3) (cit. on p. 27)
- Gagliardini, O., Cohen, D., Råback, P., & Zwinger, T. (2007). Finite-element modeling of subglacial cavities and related friction law. *Journal of Geophysical Research*, 112(F2). <https://doi.org/10.1029/2006JF000576> (cit. on pp. 53, 64)
- Gardner, A. S., Moholdt, G., Scambos, T., Fahnestock, M., Ligtenberg, S., van den Broeke, M., & Nilsson, J. (2018). Increased West Antarctic and unchanged East Antarctic ice discharge over the last 7 years. *The Cryosphere*, 12(2), 521–547. <https://doi.org/10.5194/tc-12-521-2018> (cit. on p. 96)
- GEBCO Bathymetric Compilation Group 2020. (2020). *The GEBCO_2020 Grid - a continuous terrain model of the global oceans and land.* (Version 1). British Oceanographic Data Centre, National Oceanography Centre, NERC, UK. <https://doi.org/10.5285/A29C5465-B138-234D-E053-6C86ABC040B9>. (Cit. on p. 34)
- Gillet-Chaulet, F., Durand, G., Gagliardini, O., Olivier, Mosbeux, C., Mouginot, J., Jeremie, Rémy, F., & Ritz, C. (2016). Assimilation of surface velocities acquired between 1996 and 2010 to constrain the form of the basal friction law under Pine Island Glacier. *Geophysical Research Letters*, 43(19), 10, 311–10, 321. <https://doi.org/10.1002/2016GL069937> (cit. on p. 50)
- Glasser, N. F., & Gudmundsson, G. H. (2012). Longitudinal surface structures (flow-stripes) on Antarctic glaciers. *The Cryosphere*, 6(2), 383–391. <https://doi.org/10.5194/tc-6-383-2012> (cit. on p. 40)

- Glen, J. W. (1955). The creep of polycrystalline ice. *Proceedings of the Royal Society of London. Series A. Mathematical and Physical Sciences*, 228(1175), 519–538. <https://doi.org/10.1098/rspa.1955.0066> (cit. on p. 53)
- Goff, J. A., Powell, E. M., Young, D. A., & Blankenship, D. D. (2014). Conditional simulation of Thwaites Glacier (Antarctica) bed topography for flow models: Incorporating inhomogeneous statistics and channelized morphology. *Journal of Glaciology*, 60(222), 635–646. <https://doi.org/10.3189/2014JoG13J200> (cit. on pp. 26, 48, 49)
- Gogineni, P., Simpson, C. R., Yan, J.-B., O'Neill, C. R., Sood, R., Gurbuz, S. Z., & Gurbuz, A. C. (2018). A CubeSat Train for Radar Sounding and Imaging of Antarctic Ice Sheet. *IGARSS 2018 - 2018 IEEE International Geoscience and Remote Sensing Symposium*, 4138–4141. <https://doi.org/10.1109/IGARSS.2018.8519162> (cit. on p. 18)
- Goodfellow, I. J., Bengio, Y., & Courville, A. (2016). *Deep learning*. The MIT Press. <http://www.deeplearningbook.org>. (Cit. on p. 20)
- Goodfellow, I. J., Pouget-Abadie, J., Mirza, M., Xu, B., Warde-Farley, D., Ozair, S., Courville, A., & Bengio, Y. (2014, June 10). *Generative Adversarial Networks*. arXiv: 1406.2661 [cs, stat]. Retrieved March 12, 2019, from <http://arxiv.org/abs/1406.2661>. (Cit. on pp. 20, 28, 31, 32)
- Gorman, M. R., & Siegert, M. J. (1999). Penetration of Antarctic subglacial lakes by VHF electromagnetic pulses: Information on the depth and electrical conductivity of basal water bodies. *Journal of Geophysical Research: Solid Earth*, 104(B12), 29311–29320. <https://doi.org/10.1029/1999JB900271> (cit. on p. 70)
- Graham, F. S., Roberts, J. L., Galton-Fenzi, B. K., Young, D., Blankenship, D., & Siegert, M. J. (2017). A high-resolution synthetic bed elevation grid of the Antarctic continent. *Earth System Science Data*, 9(1), 267–279. <https://doi.org/10.5194/essd-9-267-2017> (cit. on pp. 26, 48, 49, 64, 65)
- Gray, L. (2005). Evidence for subglacial water transport in the West Antarctic Ice Sheet through three-dimensional satellite radar interferometry. *Geophysical Research Letters*, 32(3). <https://doi.org/10.1029/2004GL021387> (cit. on p. 69)
- Gudmundsson, G. H. (2003). Transmission of basal variability to a glacier surface. *Journal of Geophysical Research: Solid Earth*, 108(B5). <https://doi.org/10.1029/2002JB002107> (cit. on p. 76)
- Gudmundsson, G. H. (2011). Inverse Methods in Glaciology. In V. P. Singh, P. Singh, & U. K. Haritashya (Eds.), *Encyclopedia of Snow, Ice and Glaciers* (pp. 653–656). Springer Netherlands. https://doi.org/10.1007/978-90-481-2642-2_648. (Cit. on p. 20)
- Haran, T., Bohlander, J., Scambos, T. A., Painter, T., & Fahnestock, M. (2014). MODIS Mosaic of Antarctica 2008-2009 (MOA2009) Image Map. <https://doi.org/10.7265/N5KP8037>. (Cit. on p. 68)
- Hättestrand, C. (1997). Ribbed moraines in Sweden — distribution pattern and palaeoglaciological implications. *Sedimentary Geology*, 111(1-4), 41–56. [https://doi.org/10.1016/S0037-0738\(97\)00005-5](https://doi.org/10.1016/S0037-0738(97)00005-5) (cit. on p. 40)
- Hättestrand, C., & Kleman, J. (1999). Ribbed moraine formation. *Quaternary Science Reviews*, 18(1), 43–61. [https://doi.org/10.1016/S0277-3791\(97\)00094-2](https://doi.org/10.1016/S0277-3791(97)00094-2) (cit. on p. 40)

- Hawkins, J. R., Skidmore, M. L., Wadham, J. L., Priscu, J. C., Morton, P. L., Hatton, J. E., Gardner, C. B., Kohler, T. J., Stibal, M., Bagshaw, E. A., Steigmeyer, A., Barker, J., Dore, J. E., Lyons, W. B., Tranter, M., Spencer, R. G. M., & the SALSA Science Team. (2020). Enhanced trace element mobilization by Earth's ice sheets. *Proceedings of the National Academy of Sciences*, 202014378. <https://doi.org/10.1073/pnas.2014378117> (cit. on p. 96)
- He, K., Zhang, X., Ren, S., & Sun, J. (2015, December 10). *Deep Residual Learning for Image Recognition*. arXiv: 1512.03385 [cs]. Retrieved January 29, 2018, from <http://arxiv.org/abs/1512.03385>. (Cit. on p. 28)
- He, K., Zhang, X., Ren, S., & Sun, J. (2016, July 25). *Identity Mappings in Deep Residual Networks*. arXiv: 1603.05027 [cs]. Retrieved April 15, 2020, from <http://arxiv.org/abs/1603.05027>. (Cit. on p. 33)
- Helm, V., Humbert, A., & Miller, H. (2014). Elevation and elevation change of Greenland and Antarctica derived from CryoSat-2. *The Cryosphere*, 8(4), 1539–1559. <https://doi.org/10.5194/tc-8-1539-2014> (cit. on p. 43)
- Helsen, M. M., van den Broeke, M. R., van de Wal, R. S. W., van de Berg, W. J., van Meijgaard, E., Davis, C. H., Li, Y., & Goodwin, I. (2008). Elevation Changes in Antarctica Mainly Determined by Accumulation Variability. *Science*, 320(5883), 1626–1629. <https://doi.org/10.1126/science.1153894> (cit. on p. 76)
- Herron, M. M., & Langway, C. C. (1980). Firn Densification: An Empirical Model. *Journal of Glaciology*, 25(93), 373–385. <https://doi.org/10.3189/S0022143000015239> (cit. on p. 75)
- Hindmarsh, R. C. A. (1998). Drumlinization and drumlin-forming instabilities: Viscous till mechanisms. *Journal of Glaciology*, 44(147), 293–314. <https://doi.org/10.3189/S00221430000263X> (cit. on p. 72)
- Hindmarsh, R. C. A. (2004). A numerical comparison of approximations to the Stokes equations used in ice sheet and glacier modeling. *Journal of Geophysical Research: Earth Surface*, 109(F1). <https://doi.org/10.1029/2003JF000065> (cit. on pp. 49, 53)
- Hochmuth, K., Gohl, K., Leitchenkov, G., Sauermilch, I., Whittaker, J. M., Uenzelmann-Neben, G., Davy, B., & De Santis, L. (2020). The Evolving Paleobathymetry of the Circum-Antarctic Southern Ocean Since 34 Ma: A Key to Understanding Past Cryosphere-Ocean Developments. *Geochemistry, Geophysics, Geosystems*, 21(8). <https://doi.org/10.1029/2020GC009122> (cit. on p. 19)
- Hoffman, A. O., Christianson, K., Shapero, D., Smith, B. E., & Joughin, I. (2020, April 9). *Brief Communication: Heterogenous thinning and subglacial lake activity on Thwaites Glacier, West Antarctica*. *Glaciers/Subglacial Processes*. <https://doi.org/10.5194/tc-2020-80>. (Cit. on pp. 73, 92)
- Hoffman, M., & Price, S. (2014). Feedbacks between coupled subglacial hydrology and glacier dynamics. *Journal of Geophysical Research: Earth Surface*, 119(3), 414–436. <https://doi.org/10.1002/2013JF002943> (cit. on p. 71)
- Holschuh, N., Christianson, K., Paden, J., Alley, R. B., & Anandakrishnan, S. (2020). Linking postglacial landscapes to glacier dynamics using swath radar at Thwaites Glacier, Antarctica. *Geology*, 48(3), 268–272. <https://doi.org/10.1130/G46772.1> (cit. on pp. 19, 41, 42, 72, 101)
- Hooke, R. L., Laumann, T., & Kohler, J. (1990). Subglacial Water Pressures and the Shape of Subglacial Conduits. *Journal of Glaciology*, 36(122), 67–71. <https://doi.org/10.3189/S002214300005566> (cit. on p. 72)

- Horgan, H. J., Anandakrishnan, S., Jacobel, R. W., Christianson, K., Alley, R. B., Heeszel, D. S., Picotti, S., & Walter, J. I. (2012). Subglacial Lake Whillans — Seismic observations of a shallow active reservoir beneath a West Antarctic ice stream. *Earth and Planetary Science Letters*, 331-332, 201–209. <https://doi.org/10.1016/j.epsl.2012.02.023> (cit. on pp. 71, 92, 94)
- Howat, I. M., Paul, M., Claire, P., & Myong-Jong, N. (2018). *The Reference Elevation Model of Antarctica*. Harvard Dataverse. <https://doi.org/10.7910/DVN/SAIK8B>. (Cit. on pp. 30, 44)
- Howat, I. M., Porter, C., Smith, B. E., Noh, M.-J., & Morin, P. (2019). The Reference Elevation Model of Antarctica. *The Cryosphere*, 13(2), 665–674. <https://doi.org/10.5194/tc-13-665-2019> (cit. on pp. 19, 31, 40, 41, 43, 54, 77)
- Hubbard, B., Siegert, M. J., & McCarroll, D. (2000). Spectral roughness of glaciated bedrock geomorphic surfaces: Implications for glacier sliding. *Journal of Geophysical Research: Solid Earth*, 105(B9), 21295–21303. <https://doi.org/10.1029/2000JB900162> (cit. on p. 20)
- Iken, A., Röthlisberger, H., Flotron, A., & Haeberli, W. (1983). The Uplift of Unter-aargletscher at the Beginning of the Melt Season—A Consequence of Water Storage at the Bed? *Journal of Glaciology*, 29(101), 28–47. <https://doi.org/10.3189/S002214300005128> (cit. on pp. 19, 22, 73)
- Iken, A. (1981). The Effect of the Subglacial Water Pressure on the Sliding Velocity of a Glacier in an Idealized Numerical Model. *Journal of Glaciology*, 27(97), 407–421. <https://doi.org/10.3189/S0022143000011448> (cit. on p. 53)
- IMBIE. (2018). Mass balance of the Antarctic Ice Sheet from 1992 to 2017. *Nature*, 558(7709), 219–222. <https://doi.org/10.1038/s41586-018-0179-y> (cit. on p. 26)
- Ioffe, S., & Szegedy, C. (2015, March 2). *Batch Normalization: Accelerating Deep Network Training by Reducing Internal Covariate Shift*. arXiv: 1502.03167 [cs]. Retrieved January 15, 2020, from <http://arxiv.org/abs/1502.03167>. (Cit. on p. 34)
- IPCC. (2019). Summary for Policymakers. In H.-O. Pörtner, D. C. Roberts, V. Masson-Delmotte, P. Zhai, M. Tignor, E. Poloczanska, K. Mintenbeck, A. Alegría, M. Nicolai, A. Okem, J. Petzold, B. Rama, & N. M. Weyer (Eds.), *IPCC Special Report on the Ocean and Cryosphere in a Changing Climate*. Retrieved January 16, 2020, from <https://www.ipcc.ch/srocc/chapter/summary-for-policymakers/>. (Cit. on p. 17)
- Isola, P., Zhu, J.-Y., Zhou, T., & Efros, A. A. (2016, November 21). *Image-to-Image Translation with Conditional Adversarial Networks*. arXiv: 1611.07004 [cs]. Retrieved March 12, 2019, from <http://arxiv.org/abs/1611.07004>. (Cit. on p. 28)
- Iverson, N. R., Hooyer, T. S., & Baker, R. W. (1998). Ring-shear studies of till deformation: Coulomb-plastic behavior and distributed strain in glacier beds. *Journal of Glaciology*, 44(148), 634–642. <https://doi.org/10.3189/S0022143000002136> (cit. on p. 53)
- Iverson, N. R., & Zoet, L. K. (2015). Experiments on the dynamics and sedimentary products of glacier slip. *Geomorphology*, 244, 121–134. <https://doi.org/10.1016/j.geomorph.2015.03.027> (cit. on pp. 20, 48, 49)
- Jeofry, H., Ross, N., Corr, H. F. J., Li, J., Morlighem, M., Gogineni, P., & Siegert, M. J. (2018). A new bed elevation model for the Weddell Sea sector of the

- West Antarctic Ice Sheet. *Earth System Science Data*, 10(2), 711–725. <https://doi.org/10.5194/essd-10-711-2018> (cit. on p. 20)
- Jeofry, H., Ross, N., Corr, H. F., Li, J., Gogineni, P., & Siegert, M. J. (2017, September 25). *1-km bed topography digital elevation model (DEM) of the Weddell Sea sector, West Antarctica*. Zenodo. <https://doi.org/10.5281/zenodo.1035488>. (Cit. on p. 42)
- Jolicoeur-Martineau, A. (2018, July 2). *The relativistic discriminator: A key element missing from standard GAN*. arXiv: 1807.00734 [cs, stat]. Retrieved January 2, 2019, from <https://arxiv.org/abs/1807.00734>. (Cit. on p. 103)
- Jordan, T. A., Ferraccioli, F., Corr, H., Graham, A., Armadillo, E., & Bozzo, E. (2010). Hypothesis for mega-outburst flooding from a palaeo-subglacial lake beneath the East Antarctic Ice Sheet: Antarctic palaeo-outburst floods and subglacial lake. *Terra Nova*, 22(4), 283–289. <https://doi.org/10.1111/j.1365-3121.2010.00944.x> (cit. on p. 29)
- Joughin, I., Smith, B. E., & Schoof, C. G. (2019). Regularized Coulomb Friction Laws for Ice Sheet Sliding: Application to Pine Island Glacier, Antarctica. *Geophysical Research Letters*, 46(9), 4764–4771. <https://doi.org/10.1029/2019GL082526> (cit. on pp. 50–52, 64)
- Joughin, I., Tulaczyk, S. M., Bamber, J. L., Blankenship, D., Holt, J. W., Scambos, T., & Vaughan, D. G. (2009). Basal conditions for Pine Island and Thwaites Glaciers, West Antarctica, determined using satellite and airborne data. *Journal of Glaciology*, 55(190), 245–257. <https://doi.org/10.3189/002214309788608705> (cit. on pp. 41, 48, 51)
- Kern, M., Cullen, R., Berruti, B., Bouffard, J., Casal, T., Drinkwater, M. R., Gabriele, A., Lecuyot, A., Ludwig, M., Midthassel, R., Navas Traver, I., Parrinello, T., Ressler, G., Andersson, E., Martin-Puig, C., Andersen, O., Bartsch, A., Farrell, S., Fleury, S., ... Yackel, J. (2020). The Copernicus Polar Ice and Snow Topography Altimeter (CRISTAL) high-priority candidate mission. *The Cryosphere*, 14(7), 2235–2251. <https://doi.org/10.5194/tc-14-2235-2020> (cit. on pp. 43, 96, 101)
- Kim, B.-H., Lee, C.-K., Seo, K.-W., Lee, W. S., & Scambos, T. A. (2016). Active subglacial lakes and channelized water flow beneath the Kamb Ice Stream. *The Cryosphere*, 10(6), 2971–2980. <https://doi.org/10.5194/tc-10-2971-2016> (cit. on pp. 70, 80, 81, 83)
- King, E. C. (2011). Ice stream or not? Radio-echo sounding of Carlson Inlet, West Antarctica. *The Cryosphere*, 5(4), 907–916. <https://doi.org/10.5194/tc-5-907-2011> (cit. on pp. 29, 44)
- King, E. C., Pritchard, H. D., & Smith, A. M. (2016). Subglacial landforms beneath Rutford Ice Stream, Antarctica: Detailed bed topography from ice-penetrating radar. *Earth System Science Data*, 8(1), 151–158. <https://doi.org/10.5194/essd-8-151-2016> (cit. on pp. 29, 44, 72)
- Kingslake, J., Ely, J. C., Das, I., & Bell, R. E. (2017). Widespread movement of meltwater onto and across Antarctic ice shelves. *Nature*, 544(7650), 349–352. <https://doi.org/10.1038/nature22049> (cit. on p. 71)
- Krizhevsky, A., Sutskever, I., & Hinton, G. E. (2012). ImageNet Classification with Deep Convolutional Neural Networks. In F. Pereira, C. J. C. Burges, L. Bottou, & K. Q. Weinberger (Eds.), *Advances in Neural Information Processing Systems 25* (pp. 1097–1105). Curran Associates, Inc. Retrieved July 18, 2018,

- from <http://papers.nips.cc/paper/4824-imagenet-classification-with-deep-convolutional-neural-networks.pdf>. (Cit. on p. 27)
- Kyrke-Smith, T. M., Gudmundsson, G. H., & Farrell, P. E. (2018). Relevance of Detail in Basal Topography for Basal Slipperiness Inversions: A Case Study on Pine Island Glacier, Antarctica. *Frontiers in Earth Science*, 6, 33. <https://doi.org/10.3389/feart.2018.00033> (cit. on pp. 19, 20, 41, 48, 52, 64, 65, 100)
- Landerer, F. W., Flechtner, F. M., Save, H., Webb, F. H., Bandikova, T., Bertiger, W. I., Bettadpur, S. V., Byun, S. H., Dahle, C., Dobslaw, H., Fahnestock, E., Harvey, N., Kang, Z., Kruizinga, G. L. H., Loomis, B. D., McCullough, C., Murböck, M., Nagel, P., Paik, M., ... Yuan, D.-N. (2020). Extending the Global Mass Change Data Record: GRACE Follow-On Instrument and Science Data Performance. *Geophysical Research Letters*, 47(12). <https://doi.org/10.1029/2020GL088306> (cit. on p. 18)
- Larour, E., Seroussi, H., Morlighem, M., & Rignot, E. (2012). Continental scale, high order, high spatial resolution, ice sheet modeling using the Ice Sheet System Model (ISSM). *Journal of Geophysical Research: Earth Surface*, 117(F1). <https://doi.org/10.1029/2011JF002140> (cit. on pp. 20, 52–54, 100)
- Lauro, S. E., Pettinelli, E., Caprarelli, G., Guallini, L., Rossi, A. P., Mattei, E., Cosciotti, B., Cicchetti, A., Soldovieri, F., Cartacci, M., Di Paolo, F., Noschese, R., & Orosei, R. (2020). Multiple subglacial water bodies below the south pole of Mars unveiled by new MARSIS data. *Nature Astronomy*. <https://doi.org/10.1038/s41550-020-1200-6> (cit. on p. 18)
- Le Brocq, A. M., Payne, A. J., & Vieli, A. (2010). An improved Antarctic dataset for high resolution numerical ice sheet models (ALBMAP v1). *Earth System Science Data*, 2(2), 247–260. <https://doi.org/10.5194/essd-2-247-2010> (cit. on pp. 26, 55)
- Le Brocq, A., Payne, A., Siegert, M., & Alley, R. B. (2009). A subglacial water-flow model for West Antarctica. *Journal of Glaciology*, 55(193), 879–888. <https://doi.org/10.3189/002214309790152564> (cit. on p. 94)
- LeCun, Y., Boser, B., Denker, J. S., Henderson, D., Howard, R. E., Hubbard, W., & Jackel, L. D. (1989). Backpropagation Applied to Handwritten Zip Code Recognition. *Neural Computation*, 1(4), 541–551. <https://doi.org/10.1162/neco.1989.1.4.541> (cit. on p. 27)
- Lecun, Y., Bottou, L., Bengio, Y., & Haffner, P. (1998). Gradient-based learning applied to document recognition. *Proceedings of the IEEE*, 86(11), 2278–2324. <https://doi.org/10.1109/5.726791> (cit. on p. 27)
- LeCun, Y., Bengio, Y., & Hinton, G. (2015). Deep learning. *Nature*, 521(7553), 436–444. <https://doi.org/10.1038/nature14539> (cit. on p. 27)
- Ledig, C., Theis, L., Huszar, F., Caballero, J., Cunningham, A., Acosta, A., Aitken, A., Tejani, A., Totz, J., Wang, Z., & Shi, W. (2017–July 26). Photo-Realistic Single Image Super-Resolution Using a Generative Adversarial Network. *2017 IEEE Conference on Computer Vision and Pattern Recognition (CVPR)*, 105–114. <https://doi.org/10.1109/CVPR.2017.19> (cit. on p. 28)
- Leong, W. J., & Horgan, H. J. (2019). DeepBedMap: A super-resolution deep neural network for resolving the bed topography of Antarctica. https://www.igsoc.org/symposia/2019/stanford/proceedings/procfiles/procabstracts_75.html#A3032 (cit. on p. 49)

- Leong, W. J., & Horgan, H. J. (2020a, November 6). *DeepBedMap* (Version v1.1.0). <https://doi.org/10.5281/ZENODO.4054246>. (Cit. on pp. 44, 48, 49, 56, 59, 64)
- Leong, W. J., & Horgan, H. J. (2020b). DeepBedMap: A deep neural network for resolving the bed topography of Antarctica. *The Cryosphere*, 14(11), 3687–3705. <https://doi.org/10.5194/tc-14-3687-2020> (cit. on pp. 19–21, 48, 99)
- Li, L., Jamieson, K., DeSalvo, G., Rostamizadeh, A., & Talwalkar, A. (2018, June 18). *Hyperband: A Novel Bandit-Based Approach to Hyperparameter Optimization*. arXiv: 1603.06560 [cs, stat]. Retrieved July 30, 2020, from <http://arxiv.org/abs/1603.06560>. (Cit. on p. 108)
- Li, T., Dawson, G. J., Chuter, S. J., & Bamber, J. L. (2020). Mapping the grounding zone of Larsen C Ice Shelf, Antarctica, from ICESat-2 laser altimetry. *The Cryosphere*, 14(11), 3629–3643. <https://doi.org/10.5194/tc-14-3629-2020> (cit. on p. 81)
- Li, Y., Lu, Y., & Siegert, M. J. (2020). Radar Sounding Confirms a Hydrologically Active Deep-Water Subglacial Lake in East Antarctica. *Frontiers in Earth Science*, 8. <https://doi.org/10.3389/feart.2020.00294> (cit. on pp. 70, 92, 96)
- Ligtenberg, S. R. M., Helsen, M. M., & van den Broeke, M. R. (2011). An improved semi-empirical model for the densification of Antarctic firn. *The Cryosphere*, 5(4), 809–819. <https://doi.org/10.5194/tc-5-809-2011> (cit. on p. 76)
- Ligtenberg, S. R. M., Horwath, M., van den Broeke, M. R., & Legrésy, B. (2012). Quantifying the seasonal "breathing" of the Antarctic ice sheet. *Geophysical Research Letters*, 39(23). <https://doi.org/10.1029/2012GL053628> (cit. on p. 75)
- Lim, B., Son, S., Kim, H., Nah, S., & Lee, K. M. (2017, July 10). *Enhanced Deep Residual Networks for Single Image Super-Resolution*. arXiv: 1707.02921 [cs]. Retrieved January 1, 2019, from <http://arxiv.org/abs/1707.02921>. (Cit. on p. 28)
- Lindzey, L. E., Beem, L. H., Young, D. A., Quartini, E., Blankenship, D. D., Lee, C.-K., Lee, W. S., Lee, J. I., & Lee, J. (2020). Aerogeophysical characterization of an active subglacial lake system in the David Glacier catchment, Antarctica. *The Cryosphere*, 14(7), 2217–2233. <https://doi.org/10.5194/tc-14-2217-2020> (cit. on p. 92)
- Liu, X., Wang, Y., & Liu, Q. (2018, May 9). *PSGAN: A Generative Adversarial Network for Remote Sensing Image Pan-Sharpening*. arXiv: 1805.03371 [cs]. Retrieved March 11, 2019, from <http://arxiv.org/abs/1805.03371>. (Cit. on p. 29)
- Lliboutry, L. (1968). General Theory of Subglacial Cavitation and Sliding of Temperate Glaciers. *Journal of Glaciology*, 7(49), 21–58. <https://doi.org/10.3189/S0022143000020396> (cit. on p. 72)
- Lukin, V. V., & Vasiliev, N. I. (2014). Technological aspects of the final phase of drilling borehole 5G and unsealing Vostok Subglacial Lake, East Antarctica. *Annals of Glaciology*, 55(65), 83–89. <https://doi.org/10.3189/2014AoG65A002> (cit. on p. 71)
- Lythe, M. B., & Vaughan, D. G. (2001). BEDMAP: A new ice thickness and subglacial topographic model of Antarctica. *Journal of Geophysical Research: Solid Earth*, 106(B6), 11335–11351. <https://doi.org/10.1029/2000JB900449> (cit. on pp. 26, 49)

- Maas, A. L., Hannun, A. Y., & Ng, A. Y. (2013). Rectifier nonlinearities improve neural network acoustic models. *ICML Workshop on Deep Learning for Audio, Speech, and Language Processing*. https://ai.stanford.edu/~amaas/papers/relu_hybrid_icml2013_final.pdf (cit. on pp. 33, 34)
- MacAyeal, D. R. (1989). Large-scale ice flow over a viscous basal sediment: Theory and application to ice stream B, Antarctica. *Journal of Geophysical Research: Solid Earth*, 94(B4), 4071–4087. <https://doi.org/10.1029/JB094iB04p04071> (cit. on p. 48)
- MacAyeal, D. R. (1992). The basal stress distribution of Ice Stream E, Antarctica, inferred by control methods. *Journal of Geophysical Research: Solid Earth*, 97(B1), 595–603. <https://doi.org/10.1029/91JB02454> (cit. on pp. 48, 55)
- Malczyk, G., Gourmelen, N., Goldberg, D., Wuite, J., & Nagler, T. (2020). Repeat Subglacial Lake Drainage and Filling beneath Thwaites Glacier. *Geophysical Research Letters*. <https://doi.org/10.1029/2020GL089658> (cit. on p. 92)
- Markus, T., Neumann, T., Martino, A., Abdalati, W., Brunt, K., Csatho, B., Farrell, S., Fricker, H., Gardner, A., Harding, D., Jasinski, M., Kwok, R., Magruder, L., Lubin, D., Luthcke, S., Morison, J., Nelson, R., Neuenschwander, A., Palm, S., ... Zwally, J. (2017). The Ice, Cloud, and land Elevation Satellite-2 (ICESat-2): Science requirements, concept, and implementation. *Remote Sensing of Environment*, 190, 260–273. <https://doi.org/10.1016/j.rse.2016.12.029> (cit. on pp. 18, 43, 67, 74, 77, 78)
- Masi, G., Cozzolino, D., Verdoliva, L., & Scarpa, G. (2016). Pansharpening by Convolutional Neural Networks. *Remote Sensing*, 8(7), 594. <https://doi.org/10.3390/rs8070594> (cit. on p. 28)
- McMillan, M., Corr, H., Shepherd, A., Ridout, A., Laxon, S., & Cullen, R. (2013). Three-dimensional mapping by CryoSat-2 of subglacial lake volume changes. *Geophysical Research Letters*, 40(16), 4321–4327. <https://doi.org/10.1002/grl.50689> (cit. on pp. 70, 77)
- Meier, W. N., Gallaher, D., & Campbell, G. G. (2013). New estimates of Arctic and Antarctic sea ice extent during September 1964 from recovered Nimbus I satellite imagery. *The Cryosphere*, 7(2), 699–705. <https://doi.org/10.5194/tc-7-699-2013> (cit. on p. 18)
- Mikucki, J. A., Lee, P. A., Ghosh, D., Purcell, A. M., Mitchell, A. C., Mankoff, K. D., Fisher, A. T., Tulaczyk, S. M., Carter, S., Siegfried, M. R., Fricker, H. A., Hodson, T., Coenen, J., Powell, R., Scherer, R., Vick-Majors, T., Achberger, A. A., Christner, B. C., Tranter, M., & the WISSARD Science Team. (2016). Subglacial Lake Whillans microbial biogeochemistry: A synthesis of current knowledge. *Philosophical Transactions of the Royal Society A: Mathematical, Physical and Engineering Sciences*, 374(2059), 20140290. <https://doi.org/10.1098/rsta.2014.0290> (cit. on p. 71)
- Minchew, B., & Joughin, I. (2020). Toward a universal glacier slip law. *Science*, 368(6486), 29–30. <https://doi.org/10.1126/science.abb3566> (cit. on pp. 20, 22, 48, 50, 51, 64)
- Monnier, J., & Zhu, J. (2018, November). *Inference of the bed topography in poorly flew over ice-sheets areas from surface data and a reduced uncertainty flow model*. Retrieved March 7, 2019, from <https://hal.archives-ouvertes.fr/hal-01926620>. (Cit. on p. 27)

- Morlighem, M. (2019). *MEaSUREs BedMachine Antarctica, Version 1*. NASA National Snow; Ice Data Center DAAC. <https://doi.org/10.5067/C2GFER6PTOS4>. (Cit. on pp. 34, 35, 42)
- Morlighem, M. (2020). *MEaSUREs BedMachine Antarctica, Version 2*. NASA National Snow; Ice Data Center DAAC. <https://doi.org/10.5067/E1QL9HFQ7A8M>. (Cit. on pp. 20, 48, 49, 56, 59, 64)
- Morlighem, M., Rignot, E., Seroussi, H., Larour, E., Ben Dhia, H., & Aubry, D. (2011). A mass conservation approach for mapping glacier ice thickness. *Geophysical Research Letters*, 38(19). <https://doi.org/10.1029/2011GL048659> (cit. on pp. 26, 48)
- Morlighem, M., Rignot, E., Binder, T., Blankenship, D., Drews, R., Eagles, G., Eisen, O., Ferraccioli, F., Forsberg, R., Fretwell, P., Goel, V., Greenbaum, J. S., Gudmundsson, G. H., Guo, J., Helm, V., Hofstede, C., Howat, I., Humbert, A., Jokat, W., ... Young, D. A. (2019). Deep glacial troughs and stabilizing ridges unveiled beneath the margins of the Antarctic ice sheet. *Nature Geoscience*, 13(2), 132–137. <https://doi.org/10.1038/s41561-019-0510-8> (cit. on pp. 21, 25, 26, 40, 42, 44, 48, 49, 99)
- Morlighem, M., Seroussi, H., Larour, E., & Rignot, E. (2013). Inversion of basal friction in Antarctica using exact and incomplete adjoints of a higher-order model. *Journal of Geophysical Research: Earth Surface*, 118(3), 1746–1753. <https://doi.org/10.1002/jgrf.20125> (cit. on pp. 48, 55)
- Morlighem, M., Williams, C. N., Rignot, E., An, L., Arndt, J. E., Bamber, J. L., Catania, G., Chauché, N., Dowdeswell, J. A., Dorschel, B., Fenty, I., Hogan, K., Howat, I., Hubbard, A., Jakobsson, M., Jordan, T. M., Kjeldsen, K. K., Millan, R., Mayer, L., ... Zingleren, K. B. (2017). BedMachine v3: Complete Bed Topography and Ocean Bathymetry Mapping of Greenland From Multibeam Echo Sounding Combined With Mass Conservation. *Geophysical Research Letters*, 44(21), 11, 051–11, 061. <https://doi.org/10.1002/2017GL074954> (cit. on p. 26)
- Mouginot, J., Rignot, E., & Scheuchl, B. (2019a). Continent-Wide, Interferometric SAR Phase, Mapping of Antarctic Ice Velocity. *Geophysical Research Letters*, 46(16), 9710–9718. <https://doi.org/10.1029/2019GL083826> (cit. on pp. 19, 30, 55)
- Mouginot, J., Rignot, E., & Scheuchl, B. (2019b). *MEaSUREs Phase Map of Antarctic Ice Velocity, Version 1*. NASA National Snow; Ice Data Center DAAC. <https://doi.org/10.5067/PZ3NJ5RXRH10>. (Cit. on pp. 31, 32, 41, 43, 44, 54, 59, 68)
- Mouginot, J., Scheuchl, B., & Rignot, E. (2017). *MEaSUREs Antarctic Boundaries for IPY 2007-2009 from Satellite Radar, Version 2*. NASA National Snow; Ice Data Center DAAC. <https://doi.org/10.5067/AXE4121732AD>. (Cit. on p. 34)
- Napoleoni, F., Jamieson, S. S. R., Ross, N., Bentley, M. J., Rivera, A., Smith, A. M., Siegert, M. J., Paxman, G. J. G., Gacitúa, G., Uribe, J. A., Zamora, R., Brisbourne, A. M., & Vaughan, D. G. (2020). Subglacial lakes and hydrology across the Ellsworth Subglacial Highlands, West Antarctica. *The Cryosphere*, 14(12), 4507–4524. <https://doi.org/10.5194/tc-14-4507-2020> (cit. on pp. 70, 92)

- Nasrollahi, K., & Moeslund, T. B. (2014). Super-resolution: A comprehensive survey. *Machine Vision and Applications*, 25(6), 1423–1468. <https://doi.org/10.1007/s00138-014-0623-4> (cit. on p. 27)
- Neumann, T. A., Brenner, A. C., Hancock, D. W., Robbins, J., Luthcke, S. B., Harbeck, K., Lee, J., Gibbons, A., Saba, J., & Brunt, K. M. (2020). *ATLAS/ICESat-2 L2A Global Geolocated Photon Data, version 3*. NASA National Snow; Ice Data Center DAAC. <https://doi.org/10.5067/ATLAS/ATL03.003>. (Cit. on p. 96)
- Neumann, T. A., Martino, A. J., Markus, T., Bae, S., Bock, M. R., Brenner, A. C., Brunt, K. M., Cavanaugh, J., Fernandes, S. T., Hancock, D. W., Harbeck, K., Lee, J., Kurtz, N. T., Luers, P. J., Luthcke, S. B., Magruder, L., Pennington, T. A., Ramos-Izquierdo, L., Rebold, T., ... Thomas, T. C. (2019). The Ice, Cloud, and Land Elevation Satellite – 2 mission: A global geolocated photon product derived from the Advanced Topographic Laser Altimeter System. *Remote Sensing of Environment*, 233, 111325. <https://doi.org/10.1016/j.rse.2019.111325> (cit. on pp. 67, 74)
- Ng, F. S. L. (2000). Coupled ice–till deformation near subglacial channels and cavities. *Journal of Glaciology*, 46(155), 580–598. <https://doi.org/10.3189/172756500781832756> (cit. on p. 72)
- Nias, I. J., Cornford, S. L., & Payne, A. J. (2018). New Mass-Conserving Bedrock Topography for Pine Island Glacier Impacts Simulated Decadal Rates of Mass Loss. *Geophysical Research Letters*, 45(7), 3173–3181. <https://doi.org/10.1002/2017GL076493> (cit. on p. 49)
- Nias, I. J., Cornford, S. L., & Payne, A. J. (2016). Contrasting the modelled sensitivity of the Amundsen Sea Embayment ice streams. *Journal of Glaciology*, 62(233), 552–562. <https://doi.org/10.1017/jog.2016.40> (cit. on p. 26)
- Nye, J. F. (1969–September 13). Water at the bed of a glacier. *Symposium on the Hydrology of Glaciers*, 95, 189–194. http://hydrologie.org/redbooks/a095/iahs_095_0189.pdf (cit. on p. 72)
- Orosei, R., Lauro, S. E., Pettinelli, E., Cicchetti, A., Coradini, M., Cosciotti, B., Di Paolo, F., Flamini, E., Mattei, E., Pajola, M., Soldovieri, F., Cartacci, M., Cassenti, F., Frigeri, A., Giuppi, S., Martufi, R., Masdea, A., Mitri, G., Nenna, C., ... Seu, R. (2018). Radar evidence of subglacial liquid water on Mars. *Science*, eaar7268. <https://doi.org/10.1126/science.aar7268> (cit. on p. 18)
- Oswald, G. K. A., & Robin, G. D. Q. (1973). Lakes Beneath the Antarctic Ice Sheet. *Nature*, 245(5423), 251–254. <https://doi.org/10.1038/245251a0> (cit. on p. 68)
- Park, T., Liu, M.-Y., Wang, T.-C., & Zhu, J.-Y. (2019, March 18). *Semantic Image Synthesis with Spatially-Adaptive Normalization*. arXiv: 1903.07291 [cs]. Retrieved March 19, 2019, from <http://arxiv.org/abs/1903.07291>. (Cit. on p. 29)
- Pritchard, H. D., Arthern, R. J., Vaughan, D. G., & Edwards, L. A. (2009). Extensive dynamic thinning on the margins of the Greenland and Antarctic ice sheets. *Nature*, 461(7266), 971–975. <https://doi.org/10.1038/nature08471> (cit. on p. 76)
- Raymond, M. J., & Gudmundsson, G. H. (2005). On the relationship between surface and basal properties on glaciers, ice sheets, and ice streams. *Journal of Geophysical Research: Solid Earth*, 110(B8), B08411. <https://doi.org/10.1029/2005JB003681> (cit. on pp. 26, 76)

- Reeh, N., Madsen, S. N., & Mohr, J. J. (1999). Combining SAR interferometry and the equation of continuity to estimate the three-dimensional glacier surface-velocity vector. *Journal of Glaciology*, 45(151), 533–538. <https://doi.org/10.1017/S002214300001398> (cit. on p. 74)
- Rignot, E., Mouginot, J., Morlighem, M., Seroussi, H., & Scheuchl, B. (2014). Widespread, rapid grounding line retreat of Pine Island, Thwaites, Smith, and Kohler glaciers, West Antarctica, from 1992 to 2011. *Geophysical Research Letters*, 41(10), 3502–3509. <https://doi.org/10.1002/2014GL060140> (cit. on pp. 48, 49)
- Rignot, E., Mouginot, J., & Scheuchl, B. (2011). Antarctic grounding line mapping from differential satellite radar interferometry. *Geophysical Research Letters*, 38(10). <https://doi.org/10.1029/2011GL047109> (cit. on p. 34)
- Rippin, D., Bingham, R., Jordan, T., Wright, A., Ross, N., Corr, H., Ferraccioli, F., Le Brocq, A., Rose, K., & Siegert, M. (2014). Basal roughness of the Institute and Möller Ice Streams, West Antarctica: Process determination and landscape interpretation. *Geomorphology*, 214, 139–147. <https://doi.org/10.1016/j.geomorph.2014.01.021> (cit. on p. 37)
- Ritz, C., Edwards, T. L., Durand, G., Payne, A. J., Peyaud, V., & Hindmarsh, R. C. A. (2015). Potential sea-level rise from Antarctic ice-sheet instability constrained by observations. *Nature*, 528(7580), 115–118. <https://doi.org/10.1038/nature16147> (cit. on pp. 47, 51)
- Rivera, A., Uribe, J., Zamora, R., & Oberreuter, J. (2015). Subglacial Lake CECs: Discovery and in situ survey of a privileged research site in West Antarctica. *Geophysical Research Letters*, 42(10), 3944–3953. <https://doi.org/10.1002/2015GL063390> (cit. on p. 70)
- Robin, G. D. Q., Evans, S., & Bailey, J. T. (1969). Interpretation of Radio Echo Sounding in Polar Ice Sheets. *Philosophical Transactions of the Royal Society A: Mathematical, Physical and Engineering Sciences*, 265(1166), 437–505. <https://doi.org/10.1098/rsta.1969.0063> (cit. on p. 68)
- Robin, G. D. Q., Swithinbank, C., & Smith, B. (1970). Radio echo exploration of the Antarctic ice sheet. In A. Gow, C. Keeler, C. Langway, & W. Weeks (Eds.), *International Symposium on Antarctic Glaciological Exploration (IS-AGE)* (pp. 97–115). International Association of Scientific Hydrology. <https://iahs.info/uploads/dms/086017.pdf>. (Cit. on p. 26)
- Rooney, S. T., Blankenship, D. D., Alley, R. B., & Bentley, C. R. (1987). Till beneath ice stream B: 2. Structure and continuity. *Journal of Geophysical Research*, 92(B9), 8913. <https://doi.org/10.1029/JB092iB09p08913> (cit. on p. 72)
- Röthlisberger, H. (1972). Water Pressure in Intra- and Subglacial Channels. *Journal of Glaciology*, 11(62), 177–203. <https://doi.org/10.3189/S0022143000022188> (cit. on p. 72)
- Roy, D., Wulder, M., Loveland, T., C.E., W., Allen, R., Anderson, M., Helder, D., Irons, J., Johnson, D., Kennedy, R., Scambos, T., Schaaf, C., Schott, J., Sheng, Y., Vermote, E., Belward, A., Bindschadler, R., Cohen, W., Gao, F., ... Zhu, Z. (2014). Landsat-8: Science and product vision for terrestrial global change research. *Remote Sensing of Environment*, 145, 154–172. <https://doi.org/10.1016/j.rse.2014.02.001> (cit. on p. 18)
- Rumelhart, D. E., Hinton, G. E., & Williams, R. J. (1986). Learning representations by back-propagating errors. *Nature*, 323(6088), 533–536. <https://doi.org/10.1038/323533a0> (cit. on p. 27)

- Scambos, T. A. (2014). Snow Megadune. *Encyclopedia of Planetary Landforms* (pp. 1–3). Springer New York. https://doi.org/10.1007/978-1-4614-9213-9_620-1. (Cit. on p. 40)
- Scambos, T. A., Berthier, E., & Shuman, C. A. (2011). The triggering of subglacial lake drainage during rapid glacier drawdown: Crane Glacier, Antarctic Peninsula. *Annals of Glaciology*, 52(59), 74–82. <https://doi.org/10.3189/172756411799096204> (cit. on pp. 22, 73)
- Scarpa, G., Vitale, S., & Cozzolino, D. (2018). Target-Adaptive CNN-Based Pan-sharpening. *IEEE Transactions on Geoscience and Remote Sensing*, 56(9), 5443–5457. <https://doi.org/10.1109/TGRS.2018.2817393> (cit. on p. 28)
- Schlegel, N.-J., Seroussi, H., Schodlok, M. P., Larour, E. Y., Boening, C., Limonadi, D., Watkins, M. M., Morlighem, M., & van den Broeke, M. R. (2018). Exploration of Antarctic Ice Sheet 100-year contribution to sea level rise and associated model uncertainties using the ISSM framework. *The Cryosphere*, 12(11), 3511–3534. <https://doi.org/10.5194/tc-12-3511-2018> (cit. on p. 48)
- Schoof, C. (2002). Basal perturbations under ice streams: Form drag and surface expression. *Journal of Glaciology*, 48(162), 407–416. <https://doi.org/10.3189/172756502781831269> (cit. on pp. 20, 48, 49)
- Schoof, C. (2005). The effect of cavitation on glacier sliding. *Proceedings of the Royal Society A: Mathematical, Physical and Engineering Sciences*, 461(2055), 609–627. <https://doi.org/10.1098/rspa.2004.1350> (cit. on pp. 50–53)
- Schoof, C. (2007). Ice sheet grounding line dynamics: Steady states, stability, and hysteresis. *Journal of Geophysical Research*, 112(F3). <https://doi.org/10.1029/2006JF000664> (cit. on p. 48)
- Schoof, C., & Hindmarsh, R. C. A. (2010). Thin-Film Flows with Wall Slip: An Asymptotic Analysis of Higher Order Glacier Flow Models. *The Quarterly Journal of Mechanics and Applied Mathematics*, 63(1), 73–114. <https://doi.org/10.1093/qjmam/hbp025> (cit. on pp. 49, 53)
- Schubert, E., Sander, J., Ester, M., Kriegel, H. P., & Xu, X. (2017). DBSCAN Revisited, Revisited: Why and How You Should (Still) Use DBSCAN. *ACM Transactions on Database Systems*, 42(3), 1–21. <https://doi.org/10.1145/3068335> (cit. on p. 79)
- Sergienko, O. V., & Hindmarsh, R. C. A. (2013). Regular Patterns in Frictional Resistance of Ice-Stream Beds Seen by Surface Data Inversion. *Science*, 342(6162), 1086–1089. <https://doi.org/10.1126/science.1243903> (cit. on p. 41)
- Sergienko, O. V., MacAyeal, D. R., & Bindschadler, R. A. (2007). Causes of sudden, short-term changes in ice-stream surface elevation. *Geophysical Research Letters*, 34(22). <https://doi.org/10.1029/2007GL031775> (cit. on pp. 76, 96)
- Seroussi, H., Nowicki, S., Payne, A. J., Goelzer, H., Lipscomb, W. H., Abe-Ouchi, A., Agosta, C., Albrecht, T., Asay-Davis, X., Barthel, A., Calov, R., Cullather, R., Dumas, C., Galton-Fenzi, B. K., Gladstone, R., Golledge, N. R., Gregory, J. M., Greve, R., Hattermann, T., ... Zwinger, T. (2020). ISMIP6 Antarctica: A multi-model ensemble of the Antarctic ice sheet evolution over the 21st century. *The Cryosphere*, 14(9), 3033–3070. <https://doi.org/10.5194/tc-14-3033-2020> (cit. on p. 23)
- Seroussi, H., Nowicki, S., Simon, E., Abe-Ouchi, A., Albrecht, T., Brondex, J., Cornford, S., Dumas, C., Gillet-Chaulet, F., Goelzer, H., Golledge, N. R., Gregory, J. M., Greve, R., Hoffman, M. J., Humbert, A., Huybrechts, P., Kleiner, T., Larour, E., Leguy, G., ... Zhang, T. (2019). initMIP-Antarctica: An ice sheet

- model initialization experiment of ISMIP6. *The Cryosphere*, 13(5), 1441–1471. <https://doi.org/10.5194/tc-13-1441-2019> (cit. on pp. 48, 50)
- Shepherd, A., Ivins, E. R., A, G., Barletta, V. R., Bentley, M. J., Bettadpur, S., Briggs, K. H., Bromwich, D. H., Forsberg, R., Galin, N., Horwath, M., Jacobs, S., Joughin, I., King, M. A., Lenaerts, J. T. M., Li, J., Ligtenberg, S. R. M., Luckman, A., Luthcke, S. B., ... Zwally, H. J. (2012). A Reconciled Estimate of Ice-Sheet Mass Balance. *Science*, 338(6111), 1183–1189. <https://doi.org/10.1126/science.1228102> (cit. on p. 70)
- Shi, L., Allen, C. T., Ledford, J. R., Rodriguez-Morales, F., Blake, W. A., Panzer, B. G., Prokopiack, S. C., Leuschen, C. J., & Gogineni, S. (2010–July 30). Multichannel Coherent Radar Depth Sounder for NASA Operation Ice Bridge. *2010 IEEE International Geoscience and Remote Sensing Symposium*, 1729–1732. <https://doi.org/10.1109/IGARSS.2010.5649518> (cit. on pp. 21, 29, 37)
- Shoemaker, E. M. (1986). Subglacial Hydrology for an Ice Sheet Resting on a Deformable Aquifer. *Journal of Glaciology*, 32(110), 20–30. <https://doi.org/10.3189/S0022143000006833> (cit. on p. 72)
- Shreve, R. L. (1972). Movement of Water in Glaciers. *Journal of Glaciology*, 11(62), 205–214. <https://doi.org/10.3189/S00221430002219X> (cit. on p. 109)
- Shuman, C. A., Zwally, H. J., Schutz, B. E., Brenner, A. C., DiMarzio, J. P., Suchdeo, V. P., & Fricker, H. A. (2006). ICESat Antarctic elevation data: Preliminary precision and accuracy assessment. *Geophysical Research Letters*, 33(7). <https://doi.org/10.1029/2005GL025227> (cit. on p. 67)
- Siegert, M. J., Ross, N., Corr, H., Smith, B., Jordan, T., Bingham, R. G., Ferraccioli, F., Rippin, D. M., & Le Brocq, A. (2014). Boundary conditions of an active West Antarctic subglacial lake: Implications for storage of water beneath the ice sheet. *The Cryosphere*, 8(1), 15–24. <https://doi.org/10.5194/tc-8-15-2014> (cit. on p. 70)
- Siegert, M. J., Carter, S. P., Tabacco, I., Popov, S., & Blankenship, D. D. (2005). A revised inventory of Antarctic subglacial lakes. *Antarctic Science*, 17(03), 453. <https://doi.org/10.1017/S0954102005002889> (cit. on p. 69)
- Siegert, M. J., Dowdeswell, J., Gorman, M., & McIntyre, N. (1996). An inventory of Antarctic sub-glacial lakes. *Antarctic Science*, 8(03). <https://doi.org/10.1017/S0954102096000405> (cit. on p. 69)
- Siegert, M. J., Makinson, K., Blake, D., Mowlem, M., & Ross, N. (2014). An assessment of deep hot-water drilling as a means to undertake direct measurement and sampling of Antarctic subglacial lakes: Experience and lessons learned from the Lake Ellsworth field season 2012/13. *Annals of Glaciology*, 55(65), 59–73. <https://doi.org/10.3189/2014AoG65A008> (cit. on p. 48)
- Siegert, M. J., Ross, N., & Le Brocq, A. M. (2016). Recent advances in understanding Antarctic subglacial lakes and hydrology. *Philosophical Transactions of the Royal Society A: Mathematical, Physical and Engineering Sciences*, 374(2059), 20140306. <https://doi.org/10.1098/rsta.2014.0306> (cit. on p. 70)
- Siegert, M. J., Taylor, J., Payne, A. J., & Hubbard, B. (2004). Macro-scale bed roughness of the siple coast ice streams in West Antarctica. *Earth Surface Processes and Landforms*, 29(13), 1591–1596. <https://doi.org/10.1002/esp.1100> (cit. on pp. 20, 26)
- Siegfried, M. R., & Fricker, H. A. (2018). Thirteen years of subglacial lake activity in Antarctica from multi-mission satellite altimetry. *Annals of Glaciology*,

- 1–14. <https://doi.org/10.1017/aog.2017.36> (cit. on pp. 19, 22, 23, 68, 69, 76, 78, 80, 82, 83, 92, 96, 100, 101)
- Siegfried, M. R., Fricker, H. A., Carter, S. P., & Tulaczyk, S. M. (2016). Episodic ice velocity fluctuations triggered by a subglacial flood in West Antarctica. *Geophysical Research Letters*, 43(6), 2640–2648. <https://doi.org/10.1002/2016GL067758> (cit. on pp. 19, 73, 76, 81, 92, 94, 96, 100)
- Siegfried, M. R., & Fricker, H. A. (2021). Illuminating active subglacial lake processes with ICESat-2 laser altimetry. *Geophysical Research Letters*. <https://doi.org/10.1029/2020GL091089> (cit. on pp. 93, 96)
- Simonyan, K., & Zisserman, A. (2014, September 4). *Very Deep Convolutional Networks for Large-Scale Image Recognition*. arXiv: 1409.1556 [cs]. Retrieved January 26, 2018, from <http://arxiv.org/abs/1409.1556>. (Cit. on p. 34)
- Smith, A., Murray, T., Nicholls, K., Makinson, K., Aðalgeirsdóttir, G., Behar, A., & Vaughan, D. (2007). Rapid erosion, drumlin formation, and changing hydrology beneath an Antarctic ice stream. *Geology*, 35(2), 127. <https://doi.org/10.1130/G23036A.1> (cit. on p. 72)
- Smith, B. E., Bentley, C. R., & Raymond, C. F. (2005). Recent elevation changes on the ice streams and ridges of the Ross Embayment from ICESat crossovers. *Geophysical Research Letters*, 32(21). <https://doi.org/10.1029/2005GL024365> (cit. on p. 76)
- Smith, B. E., Dickinson, S., Jelley, B. P., Neumann, T. A., Hancock, D. W., Lee, J., & Harbeck, K. (2021). *ATLAS/ICESat-2 L3B Annual Land Ice Height, version 2*. NASA National Snow; Ice Data Center DAAC. <https://doi.org/10.5067/ATLAS/ATL11.002>. (Cit. on pp. 74, 78, 96)
- Smith, B. E., Fricker, H. A., Gardner, A. S., Medley, B., Nilsson, J., Paolo, F. S., Holschuh, N., Adusumilli, S., Brunt, K., Csatho, B., Harbeck, K., Markus, T., Neumann, T., Siegfried, M. R., & Zwally, H. J. (2020). Pervasive ice sheet mass loss reflects competing ocean and atmosphere processes. *Science*, eaaz5845. <https://doi.org/10.1126/science.aaz5845> (cit. on p. 75)
- Smith, B. E., Fricker, H. A., Gardner, A. S., Siegfried, M. R., Adusumilli, S., Csathó, B. M., Holschuh, N., Nilsson, J., Paolo, F. S., & ICESat-2 Science Team. (2020). *ATLAS/ICESat-2 L3A Land Ice Height, version 3*. NASA National Snow; Ice Data Center DAAC. <https://doi.org/10.5067/ATLAS/ATL06.003>. (Cit. on p. 96)
- Smith, B. E., Fricker, H. A., Holschuh, N., Gardner, A. S., Adusumilli, S., Brunt, K. M., Csatho, B., Harbeck, K., Huth, A., Neumann, T., Nilsson, J., & Siegfried, M. R. (2019). Land ice height-retrieval algorithm for NASA's ICESat-2 photon-counting laser altimeter. *Remote Sensing of Environment*, 233, 111352. <https://doi.org/10.1016/j.rse.2019.111352> (cit. on pp. 77, 78)
- Smith, B. E., Fricker, H. A., Joughin, I. R., & Tulaczyk, S. M. (2009). An inventory of active subglacial lakes in Antarctica detected by ICESat (2003–2008). *Journal of Glaciology*, 55(192), 573–595. <https://doi.org/10.3189/002214309789470879> (cit. on pp. 19, 22, 69, 70, 76, 78, 80, 83, 92)
- Smith, B. E., Gourmelen, N., Huth, A., & Joughin, I. (2017). Connected subglacial lake drainage beneath Thwaites Glacier, West Antarctica. *The Cryosphere*, 11(1), 451–467. <https://doi.org/10.5194/tc-11-451-2017> (cit. on pp. 64, 70, 73, 92, 94)
- Smith-Johnsen, S., de Fleurian, B., & Nisancioglu, K. H. (2020). The role of subglacial hydrology in ice streams with elevated geothermal heat flux. *Journal*

- of Glaciology*, 66(256), 303–312. <https://doi.org/10.1017/jog.2020.8> (cit. on p. 23)
- Solheim, A., & Pfirman, S. L. (1985). Sea-floor morphology outside a grounded, surging glacier; Bråsvellbreen, Svalbard. *Marine Geology*, 65(1-2), 127–143. [https://doi.org/10.1016/0025-3227\(85\)90050-7](https://doi.org/10.1016/0025-3227(85)90050-7) (cit. on p. 40)
- Sommers, A., Rajaram, H., & Morlighem, M. (2018). SHAKTI: Subglacial Hydrology and Kinetic, Transient Interactions v1.0. *Geoscientific Model Development*, 11(7), 2955–2974. <https://doi.org/10.5194/gmd-11-2955-2018> (cit. on pp. 23, 65, 101)
- Stearns, L. A., & van der Veen, C. J. (2018). Friction at the bed does not control fast glacier flow. *Science*, 361(6399), 273–277. <https://doi.org/10.1126/science.aat2217> (cit. on p. 50)
- Stearns, L. A., Smith, B. E., & Hamilton, G. S. (2008). Increased flow speed on a large East Antarctic outlet glacier caused by subglacial floods. *Nature Geoscience*, 1(12), 827–831. <https://doi.org/10.1038/ngeo356> (cit. on pp. 22, 73)
- Stokes, C. R., Sanderson, J. E., Miles, B. W. J., Jamieson, S. S. R., & Leeson, A. A. (2019). Widespread distribution of supraglacial lakes around the margin of the East Antarctic Ice Sheet. *Scientific Reports*, 9(1). <https://doi.org/10.1038/s41598-019-50343-5> (cit. on pp. 22, 71)
- Sun, S., Cornford, S. L., Liu, Y., & Moore, J. C. (2014). Dynamic response of Antarctic ice shelves to bedrock uncertainty. *The Cryosphere*, 8(4), 1561–1576. <https://doi.org/10.5194/tc-8-1561-2014> (cit. on p. 49)
- Sun, S., Pattyn, F., Simon, E. G., Albrecht, T., Cornford, S., Calov, R., Dumas, C., Gillet-Chaulet, F., Goelzer, H., Golledge, N. R., Greve, R., Hoffman, M. J., Humbert, A., Kazmierczak, E., Kleiner, T., Leguy, G. R., Lipscomb, W. H., Martin, D., Morlighem, M., . . . Zhang, T. (2020). Antarctic ice sheet response to sudden and sustained ice-shelf collapse (ABUMIP). *Journal of Glaciology*, 1–14. <https://doi.org/10.1017/jog.2020.67> (cit. on p. 50)
- Talalay, P., Li, Y., Augustin, L., Clow, G. D., Hong, J., Lefebvre, E., Markov, A., Motoyama, H., & Ritz, C. (2020). Geothermal heat flux from measured temperature profiles in deep ice boreholes in Antarctica. *The Cryosphere*, 14(11), 4021–4037. <https://doi.org/10.5194/tc-14-4021-2020> (cit. on p. 71)
- Tokui, S., Yamazaki Vincent, H., Okuta, R., Akiba, T., Niitani, Y., Ogawa, T., Saito, S., Suzuki, S., Uenishi, K., & Vogel, B. (2019–August 8). Chainer: A Deep Learning Framework for Accelerating the Research Cycle. *Proceedings of the 25th ACM SIGKDD International Conference on Knowledge Discovery & Data Mining - KDD '19*, 2002–2011. <https://doi.org/10.1145/3292500.3330756> (cit. on p. 107)
- Tozer, B., Sandwell, D. T., Smith, W. H. F., Olson, C., Beale, J. R., & Wessel, P. (2019). Global Bathymetry and Topography at 15 Arc Sec: SRTM15+. *Earth and Space Science*. <https://doi.org/10.1029/2019EA000658> (cit. on p. 68)
- Tsai, R., & Huang, T. S. (1984). Multiframe image restoration and registration. In T. S. Huang (Ed.), *Advances in Computer Vision and Image Processing* (pp. 317–339). JAI Press. <https://ci.nii.ac.jp/naid/10026807118/en/>. (Cit. on p. 27)
- Tsai, V. C., Stewart, A. L., & Thompson, A. F. (2015). Marine ice-sheet profiles and stability under Coulomb basal conditions. *Journal of Glaciology*, 61(226), 205–215. <https://doi.org/10.3189/2015JoG14J221> (cit. on pp. 50, 51, 53)

- Tulaczyk, S. M., & Foley, N. T. (2020). The role of electrical conductivity in radar wave reflection from glacier beds. *The Cryosphere*, 14(12), 4495–4506. <https://doi.org/10.5194/tc-14-4495-2020> (cit. on p. 70)
- Tulaczyk, S. M., Mikucki, J. A., Siegfried, M. R., Priscu, J. C., Barchek, C. G., Beem, L. H., Behar, A., Burnett, J., Christner, B. C., Fisher, A. T., Fricker, H. A., Mankoff, K. D., Powell, R. D., Rack, F., Sampson, D., Scherer, R. P., Schwartz, S. Y., & The Wissard Science Team. (2014). WISSARD at Sub-glacial Lake Whillans, West Antarctica: Scientific operations and initial observations. *Annals of Glaciology*, 55(65), 51–58. <https://doi.org/10.3189/2014AoG65A009> (cit. on pp. 19, 48, 71, 94)
- Uieda, L., Tian, D., Leong, W. J., Toney, L., Newton, T., & Wessel, P. (2020, September 12). *PyGMT: A Python interface for the Generic Mapping Tools* (Version v0.2.1). <https://doi.org/10.5281/ZENODO.4025418>. (Cit. on p. 68)
- van Pelt, W. J. J., Oerlemans, J., Reijmer, C. H., Pettersson, R., Pohjola, V. A., Isaksson, E., & Divine, D. (2013). An iterative inverse method to estimate basal topography and initialize ice flow models. *The Cryosphere*, 7(3), 987–1006. <https://doi.org/10.5194/tc-7-987-2013> (cit. on p. 26)
- Vick-Majors, T. J., Michaud, A. B., Skidmore, M. L., Turetta, C., Barbante, C., Christner, B. C., Dore, J. E., Christianson, K., Mitchell, A. C., Achberger, A. M., Mikucki, J. A., & Priscu, J. C. (2020). Biogeochemical Connectivity Between Freshwater Ecosystems beneath the West Antarctic Ice Sheet and the Sub-Ice Marine Environment. *Global Biogeochemical Cycles*, 34(3). <https://doi.org/10.1029/2019GB006446> (cit. on p. 96)
- Wang, X., Yu, K., Wu, S., Gu, J., Liu, Y., Dong, C., Qiao, Y., & Loy, C. C. (2019). ESRGAN: Enhanced Super-Resolution Generative Adversarial Networks. In L. Leal-Taixé & S. Roth (Eds.), *Computer Vision – ECCV 2018 Workshops* (pp. 63–79). Springer International Publishing. https://doi.org/10.1007/978-3-030-11021-5_5. (Cit. on pp. 28, 32, 34, 43, 99, 103)
- Wang, Z., Bovik, A., Sheikh, H., & Simoncelli, E. (2004). Image Quality Assessment: From Error Visibility to Structural Similarity. *IEEE Transactions on Image Processing*, 13(4), 600–612. <https://doi.org/10.1109/TIP.2003.819861> (cit. on p. 104)
- Weertman, J. (1957). On the Sliding of Glaciers. *Journal of Glaciology*, 3(21), 33–38. <https://doi.org/10.3189/S0022143000024709> (cit. on pp. 20, 48–51, 72)
- Wessel, P., Luis, J., Uieda, L., Scharroo, R., Wobbe, F., Smith, W., & Tian, D. (2019). The Generic Mapping Tools Version 6. *Geochemistry, Geophysics, Geosystems*, 20(11), 5556–5564. <https://doi.org/10.1029/2019GC008515> (cit. on pp. 29, 68, 107)
- Wessel, P. (2010). Tools for analyzing intersecting tracks: The x2sys package. *Computers & Geosciences*, 36(3), 348–354. <https://doi.org/10.1016/j.cageo.2009.05.009> (cit. on p. 80)
- Whillans, I. M. (1977). The Equation of Continuity and its Application to the Ice Sheet Near "Byrd" Station, Antarctica. *Journal of Glaciology*, 18(80), 359–371. <https://doi.org/10.3189/S0022143000021055> (cit. on p. 74)
- Wingham, D., Francis, C., Baker, S., Bouzinac, C., Brockley, D., Cullen, R., de Chateau-Thierry, P., Laxon, S., Mallow, U., Mavrocordatos, C., Phalippou, L., Ratier, G., Rey, L., Rostan, F., Viau, P., & Wallis, D. (2006). CryoSat: A mission to determine the fluctuations in Earth's land and marine ice fields.

- Advances in Space Research*, 37(4), 841–871. <https://doi.org/10.1016/j.asr.2005.07.027> (cit. on pp. 18, 77)
- Winsborrow, M. C., Clark, C. D., & Stokes, C. R. (2010). What controls the location of ice streams? *Earth-Science Reviews*, 103(1-2), 45–59. <https://doi.org/10.1016/j.earscirev.2010.07.003> (cit. on p. 73)
- Wright, A. P., & Siegert, M. J. (2012). A fourth inventory of Antarctic subglacial lakes. *Antarctic Science*, 24(06), 659–664. <https://doi.org/10.1017/S095410201200048X> (cit. on pp. 22, 69)
- Wright, A. P., Young, D. A., Roberts, J. L., Schroeder, D. M., Bamber, J. L., Dowdeswell, J. A., Young, N. W., Le Brocq, A. M., Warner, R. C., Payne, A. J., Blankenship, D. D., van Ommen, T. D., & Siegert, M. J. (2012). Evidence of a hydrological connection between the ice divide and ice sheet margin in the Aurora Subglacial Basin, East Antarctica. *Journal of Geophysical Research: Earth Surface*, 117(F1), n/a–n/a. <https://doi.org/10.1029/2011JF002066> (cit. on p. 70)
- Wright, A. P., Young, D., Bamber, J., Dowdeswell, J., Payne, A., Blankenship, D., & Siegert, M. (2014). Subglacial hydrological connectivity within the Byrd Glacier catchment, East Antarctica. *Journal of Glaciology*, 60(220), 345–352. <https://doi.org/10.3189/2014JoG13J014> (cit. on pp. 22, 70, 73, 92)
- Xu, Z., Wang, X., Chen, Z., Xiong, D., Ding, M., & Hou, W. (2015). Nonlocal similarity based DEM super resolution. *ISPRS Journal of Photogrammetry and Remote Sensing*, 110, 48–54. <https://doi.org/10.1016/j.isprsjprs.2015.10.009> (cit. on p. 29)
- Yang, J., Fu, X., Hu, Y., Huang, Y., Ding, X., & Paisley, J. (2017–October 29). PanNet: A Deep Network Architecture for Pan-Sharpening. *2017 IEEE International Conference on Computer Vision (ICCV)*, 1753–1761. <https://doi.org/10.1109/ICCV.2017.193> (cit. on p. 28)
- Yang, W., Zhang, X., Tian, Y., Wang, W., Xue, J.-H., & Liao, Q. (2019). Deep Learning for Single Image Super-Resolution: A Brief Review. *IEEE Transactions on Multimedia*, 21(12), 3106–3121. <https://doi.org/10.1109/TMM.2019.2919431> (cit. on pp. 27, 43)
- Zhang, T., Price, S., Ju, L., Leng, W., Brondex, J., Durand, G., & Gagliardini, O. (2017). A comparison of two Stokes ice sheet models applied to the Marine Ice Sheet Model Intercomparison Project for plan view models (MISMIP3d). *The Cryosphere*, 11(1), 179–190. <https://doi.org/10.5194/tc-11-179-2017> (cit. on p. 50)
- Zhao, C., Gladstone, R. M., Warner, R. C., King, M. A., Zwinger, T., & Morlighem, M. (2018). Basal friction of Fleming Glacier, Antarctica – Part 2: Evolution from 2008 to 2015. *The Cryosphere*, 12(8), 2653–2666. <https://doi.org/10.5194/tc-12-2653-2018> (cit. on p. 71)
- Zoet, L. K., & Iverson, N. R. (2020). A slip law for glaciers on deformable beds. *Science*, 368(6486), 76–78. <https://doi.org/10.1126/science.aaz1183> (cit. on pp. 48, 50, 51, 64)
- Zwally, H. J. (2002). Surface Melt-Induced Acceleration of Greenland Ice-Sheet Flow. *Science*, 297(5579), 218–222. <https://doi.org/10.1126/science.1072708> (cit. on pp. 22, 73)
- Zwally, H. J., Schutz, B., Abdalati, W., Abshire, J., Bentley, C., Brenner, A., Bufton, J., Dezio, J., Hancock, D., Harding, D., Herring, T., Minster, B., Quinn, K., Palm, S., Spinhirne, J., & Thomas, R. (2002). ICESat's laser measurements

of polar ice, atmosphere, ocean, and land. *Journal of Geodynamics*, 34(3-4), 405–445. [https://doi.org/10.1016/S0264-3707\(02\)00042-X](https://doi.org/10.1016/S0264-3707(02)00042-X) (cit. on p. 67)